An Image Based Vibration Sensor for Soft Tissue Modal Analysis in a Digital Image Elasto Tomography (DIET) System

Sheng Feng

A thesis submitted in partial fulfillment
of the requirements for the degree of
Master of Engineering

in
BioEngineering
at the
University of Canterbury,
Christchurch, New Zealand

September 2011

Abstract

Digital Image Elasto Tomography (DIET) is a non-invasive elastographic breast cancer screening technology, relying on image-based measurement of surface vibrations induced on a breast by mechanical actuation. Knowledge of frequency response characteristics of a breast prior to imaging is critical to maximize the imaging signal and diagnostic capability of the system. A non-invasive image based modal analysis system that is designed to be able to robustly and rapidly identify resonant frequencies in soft tissue is presented in this thesis.

A feasibility analysis reveals that three images per oscillation cycle are sufficient to capture the relative motion behavior at a given frequency. Moreover, the analysis suggests that 2D motion analysis is able to give an accurate estimation of the response at a particular frequency. Thus, a sweep over critical frequency ranges can be performed prior to imaging to determine critical imaging settings of the DIET system to maximize diagnositc performance.

Based on feasibility simulations, a modal analysis system is presented that is based on the existing DIET digital imaging system. A frequency spectrum plot that comprises responses gathered from more than 30 different frequencies can be obtained in about 6 minutes.

Preliminary results obtained from both phantom and human trials indicate that distinctive resonant frequencies can be obtained with the modal analysis system. Due to inhomogeneous properties of human breast tissues, different imaging location appear to pick up different resonances. However, there has been very limited clinical data for validating such behavior.

Overall, a modal analysis system for soft tissue has been developed in this thesis. The system was first evaluated in simulation, then implemented in hardware and software, and finally successfully validated in silicone phantoms as well as human breasts.

Acknowledgements

First and foremost, I wish to thank my supervisors Professor Geoff Chase and Dr Thomas Lotz for their guidance and support throughout this research. I sincerely appreciate the time and effort they have spent on supervising my studies. I am also indebted to Larry Podmore from Boundary LifeSciences, who introduced me to this great project.

I would also like to thank everyone who have helped me along the way - especially Rodney Elliot, Stefanie Gutschmidt, Tim David, Chris Hann, Phil Bones and fellow students from the DIET team. The completion of this work would not have been possible without your support. Thanks to all my friends in Christchurch for keeping me in line and sharing the good and bad times.

I would like to acknowledge the Foundation for Research Science and Technology (FRST) for funding this research.

Finally, much gratitude to my family, especially my parents, for encouraging and supporting me in my every endeavor.

Contents

List of Figures

List of Tables

Abbreviations

DIET	**D**igital **I**mage **E**lasto **T**omography
FE	**F**inite **E**lement
DOF	**D**egree **O**f **F**reedom
LVDT	**L**inear **V**ariable **D**ifferential **T**ransformer
MRE	**M**agnetic **R**esonance **E**lastography
MRI	**M**agnetic **R**esonance **I**maging
DCIS	**D**uctal **C**arcinoma **I**n **S**itu
LDV	**L**aser **D**oppler **V**ibrometer
FOV	**F**ibre **O**ptic **V**ibrometer
NCC	**N**ormalized **C**ross **C**orrelation
SDK	**S**oftware **D**evelopment **K**it
LCM	**L**east **C**ommon **M**ultiple
SIFT	**S**cale **I**nvariant **F**eature **T**ransform
SURF	**S**peeded **U**p **R**obust **F**eatures
ROI	**R**egion **O**f **I**nterest
RMS	**R**oot **M**ean **S**quare
RIO	**R**econfigurable **I**nput **O**utput
DSLR	**D**igital **S**ingle **L**ens **R**eflex

Chapter 1

Introduction and Background

1.1 Breast Cancer

Breast Cancer is the most common type of cancer found in women both in developed and developing countries, accounting for as much as 16% of worldwide female cancer registrations [1]. Successful early detection of breast cancer using screening modalities such as mammography can significantly reduce the mortality rate, by as much as 30% [2].

In New Zealand, breast cancer is the most common type of cancer registered for women aged between 25 to 74, accounting for more than 27% of all new female registrations [2]. Over the past decade, the government has increased the availability of its free screening programs to cover those aged between 45 and 69, and this is believed to be the main cause behind the uptrend in detection rate and downtrend in mortality rate seen in Figure 1.1. However, breast cancer remains to be the second most common cause of cancer death for the female population, accounting for more than 16% of female cancer deaths [3, 4].

Although the risk of developing breast cancer increases with age, incidence among younger women is rising. The exact causes of breast cancer remain unknown. Researches have identified a number of risk factors for breast cancer, including high-fat diet [5], high level of alcohol intake [6–9], obesity [10], radiation, genetic markers [11] and endocrine disruptors [12, 13].

Surgery is usually the first line of attack against breast cancer when the tumor is localized. However, many other adjunct treatments also exist, including chemotherapy,

radiation therapy, hormonal therapy, and targeted therapy. Together with early detection through breast cancer screening programs, these treatments have shown to be effective in reducing the mortality rate.

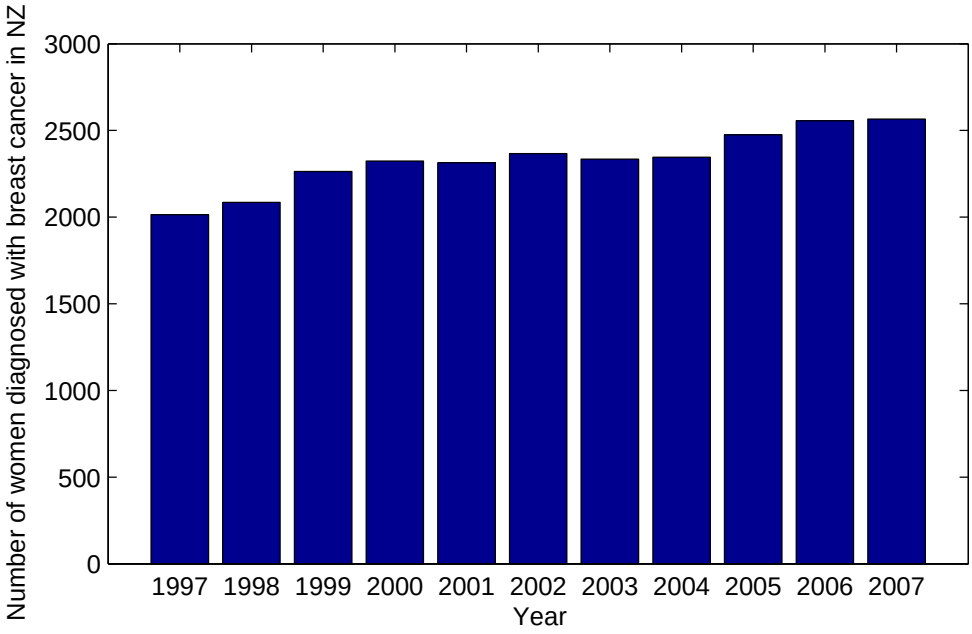

(a) Breast cancer registration in NZ

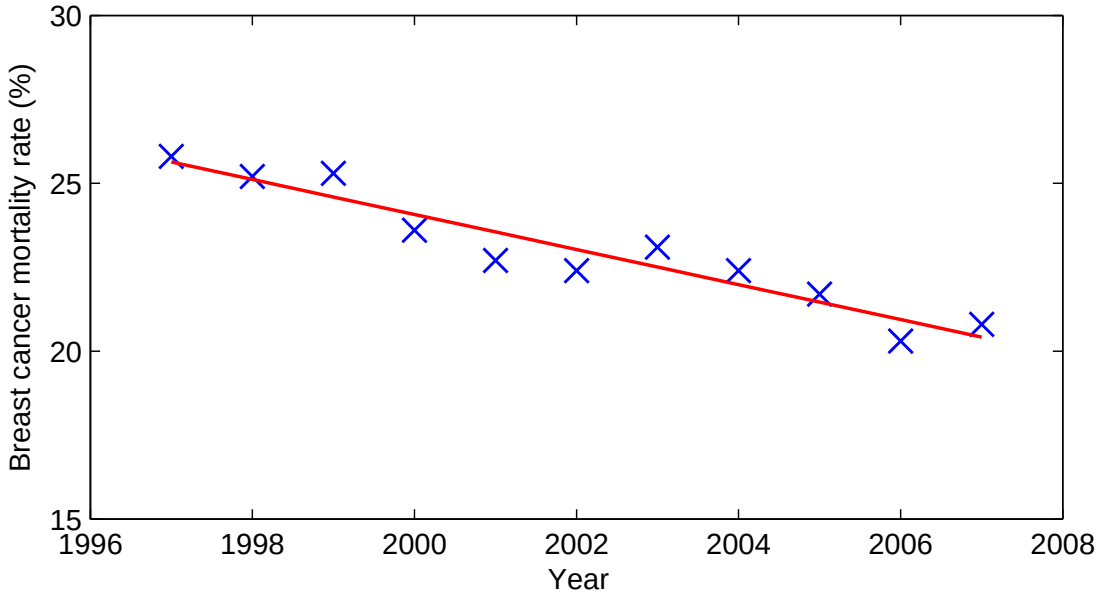

(b) Mortality rate due to breast cancer

FIGURE 1.1: Female breast cancer registration and mortality rates in New Zealand, between the 1997 and 2007 [3].

Mammography is currently one of the most commonly used modalities for reliable detection of early, non-palpable breast cancer. Despite its safety and efficacy, mammography suffers from several major drawbacks. It is known to have a poor sensitivity that can sometimes lead to false positives [14, 15]. Furthermore, the screening process

requires heavy mechanical stress imposed on the breasts, causing pain and discomfort [16]. Moreover, ionizing radiation (X-rays) is used during mammography screenings and many believe the screening process itself may increase the likelihood of developing cancer [17].

The issue of X-ray radiation induced cancer has been a controversial and a much disputed subject within the medical field. Although radiation-induced breast cancers are indistinguishable from other breast cancers, the adverse consequences of ionizing radiation are well established and there has always been doubts on their use in a screening program that aims to detect cancer at an early stage [18]. The rate of cancer detection and that induced by breast screening has been the subject of a series of publications by Law and Faulkner [17, 19, 20].

The past decades have seen increasingly rapid advances in the field of medical imaging. There has been an increasing interest in developing alternative breast imaging techniques. Detecting tumors in soft tissues using elastography, is a promising approach being researched in the medical imaging community [21, 22]. Preliminary results on magnetic resonance elastography (MRE) [23, 24] and ultrasound elastography [25–28] have all shown promising results. All elastographic imaging modalities are aiming to provide a more accurate diagnosis of cancerous tissues. Due to the costly nature of MRE and ultrasonic elastography, these modalities are not very well suited for screening applications.

1.2 DIET System

Digital Image Elasto Tomography (DIET) is an emerging non-invasive and cost-effective elastographic imaging system designed for breast cancer screening. The DIET system is intended to be compact and can be easily deployed, even in remote areas, where people have very little accesses to the breast cancer screening facilities. As shown in Figure 1.2, its design is relatively simple, comprising five consumer digital cameras and a mechanical actuator. Based on external tissue compression and subsequent strain profile analysis, DIET is able to compute elastic modulus profile of the full breast volume. Such elastic properties can then be used to evaluate and detect areas of higher stiffness, potentially cancer, within the breast volume.

During a DIET screening session, the breast undergoes actuations from a sinusoidal vibrating source and its surface is imaged. A typical DIET screening process using the current prototype is depicted in Figure 1.3 and described in more detail here.

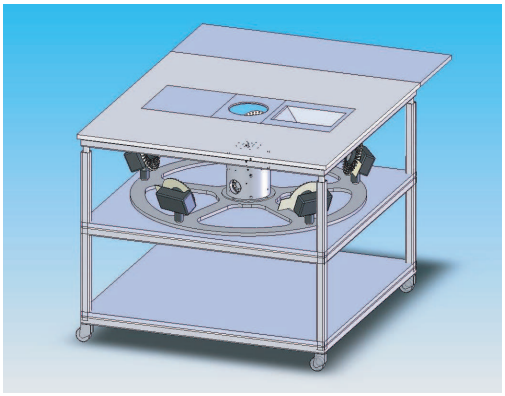

(a) Design drawing

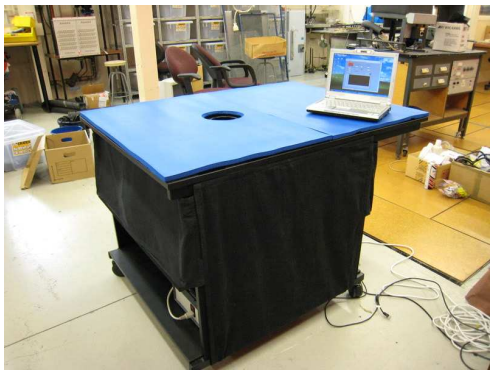

(b) DIET Prototype

(c) Rendered design artwork

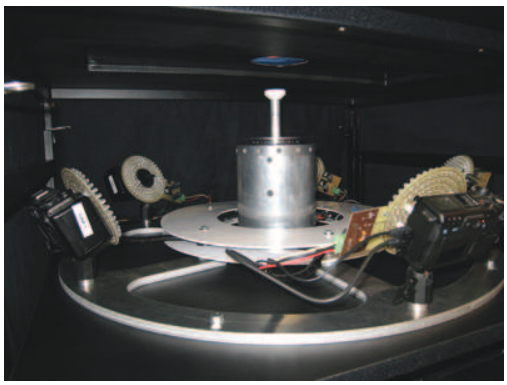

(d) Inside of the current prototype

FIGURE 1.2: DIET prototype.

1) A voice-coil actuator is used to induce sinusoidal oscillation on the breast volume. Typically, the actuation has a frequency of $10-100Hz$ and an amplitude of $0.5-1mm$. Once the breast is moving in its steady state motion, imaging may begin.

2) An array of 5 digital cameras are used to capture the steady state motion of the breast surface. Once the breast is moving in steady state, all points on the breast surface are at the same locations in space at the same point relative to the actuation period. By synchronizing the LED strobe light system to illuminate only at the desired point in time, a single image can be exposed to capture the same state from multiple cycles [29]. This averaging approach effectively enhances the image quality by averaging out noise. Ten images with linear spacing in time between adjacent images are taken to capture a single oscillation cycle. Figure 1.4 illustrates the points in time that are captured by a three image per oscillation setting.

3) Fiducial markers found on the surface are tracked through a single oscillation period on all cameras [30, 31]. By parameterizing the motion, a full description of the frequency response of the breast surface can be obtained and processed.

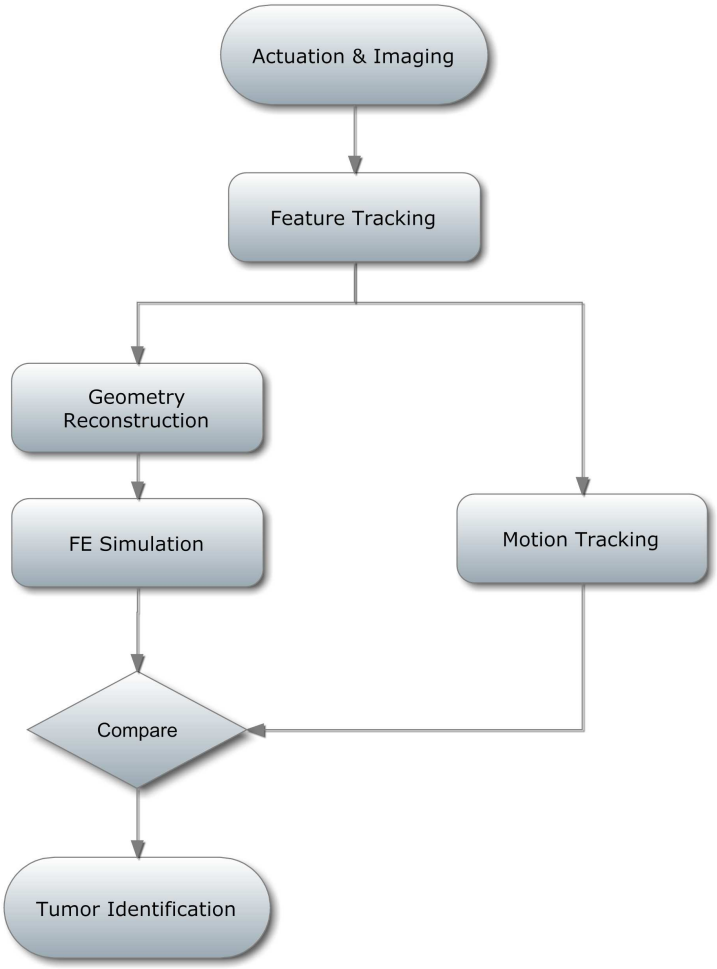

FIGURE 1.3: DIET work-flow describing the imaging procedure.

4) A diagnostic result can be obtained by comparing experimental motion with simulated results. Geometry of the breast volume is reconstructed using 2 steps. First interpolating surface data points using software package FASTRBF, followed by filling a volume into these points using software package GMSH [32]. This geometric property is then used by Finite Element (FE) packages to simulate surface disturbances when inclusions are present. Such as shown in Figure 1.5, surface motion data is then compared with simulation results and can lead to an estimation of the location and size of any stiffer masses [32].

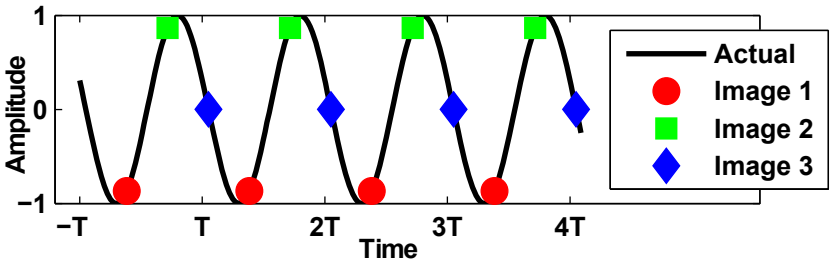

FIGURE 1.4: An example to illustrate 3 images per oscillation cycle, where T corresponds to a single oscillation period. Instead of high speed imaging, sharp images are achieved by long exposure taken over multiple oscillation cycles with illumination from the LED strobe light system. The LED strobe light system is synchronized with the actuation frequency and will only illuminate part of the oscillation cycle allowing for sharp images to be taken.

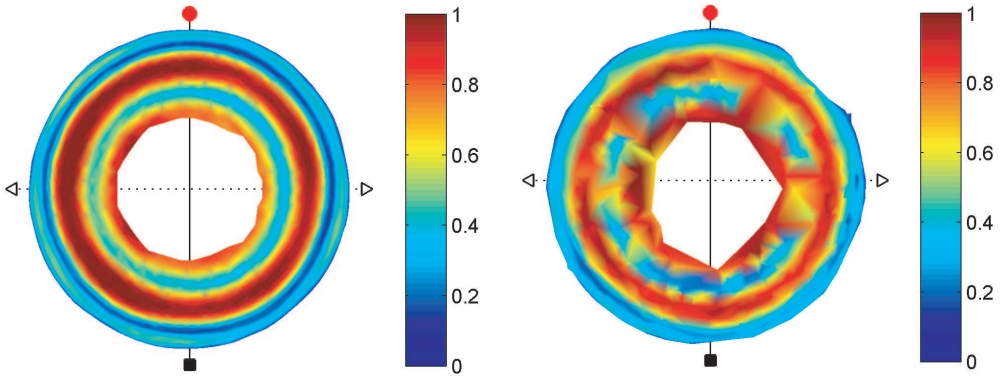

FIGURE 1.5: Tumor diagnosis by comparing Finite Element (FE) simulation results with surface motion data. Motion data (right) demonstrates a reasonably good match with Finite Element (FE) simulation results (left), therefore the two should have similar health status.

A system diagram of the control software of the current prototype is shown in Figure 1.6. Imaging devices are solely controlled by the PC and all other hardware is controlled by a National Instruments^{TM} Reconfigurable Input Output (RIO) system. The RIO system provides real-time control capabilities to ensure accurate actuator operation and strobe synchronization.

1.3 Motivation

In DIET, the actuation frequency is an important experimental parameter that can be altered in a clinical or experimental setting. Due to the damped and viscoelastic behavior of breast tissue, the actuation frequency can strongly influence the motion seen on the breast surface. As shown in Figure 1.7, a slight change in actuation frequency can have severe impacts on the surface motion. This effect is seen both on human breasts as well as silicone phantoms.

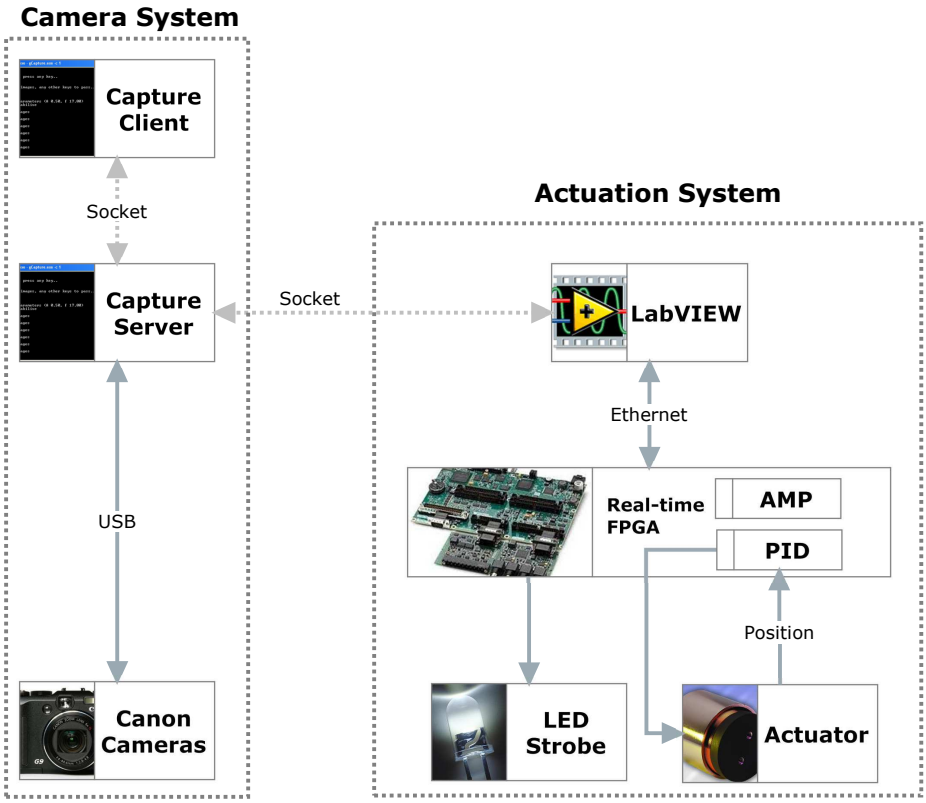

FIGURE 1.6: System diagram of the DIET setup.

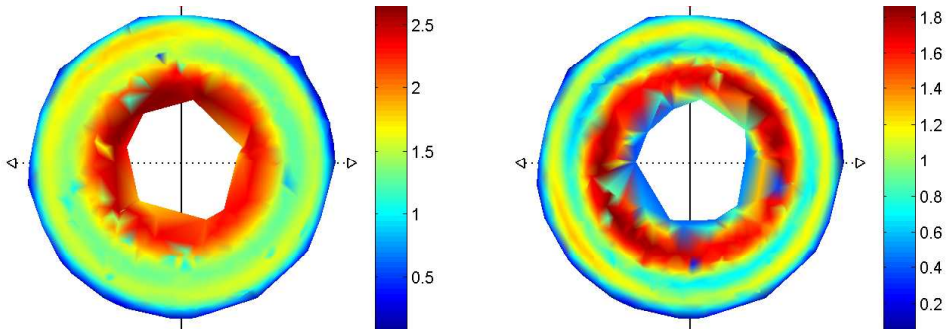

(a) Fundamental frequency 18Hz (b) Nearby frequency 22Hz

FIGURE 1.7: Real displacement amplitude at different actuation frequencies of a 3 kPa phantom. A slight change in actuation frequency can have severe impact on surface motion.

The contrast in stiffness between healthy and cancerous tissues can be maximized when the analysis is carried out around the resonant frequency of the breast tissue, where largest oscillatory responses in surface displacement occur. This amplification, in contrast, can significantly enhance the performance of tumor identification algorithms. Consequently, it is desired to identify the resonant frequencies on each breast prior to imaging. Resonant frequencies can vary significantly in different breasts due to the complex anatomical structures and geometries. The successful identification of such crucial parameter can lead to an increase in performance of the overall system.

Lotz *et al.* [33] have developed a new concept for identifying the tumor's position by solely analyzing surface motions. Some preliminary phantom studies show that such approach is able to outperform the existing system in processing time by omitting the FE simulations. However, this approach requires relatively large surface motions in order to make accurate estimations. Consequently, the imaging should be concentrated around the actuation frequencies that can result in large surface motions.

The resonant frequency, or sometimes called the natural frequency, is the tendency of a vibrating structure to oscillate with larger amplitudes at some frequencies than at others. Hence, prior inspection of the fundamental frequency of a breast using a suitable fundamental frequency detection platform ought to be carried out. A non-invasive platform that could operate in an efficient yet accurate fashion is desired. Once the resonant frequencies are identified, thorough imaging could be carried out around this frequency. A possible new work flow is illustrated in Figure 1.8. This particular approach eliminates the need for any FE simulations.

1.4 Preface

This research presents a non-invasive resonant frequency detection system for soft tissue, particularly designed for the DIET system in breast cancer imaging. This thesis has been organized in the following way.

Chapter 2

begins by laying out the theoretical background of the research, and looks at a number of popular modal testing platforms and vibration sensing modalities. Most importantly, merits and potential pitfalls associated with those methods are identified. This chapter proposes that an imaging sensor fulfills the design requirements.

Chapter 3

assesses the feasibility of the proposed approach through simulation studies using

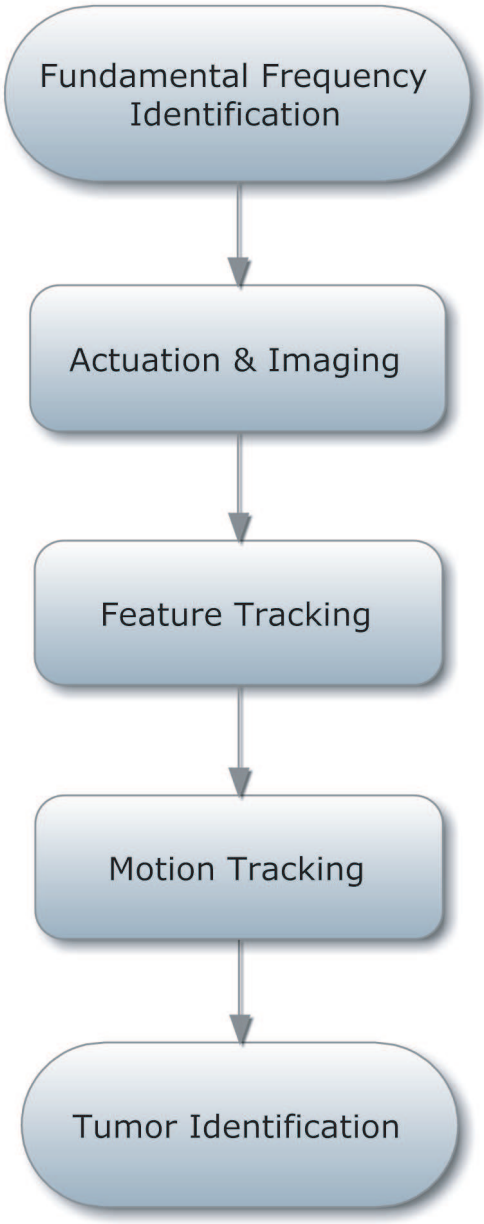

FIGURE 1.8: Proposed DIET work-flow with imaging only diagnosis.

silicone phantoms. Key parameters are investigated and their optimal values are determined. Accuracy of the method is evaluated by comparing results with a reference sensor.

Chapter 4

describes the design and performance of the current implementation. This chapter also reviews the suitability of several other motion recognition algorithms and imaging modalities.

Chapter 5

presents characterization and evaluation of some results from phantom studies as

well as human trials.

Chapter 6

provides conclusions and suggests future work.

Chapter 2

Modal Analysis

This chapter provides an overview of various vibration sensing modalities and different modal analysis platforms. The importance of the modal analysis system is explained first followed by a selection of the most appropriate sensing solution for DIET. A retrospective feasibility study using the selected vibration sensing modality is performed before implementing the modal analysis system.

2.1 Experimental Modal Analysis

In order to identify the resonant frequencies of a breast, it is necessary to assess its vibration response. One common way to investigate dynamic behavior of a structure is through experimental modal analysis. This technique consists of applying a known vibrational excitation to a structure and measuring its output response at different points of interest. The structural resonances can be seen in the response spectra. By analyzing the frequency response, such as using Bode plots, a better understanding of the elastic properties can be obtained.

In a DIET system, the frequency response can be used to identify optimal frequencies for the FE optimization algorithms, or to identify the overall response on the surface and develop alternative diagnostic algorithms. One example of a diagnostic application of modal analysis is to model breasts using simple mechanical systems [34]. Bode plots provide excellent data for system identification. Based on curve fitting of these plots, mechanical model parameters can be identified. The identified stiffness and damping values can lead to diagnostic results.

2.2 Vibration Theory

Vibration is the repetitive, periodic, or oscillatory response of a mechanical system. "Repetitive motions that are regular and occur at relatively low frequencies are commonly called oscillations whereas any repetitive motion, even at high frequencies, with low amplitudes and having irregular and random behavior falls into the general category of vibration" [35]. Usually the terms vibration and oscillation are used interchangeably, as is done in this thesis.

In order for a structure to vibrate, it must have two main characteristics: elasticity and mass. Soft tissue such as the human breast has both characteristics. Previous studies have reported a damped viscoelastic behavior of soft human tissue [36, 37]. Thus, it is safe to assume normal human breast structure would have similar characteristics as a spring-mass-damper system shown in Figure 2.1.

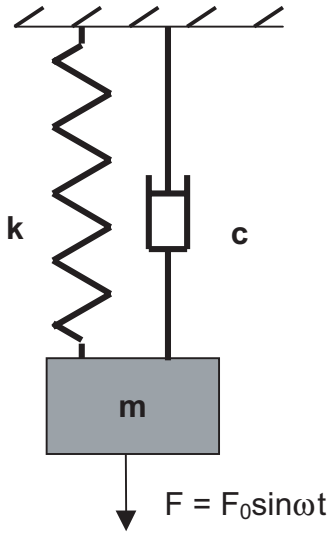

FIGURE 2.1: Damped single DOF system undergoing $F_0 \sin(\omega t)$ excitation, where m is the mass, c is damping and k represents stiffness.

Given motion of a harmonic $\psi(t)$ can be expressed by displacement amplitude A, angular frequency ω and phase delay ϕ.

$$\psi(t) = Asin(\omega t + \phi) \tag{2.1}$$

Equation 2.1 contains three parameters; A, ω and ϕ. During a cycle of vibration, ψ takes on all values between the limits $\pm A$. The rate of vibration cycles, or the number of cycles per unit time, $f = \frac{\omega}{2\pi}$ is its frequency, which has an unit of s^{-1}.

When external time-varying driving force is applied to soft tissue for a period of time; the soft tissue reaches steady state, a regime in which the structure is vibrating harmonically at the same frequency as the driving force.

When applying a harmonic excitation $u(t) = F_0 \sin(\omega t)$ to the single degree-of-freedom (DOF) system, such as shown in Figure 2.1, the equation of motion is shown in Equation 2.2, which then yields Equation 2.3. During steady state, Equation 2.4 and Equation 2.5 are used to describe amplitude A and phase ϕ of the vibrating soft tissue that has mass m, spring constant k and viscous damper of damping coefficient c.

$$F_0 \sin \omega t = m\ddot{x} + c\dot{x} + kx \tag{2.2}$$

$$\ddot{x} + 2\xi\omega\dot{x} + \omega_n^2 x = \frac{F_0}{m} \sin \omega t \tag{2.3}$$

where F_0 is the excitation force; x $\dot{x}$ $\ddot{x}$ are the position, velocity and acceleration; and $\xi = \frac{c}{2\sqrt{km}}$ describes the damping coefficient of the soft tissue.

$$A(\omega) = \frac{F_0}{k} \frac{{\omega_n}^2}{\sqrt{({\omega_n}^2 - \omega^2)^2 + (2\xi\omega_n\omega)}} \tag{2.4}$$

$$\phi = \arctan \frac{2\xi\omega_n\omega}{{\omega_n}^2 - \omega^2} \tag{2.5}$$

where ω_n is the natural frequency of the soft tissue; and ω is the frequency of the input harmonic, or the actuation frequency.

Maximum displacement of the soft tissue occurs when $\omega = \omega_n\sqrt{1 - 2\xi^2}$. Depending on the damping coefficient of soft tissue, maximum displacement would occur around the natural frequency ω_n. An example response is illustrated in Figure 2.2. For relatively small ξ, maximum displacement occurs at a frequency ω that is slightly higher than ω_n. If the system has relatively high damping, response becomes maximum at a frequency ω that is slightly smaller than ω_n. Given the actuation frequency $\omega \approx \omega_n$, large tissue vibration displacements can be achieved.

The relationship between displacement, velocity and acceleration of the soft tissue during harmonic actuation can be obtained through differentiating Equation 2.1 with respect to t, where first differentiation gives the velocity and second differentiation gives the acceleration as shown in Equation 2.6 and Equation 2.7.

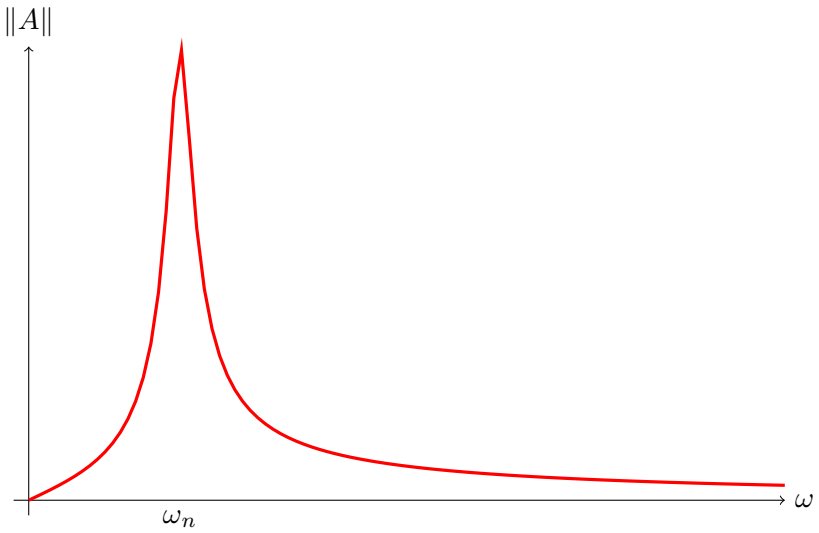

FIGURE 2.2: Ideal frequency response for a single DOF mechanical system, where maximum displacement occurs around its fundamental frequency ω_n.

$$\dot{\psi}(t) = -\omega A sin(\omega t + \phi) \equiv \omega A \cos(\omega t + \phi + \frac{1}{2}\pi) \tag{2.6}$$

$$\ddot{\psi}(t) = -\omega^2 A cos(\omega t + \phi) \equiv \omega^2 A cos(\omega t + \phi + \pi) \tag{2.7}$$

According to Equation 2.6 and Equation 2.7, $\psi(t)$, $\dot{\psi}(t)$ and $\ddot{\psi}(t)$ all vary harmonically with the same frequency. Notably, acceleration leads velocity by $\frac{\pi}{2}$ while velocity itself leads displacement by $\frac{\pi}{2}$. A much more visual illustration using phasors can be seen in Figure 2.3.

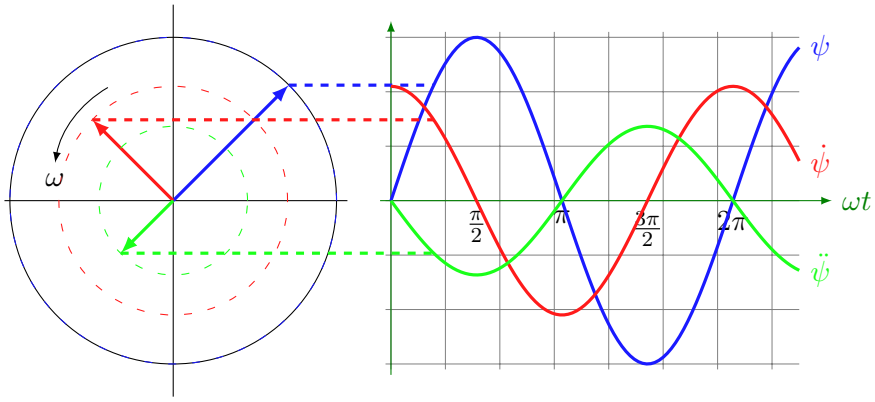

FIGURE 2.3: Phasor relationships between displacement ψ, velocity $\dot{\psi}$ and acceleration $\ddot{\psi}$.

In practice, boundary conditions, also known as initial conditions, tend to have strong influences over the initial values of displacement A and phase ϕ. Different starting experimental arrangements would lead to different initial values for A and ϕ.

2.3 Vibration Sensing

The field of vibration measurement in the domain of industrial, architectural and geological vibrations has already been intensively studied and the associated difficulties are well known. However, vibration measurement on soft tissue, such as human breasts, is a less well-known topic. In order to carry out the modal analysis on a breast surface, an appropriate sensor must be selected for measuring the vibrations.

A wide range of electronic transducers are available for sensing surface vibrations. Some of these sensors are sensitive to the displacement and acceleration while others are sensitive to optical harmonics such as ultrasound and laser. Regardless of their working principles, these approaches can be subdivided into two broad categories, depending on whether or not it has any physical contacts with the vibrating object that is being measured.

Since the main objective of the DIET system is to deliver breast cancer diagnoses in a non-invasive and cost effective manner, it is best to keep the modal testing platform alike. A number of well-known vibration sensing techniques are presented in this section and discussed for their suitability in the DIET context which concerns the question of the sensor deployment: exactly how least invasive, rapid and low cost can the vibration sensing method be?

2.3.1 Piezo-electric Accelerometer

A piezo-electric accelerometer is a device that is frequently used to monitor vibrations. It measures the acceleration at the point where it is attached, converting mechanical acceleration into a proportional electrical voltage signal. Most accelerometers are able to monitor motion occurring along one or more axes. The acceleration sensitivity associated with most accelerometers is only valid for a certain range of frequencies [38]. Hence, a suitable accelerometer must have the appropriate bandwidth that covers all possible DIET actuation frequencies.

Since the accelerometer only measures the acceleration of the object, displacement can only be obtained by performing integrations on the readings. A number of suitable accelerometers are presented in Table 2.1.

Rendon *et al.* have developed a system for studying soft tissue vibrations, presenting a system that uses two ENDEVCO 752A12 accelerometers to map the surface of neck and thorax using the mean power levels of acceleration signal in different frequency bands [39]. Patient's heart beat, breathing movement, snoring sounds are recorded by

TABLE 2.1: A selection of suitable accelerometers for tracking tissue vibrations. Some of the accelerometers offer voltage potentials mV (milli-volts) output while others offer capacitance pC (pico-farads) as the output signal.

Product Model	Weight (gm)	Sensitivity	Frequency Response /Uncertainty ±%
Dytran 3032A	1.5	10(mV/g)	1Hz-10kHz/5%
Dytran 3133A1	0.8	10-15(mV/g))	0.25Hz-10kHz/10%
Dytran 3133A2	0.8	2-3(mV/g)	0.25Hz-10kHz/10%
Dytran 3133A3	0.8	5-7(mV/g)	0.25Hz-10kHz/10%
Dytran 3224A1	0.2	10(mV/g))	1.8Hz-20kHz/5%
Dytran 3225F2	1.0	10(mV/g)	2Hz-10kHz/10%
Dytran 3225F1	0.6	10(mV/g)	1.6Hz-10kHz/10%
Dytran 3225F3	0.6	10(mV/g)	1.6Hz-10kHz/10%
ENDEVCO 22PICOMIN	0.14	0.4(pC/g)	1Hz-10kHz/5%
ENDEVCO 752A12	13	100(mV/g)	1Hz-8KHz/5%
B&K 4374	0.65	0.15(pC/g)	1Hz-26kHz/10%
B&K 4375	2.6	3.1(pC/g)	0.1Hz-16.5kHz/10%

accelerometers attached to the skin. However, such design neglects the additional weight being put onto the skin, as its main intention is to find out the relationships of the power levels between different skin surface areas, not their actual displacements.

Cano *et al.* have developed a system to measure displacement of machine points by merging computer vision and accelerometers [40]. Essentially, the design uses a camera to measure displacements, and compares the results with acceleration measurements. The system is designed to operate on industrial machines with much larger vibrations. The overall complexity of the design also made the approach less appealing to others.

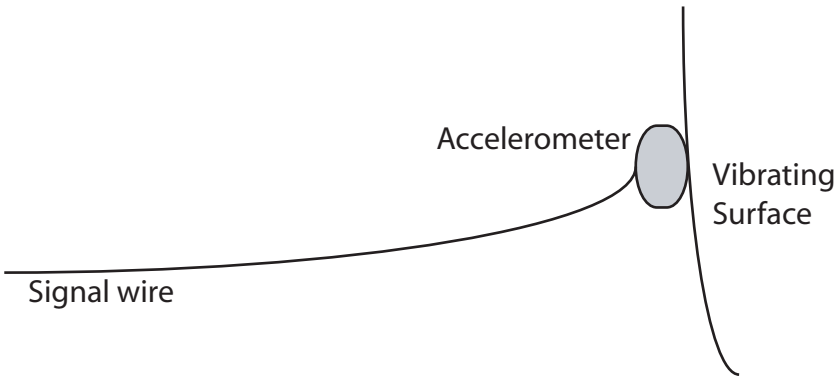

FIGURE 2.4: Example setup for vibration sensing using a compact accelerometer. Note the requriement of contact between the sensor and vibration surface. Not only can this affect the resulting measurements, but also make the testing procedure a lot more complicated.

One of the most difficult aspects of using an accelerometer is finding a method to attach the sensor to the skin. The sensor must be rigidly attached to the skin throughout the actuation process in order to carry out any measurements. Some manufacturers,

such as Dytran, have designed very compact accelerometers that just weigh less than a gram and can be connected to any external data acquisition platform via a thin piece of wire. Since the patients will be lying on their chest, any additional weight attached onto the breast will disturb the surface motion pattern, and this disturbance can lead to incorrect diagnoses. Slight rotation of the accelerometer's sensitive axis by a few degrees will severely affect the acceleration measured. During actuation, there is absolutely no guarantee on whether the accelerometer will stay in the same orientation. In addition, the measurements can be easily affected by the surrounding environment, such as temperature, humidity, frequency of operation and earth gravity.

In a short summary, some of the obstacles associated with using accelerometers are,

- Models with high accuracy are fairly expensive (For example, lower end Dytran 3032 model costs just a little over NZ$200 while ultra light weight ENDEVCO 22PICOMIN itself is valued around about NZ$1500)
- Difficulty in attaching the sensor to the patient's skin and the presence of signal wires may impose inconveniences
- Sophisticated second integrations are required to obtain displacement, especially with low accelerations
- Signal magnitude is position dependent and can be strongly affected by the surrounding environment
- Output is position dependent. For example, rotation of the sensitive axis of the accelerometer by a few degrees from the horizontal axis can produce a much smaller acceleration.

2.3.2 Ultrasound

Ultrasonic vibration sensing is an alternative non-invasive sensing technique. A continuous high frequency ultrasonic beam is emitted towards the moving surface and the reflected beam is captured. Doppler shifts in the received signal can be analyzed to estimate the amplitude and frequency of the vibration. This method is reasonably sensitive to surface movements. Furthermore, the sensitivity can be enhanced by applying various signal modulation schemes to the ultrasonic beam.

Over the years, many have studied such non contact vibration measurement systems using ultrasonic interferometry. Zhao *et al.* have been able to detect amplitudes as little as 30 *nm* using the pulse echo Doppler method [41], while Matar *et al.* have proposed

several other improvements that can be made to increase the sensitivities of ultrasonic vibration sensors [42]. This method would have been much more convincing if the author had considered to test it on various vibrating surfaces that are made of different surface shapes and materials. Yamakoshi *et al.* [26], Matsumura *et al.*[27] and Sinkus *et al.* [28] all have implemented similar systems for detecting inner tissue vibrations based on ultrasound measurements. The performance of these systems is good, but not particularly useful in DIET since they are targeted at inner tissue vibrations.

The energy of the ultrasonic pulse is transmitted in form of a cone along the transducer axis, and the majority of the limitations of ultrasonic sensors are related to this cone-shaped emitting pulse. As shown in Figure 2.5, the further the sensor is positioned from the vibrating surface, the larger the angle of beam, and the larger the surface it is measuring. The reaction time also increases with sensor-to-target distance to avoid a large beam cone diameter. Most accurate detection occurs when the vibrating surface is perpendicular to the transducer's beam axis, and the sensor must be positioned as close as possible to the vibrating surface.

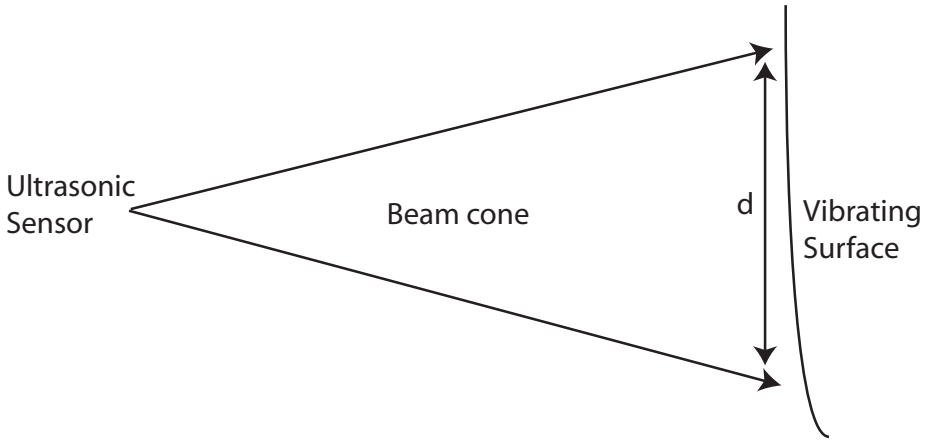

FIGURE 2.5: Example setup for vibration sensing using an ultrasonic sensor. The further the sensor is positioned from the vibrating surface, the larger the beam cone diameter. The area monitored depends on the length of d.

It is difficult for the ultrasonic sensor to discern between the breast surface and its surroundings, because the beam will bounce back as soon as it has reached any obstacles. Previous experiments have indicated that breast surface area close to the actuator tends to have a synchronized motion with the actuator, and thus must be ignored. However, this can be a difficult task as the area covered by the sensor is dependent on the angle of beam as well as the sensor-to-target distance. In order to detect movement of a specific region of interest, precise positioning of the sensor is required. One other possible solution is to employ an array of sensors focusing on the area of interest and average the resulting measurements. But due to the high pricing on accurate narrow beamed

ultrasound transducers (for example, NZ$3000 for a Migatron RPS-412A-10-V [43]), other options must be considered.

2.3.3 Laser Doppler Vibrometer (LDV)

Laser-based remote sensing techniques have emerged and appear to be expanding its applications across the biomedical field; for example, Jenkins *et al.* have used LDV to study anatomical noise vibrations [44], Wang *et al.* have used a similar setup to detect human life signs [45] and Wilson *et al.* have used it to monitor cardiac motions [46]. Smutz *et al.* have used scanning LDV to study vibration transmissibility on animal tissues[47]. Lorenzo *et al.* adopted a similar approach to study local hand transmissibility [48].

The basic LDV employs a two beam laser interferometer. Displacements of a target point can be calculated by comparing the Doppler-shifted beam and its internal reference beam. It has very high performance in terms of processing speed, precision, accuracy and ability to track motion of a relatively small area. Single-point LDV is most commonly used and it is able to measure the small vibrations occurring at a single point without the need for scrupulous setup or surface preparation. Scanning LDV is also popular due to its ability to simultaneously monitor numerous locations for vibrations. However, LDV is only able to detect out of plane motion; that is, motion occurring perpendicular to the vibrating surface.

Apart from its costly nature, some concerns also exist around its safety in a practical clinical environment. Extreme care must be taken when LDV is used, as it is a class II laser device and could potentially harm the eyes. The LDV is the perfect device that can be used for modal testing, but its high cost makes it unsuitable for creating a cost effective cancer screening system. However, it is important to note that LDV is still a good reference sensor for validating the accuracy of other vibration sensors.

2.3.4 Fibre Optic Vibrometer (FOV)

Optical fibres have been used as sensors for measuring vibration amplitude and several other physical parameters. There are two distinct types of optical fibre sensors:

- Intrinsic, the fibre is used as a sensing element, where the parameter of interest affects the light propagation through the fibre
- Extrinsic, the fibre is used to relay data from one end to another.

Chitnis *et al.* have designed an extrinsic optical sensing system that is able to detect displacement as little as $0.1\mu m$ [49]. Dib *et al.* have designed a similar system that would work with a flat vibrating surface with an accuracy of $2nm$ [50]. Alberto *et al.* have designed a calibration scheme to enhance the design by Dib *et al.* to work on non-spatially uniform reflectivity and non-flat vibrating surface with an accuracy of $1\mu m$ [51–53]. However, all approaches of this kind carry with them some serious limitations in a clinical environment. For example, the sensor needs to be repositioned and calibrated manually for every trial, and this can seriously reduce the efficiency of a screening session.

Most of the displacement vibration fibre optic sensing methods are of extrinsic type. This approach utilizes optic fibre cables that are placed at a distance d away from the vibrating surface as shown in Figure 2.6. A light emitting source can then transmit light pulses along one fibre to the vibrating surface, and the other fibre picks up the light and transmits it back. At the receiving end, the light is detected by a photodiode. There are many design variations, but all based on the same principle, light intensity captured by the receiving end is directly proportional to distance d. Ideally, the vibrating surface should be perpendicular to the fibre axis for maximum accuracy.

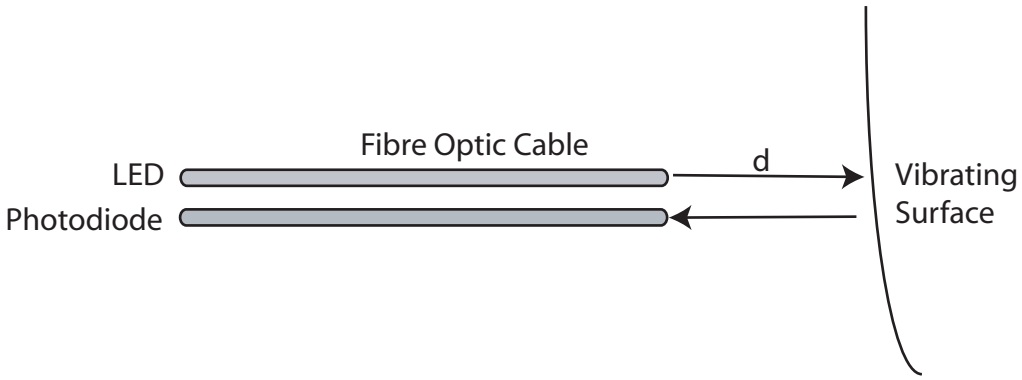

FIGURE 2.6: Example setup using an extrinsic fibre optic sensor for vibration sensing, where d is the fibre-to-target distance. Such distance can strongly affect the sensitivity and performance of the overall system.

Although there is no strict requirement on the fibre-to-target distance, according to Alberto *et al.*, uncertainty drops when working with longer distances d. Sensitivity increases when working with shorter distance d. In other words, the sensor working position has to be chosen as a compromise between the sensitivity and the uncertainty since they both increase for shorter fibre-to-target distance d. Moreover, a reference sensor should be used for calibrating the photodiode. For the modal testing platform, this could impose some problems. Under a clinical environment, it is unpractical to work with long fibre-to-target distances due to a compact build requirement for the DIET setup. Manual adjustments of fibre cables to make sure they stay perpendicular to the vibrating surface can also be challenging. This procedure may need to be repeated

for every imaging session. Last but not least, the performance of fibre optic sensors on soft tissue is unclear, and may require further investigations.

There are commercial FOV products which are far more economical compared to LDV devices yet have similar accuracy, but its setup during clinical trials will be rather difficult.

2.3.5 Optical Image Sensor

Nearly all the sensors described in this chapter can only measure 1D motion, that is, movements occurring along one particular axis, such as the out of plane motion occurring perpendicular to the vibrating surface. When the breast undergoes an actuation force, its vibrational response can be far more complicated than from a single plate, which most of those sensors are designed to measure. Therefore, multiple sensors may be required to capture motions occurring in different axes. However, this introduces further problems: unless the sensor's sensitive beam is in parallel with the particular axis of interest, precise movements in that axis cannot be measured. This is especially difficult with Z-axis measurements due to the presence of the actuator setup, such as shown in Figure 2.7.

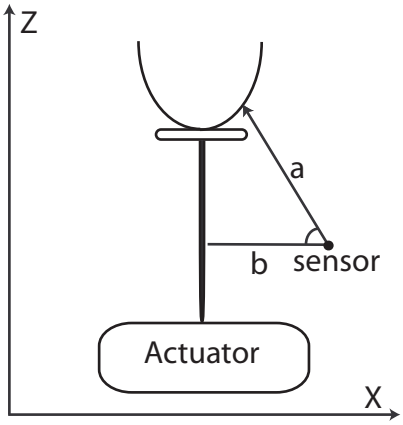

FIGURE 2.7: Difficulty in measuring Z axis motion associated with using sensors that are capable of measuring 1D motion, where a is the sensor's sensitive axis and b is the nearest possible location for sensor deployment. As a direct result, the measurements can only be done at one angle.

Digital (CCD or CMOS) image sensors are becoming increasingly popular due to their low costs. Advances in image processing techniques in recent decades have made this approach very versatile and robust. The image contains 2D information regarding the movements in any 2 axes depending on the location of the camera. This is very beneficial since the vibration of breast volume occurs in more than one axis. With active research on fiducial tracking and skin tracking algorithms, performance of the motion tracking system is being continuously improved. Fiducial markers have greatly enhanced

its performance by allowing the camera sensor to monitor movements occurring at different locations on the surface simultaneously. Each fiducial marker has the equivalent functionality of a point-vibration measuring device, such as LDV, fibre optic sensor, or ultrasound. Moreover, one has the choice of evaluating a Region Of Interest (ROI) of an arbitrary size on the breast surface. Instead of altering any equipment setups, this is achieved easily in software by ignoring fiducial marker movements in unwanted regions after the fiducial tracking stage. On the contrary, such ROI evaluation feature is unavailable with other sensors mentioned in this chapter.

2.4 Sensor Comparison

The benefits and disadvantages of using each sensor are shown in Table 2.2. Notably, digital image sensor and accelerometer are the only ones that can detect 3D movements with just a single sensor. Whereas the others would require multiple sensors to measure 3D movements.

Despite the fact that some of these sensors require complicated setups and manual calibration, most of them are effective and accurate in measuring small oscillations, with some more expensive than the others. Apart from the accelerometer, all sensors are able to operate in a non-invasive manner.

The digital image sensor is the most economical solution since it makes full use of the existing imaging setup in the DIET system. The LDV on the other hand is the most expensive solution. It is important to note that, apart from the digital image sensor, all others could only measure displacement at a given point on the surface. This means multiple sensors will have to be deployed in order to measure displacements at different locations on the surface.

2.5 Summary

Popular vibration sensors, such as accelerometers, laser vibrometers, ultrasonic and fibre optic vibration sensors are all not suitable in this application due to their invasiveness, cost or both.

Based on the availability of imaging devices in DIET, the most cost-effective solution would be to conduct modal analysis using the existing imaging devices. A frequency sweep on the breast is conducted before the DIET imaging session. Since these imaging devices can guarantee the absence of contact, a non-invasive yet cost-effective modal

TABLE 2.2: Comparison of a list of vibration sensors.

Accelerometer	
• Accurate • Measures 3D motion at a point	• Invasive and difficult to attach • Measurements can be affected by the surroundings • Cannot measure displacement • Moderately expensive
Ultrasound	
• Non-invasive	• Only measures 1D motion at a single point • Setup and calibration are complicated • Cannot distinguish between the object and background • Narrow beam sensors are expensive
LDV	
• Very accurate • Non-invasive • Simple setup	• Health & Safety concern Only measures 1D motion at a single point • Very expensive
FOV	
• Very accurate • Non-invasive	• Setup and calibration are complicated • Only measures 1D motion at a single point • Accurate FOV sensor is very expensive
Digital Image Sensor	
• Good accuracy • Non-invasive • Able to detect 3D motion in a given region Make use of the current imaging setup	• Accuracy depends on the image processing algorithm used

testing platform can be established. This approach will be tested in the following chapters.

Chapter 3

Retrospective Feasibility Study

This chapter details the feasibility studies using the vibration sensing modality selected in the previous chapter. A number of objectives are defined and a list of optimal parameters are determined from the simulation studies. Part of the research described here has been presented at IEEE EMBC 2010 [54].

3.1 Feasibility Study Objectives

A camera-based modal testing system that can operate in a time efficient manner using the least amount of resources is desired. Conducting necessary feasibility studies prior to implementing a preliminary design based on an image-based vibration sensor is important as there are several unknown parameters that require further investigations. These are i.e. the number of images to capture during a single oscillation period and the number of imaging devices to use.

In order to obtain the full frequency response of the breast, an appropriate method for calculating its response at a particular actuation frequency is required. The feasibility study described in this chapter is carried out with the intention to establish a frequency response sensing method that has following characteristics:

- minimum number of image captures in a single oscillation period to maximize speed
- minimum number of imaging devices to achieve a simple, yet cost-effective system.

The frequency response is identified through analyzing fiducial motion patterns based on these underlying assumptions:

- Stiffness of healthy breast volume is relatively homogeneous
- All fiducial markers move in an elliptical path
- Largest fiducial motion occurs at the breast's fundamental frequency.

Once the appropriate calculation method is chosen, full frequency response over a selected spectrum can be obtained by repeating the analysis on all frequencies that are to be examined.

In short summary, the primary objective of the feasibility study is to identify an appropriate method for calculating a response value based on evaluating surface motion. Ideally, such a method should be able to generate a satisfactory approximation of the real average frequency response using the minimal amount of image captures with the least amount of imaging resources.

The software package MATLAB^{TM} is used to simulate results obtained from different number of image captures as well as different number of cameras. Quality of the method may be assessed by how accurate the predicted harmonic frequencies are compared to the results obtained from a single-point LDV.

3.2 Fiducial Marker Movement

During a DIET imaging procedure, fiducial markers are randomly applied onto the breast surface. These fiducial markers act as grid points allowing precise measurement of vibrations in 3D space. Knowledge of the motion paths generated by these markers during actuation is important to minimize the number of image captures, and is the main focus of this study.

As shown in Figure 3.1, the motion path of a fiducial marker during a single oscillation on a phantom breast resembles the shape of an ellipse. This steady state harmonic response is also seen in FE simulations [31] as well as human trials. Moreover, the magnitudes of the major and minor axes of the ellipse can be strongly influenced by the actuation frequencies. For example, the particular motion pattern of the phantom shown in Figure 3.1 recorded at its fundamental frequency is approximately 8 times larger than the motion pattern at a nearby frequency.

Thus, by studying these elliptical patterns at various frequencies, one may be able to draw conclusions on where the fundamental frequency is. Theoretically, magnitudes of the major and minor axes of all the elliptical motion paths should be maximized at the fundamental frequency. However, as seen in most experiments, it will also depend

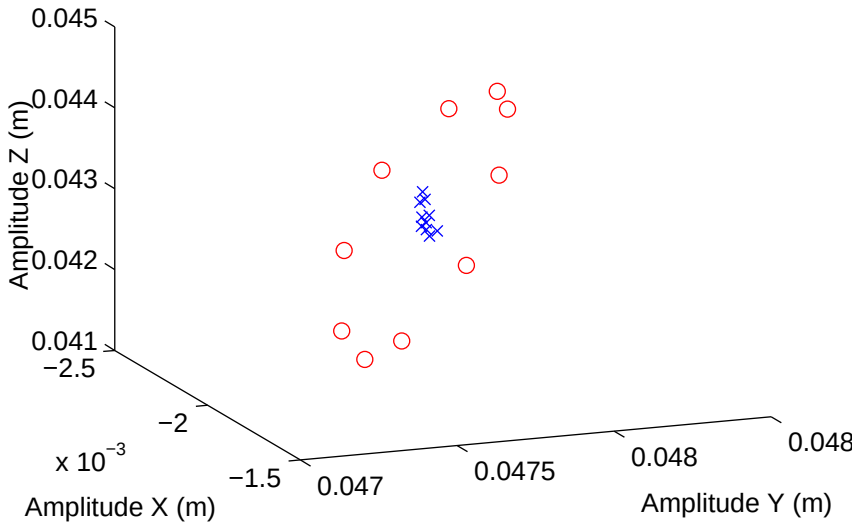

FIGURE 3.1: Elliptical-shaped oscillatory movement of a fiducial marker seen on a silicone phantom breast tracked in 10 discrete images. The fundamental frequency of this phantom is centered around 50Hz (**o**), motion is also recorded at a nearby frequency 35Hz(**x**). The motions are approximately 8x larger at this fundamental frequency

on the location of the fiducial marker. Fiducial markers that are close to the actuator tend to have synchronized motion with the actuator. On the other hand, markers near the base of the breast, have very little motion throughout the frequency sweep as they are attached to a fixed surface. Consequently, motions seen at these locations will be relatively constant, independent of the actuation frequency. Therefore, when analyzing the characteristics of the ellipses on the surface, these factors must also be accounted for.

3.3 Data Interpolation

In order to evaluate the performance of a specific number of image captures per cycle on a particular phantom, experimental imaging sets with different image numbers are required. Various interpolation techniques can be used to up-sample the existing experimental data and then down-sample to simulate the output with the desired number of samples/captures. There are readily available and post-processed data recordings from past experiments, which contain fiducial positions over the entire breast on various phantoms.

An example of a soft healthy phantom Mk3 imaged at a F=16Hz, A=0.5mm actuation setting is shown in Figure 3.2. These data were acquired by 5 cameras at 10 images per oscillation period. The actuation path of the fiducials resembles an ellipse

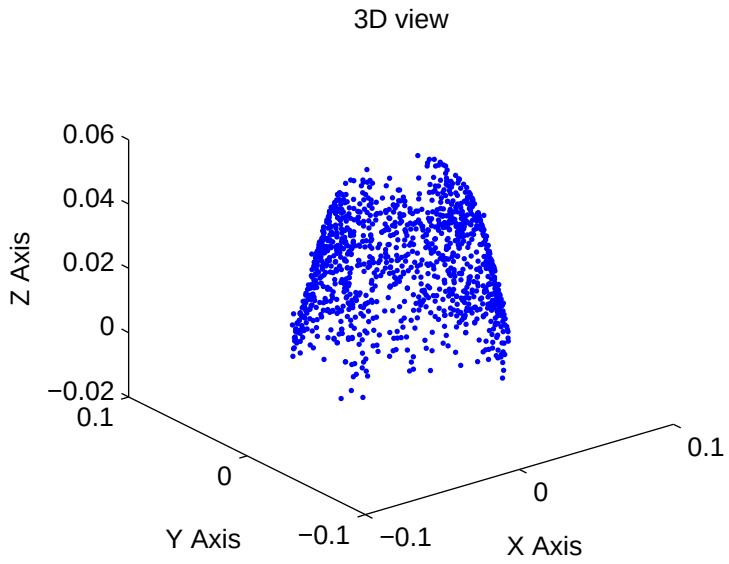

FIGURE 3.2: Reconstructed 3D motion data acquired a silicone phantom.

and can thus be robustly interpolated to generate more synthetic images. It is thus possible to generate additional data entries by interpolation of the 10 measurements per cycle to N measurements per cycle. Depending on the number of required test cases $(n_1, n_2, ..., n_k)$, N is chosen to be the Least Common Multiple LCM of the number of test cases. Appendix A provides a detailed explanation on LCM and its importance in the data interpolation process.

Examples of possible number of image captures per cycle that can be decimated from N images per cycle are shown in Table 3.1. If existing 10-sample data are chosen to be interpolated to $N = 24$ samples, one will be able to study the behaviors at $(n_1, n_2, ..., n_k) = 1, 2, 3, 4, 6, 8, 12, 24$ images per cycle. But the accuracy of simulation studies will heavily rely on the interpolation method that is used.

The impact of various numbers of image captures per cycle on the magnitude of elliptical axes is to be investigated in detail as this is the key for evaluating responses at given frequencies at a minimum number of samples.

Simulations on $(n_1, n_2, ..., n_k) = 2, 3, 4, 5, 6$ are performed and N is chosen to be 60 as it can be used to decimate to 2,3,4,5,6 images per cycle. Interpolation techniques tested were linear and elliptical, which are described in more detail here.

3.3.1 Linear Fitting

In 2D space, a line can fitted between two points (x_0, y_0) and (x_1, y_1) by Equation 3.1, where x is a value between(x_0, x_1) and the value of y defines the value along the straight

TABLE 3.1: Possible image captures per oscillation cycle that can be simulated with N number of images per cycle through decimation. N is the least common multiple of the list.

N $\equiv lcm(...)$	Image captures per cycle that can be studied $(n_1, n_2, ..., n_k)$
4	1,2,4
6	1,2,3
8	1,2,4,8
10	1,2,5,10
12	1,2,3,4,6,12
24	1,2,3,4,6,8,12,24
36	1,2,3,4,6,9,12,18,36
48	1,2,3,4,6,8,12,16,24,48
60	**1,2,3,4,5,6,8,10,12,15,20,30,60**
72	1,2,3,4,6,8,9,12,18,24,36,72
84	1,2,3,4,6,7,12,14,21,28,42,84
90	1,2,3,5,6,9,10,15,18,30,45,90
96	1,2,3,4,6,8,12,16,24,32,48,96

line.

$$y = y_0 + (x - x_0)\frac{y_1 - y_0}{x_1 - x_0} = \frac{(x - x_0)y_1 + (x_1 - x)y_0}{x_1 - x_0} \tag{3.1}$$

Once the equations for the lines are known, additional points on the line can be interpolated easily. Full 3D interpolation is achieved by performing the 2D interpolation method on data from each axis.

3.3.2 Elliptical Fitting

As seen earlier in Section 3.2, a typical fiducial marker moves in an elliptical path. Fitting the group of samples with an ellipse would generate much more realistic samples.

Recall that a point in 3D space $\begin{pmatrix} x \\ y \\ z \end{pmatrix}$ on an ellipse with center point $\begin{pmatrix} x_0 \\ y_0 \\ z_0 \end{pmatrix}$, amplitude $\begin{pmatrix} A_x \\ A_y \\ A_z \end{pmatrix}$ and phase $\begin{pmatrix} \phi_x \\ \phi_y \\ \phi_z \end{pmatrix}$ can be represented by Equation 3.2.

$$\begin{pmatrix} x \\ y \\ z \end{pmatrix} = \begin{pmatrix} x_0 \\ y_0 \\ z_0 \end{pmatrix} + \begin{pmatrix} \sin(\omega t + \phi_x) & 0 & 0 \\ 0 & \sin(\omega t + \phi_y) & 0 \\ 0 & 0 & \sin(\omega t + \phi_z) \end{pmatrix} \begin{pmatrix} A_x \\ A_y \\ A_z \end{pmatrix} \tag{3.2}$$

The parameters A and ϕ of an ellipse are obtained by using an integral-based fitting method [55]. The method is convex and not starting point dependent. It is described here on the example of fitting a sinusoidal motion path. Recall that a harmonic motion can be described by Equation 3.3.

$$u = A\sin(\omega t + \phi) \equiv A[\sin\omega t\cos\phi + \cos\omega t\sin\phi] \tag{3.3}$$

By integrating Equation 3.3 with respect to ωt between ω_{t_0} and ω_{t_1}, Equation 3.4 is obtained.

$$\int_{\omega_{t_0}}^{\omega_{t_1}} u\, d\omega t = A\cos\phi[-\cos\omega_{t_1} + \cos\omega t_0] + A\sin\phi[\sin\omega_{t_1} - \sin\omega_{t_0}] \tag{3.4}$$

The integral of the displacement $\int u$ can be approximated by the area under the curve of the experimental displacements.

$$\int_{\omega_{t_0}}^{\omega_{t_1}} u\, d\omega t = u_m(_{\omega t_1} -_{\omega t_0}) = \frac{u(t_1) + t_0}{2}(\omega(t_1 - t_0)) \tag{3.5}$$

where u_m is the mean displacement between t_0 and t_1. Equation 3.5 consists of two unknowns $x = A\cos\phi$, $y = A\sin\phi$ and can be written in the form

$$d_0 = xC_1 + yC_2 \tag{3.6}$$

where d_0 is the area under the curve between samples $u(t_0)$ and $u(t_1)$, $C_{01} = -\cos\omega_{t_1} + \cos\omega_{t_0}$ and $C_{02} = \sin\omega_{t_1} - \sin\omega_{t_0}$.

Equation 3.6 can then be repeated for other time steps to obtain a set of linear equations. The optimization problem is thus reduced to solving a set of linear equations:

$$d = B\begin{pmatrix} x \\ y \end{pmatrix} \tag{3.7}$$

After solving Equation 3.7 for $\begin{pmatrix} x \\ y \end{pmatrix}$, phase angle ϕ and amplitude A can be obtained by solving the following equation.

$$\begin{pmatrix} x \\ y \end{pmatrix} = A\begin{pmatrix} \cos\phi \\ \sin\phi \end{pmatrix} \tag{3.8}$$

Similar to the linear interpolation approach, full 3D interpolation using the ellipse method is achieved by performing the interpolation on data from all three axes: first A_x, A_y, A_z and $\phi x, \phi y, \phi z$ are identified, then the desired number of samples can be generated with Equation 3.2.

3.3.3 Results

Both interpolation techniques are compared. As shown in Figure 3.3, for certain input patterns that have very little or irregular motions, elliptical fitting is able to generate much more realistic motion than linear interpolation. Furthermore, noisy measurements can be filtered more easily by knowing the shape of the motion path. With good quality input data, both methods are able to generate additional synthetic motion samples. Therefore, based on the assumption that all fiducial markers shall move approximately in an elliptical pattern, ellipse interpolation is preferred.

3.4 Frequency Response Analysis

Frequency responses obtained by evaluating displacement of fiducial markers at different frequencies can be used to assess the modal response of the system.

This study proposes three types of methods for calculating response at a given actuation frequency: 1D, 2D and 3D analysis. All three analyses are based on maximum displacement found in motion pattern of a fiducial marker in an oscillation cycle. Their methodology and performance is discussed in this section.

- 1D displacement analysis with data from a single axis, Δx or Δy or Δz
- 2D displacement analysis with data from 2 axes, Δxy or Δxz or Δyz
- 3D displacement analysis with data from all 3 axes, Δxyz.

The main difference between these methods lies in how many dimensions of the input data the computation requires. For example, 2D XZ analysis on motion pattern illustrated in Figure 3.4 would require measurements in both X and Z axis; that is, Δx and Δz are used to determine the response at a particular frequency.

Given the elliptical fitting technique is able to generate relatively realistic motion data in an efficient manner, previous experimental data can be interpolated from 10 measurements to 60 measurements per oscillation cycle. This enables simulations of

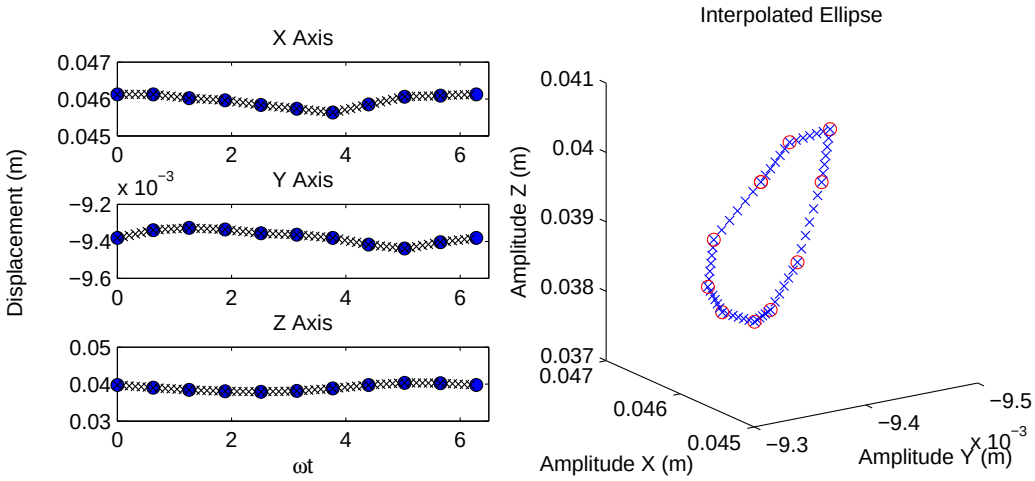

(a) An example to show that linear interpolation may become inadequate when input motion data is less than ideal. XYZ axis coordinates are linearly fitted and interpolated from 10 samples to 60 samples. Interpolated data points (**x**) with input (**o**).

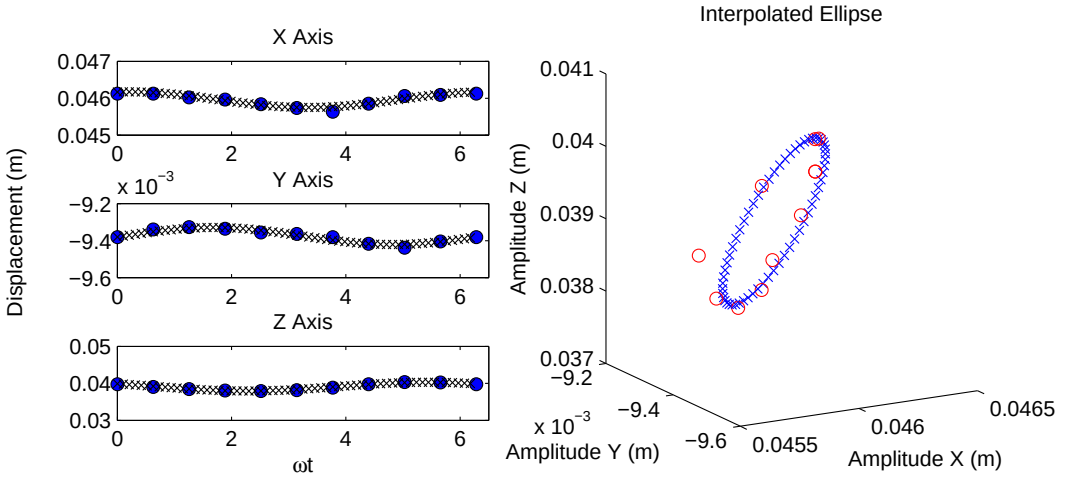

(b) An example to show that ellipse interpolation will be able to generate sensible data regardless of the quality of input motion data. XYZ axis coordinates are fitted with an ellipse and interpolated from 10 samples to 60 samples. Interpolated data points (**x**) with input (**o**).

FIGURE 3.3: Examples comparing linear and elliptical interpolation. Notably, the elliptical approach is able to interpolate in a sensible manner.

multiple numbers of capture settings. As shown in Figure 3.4, 3D data is interpolated to have 60 measurements. Δx Δy Δz represent the largest displacements of a selected fiducial marker in one oscillation cycle measured in the X Y Z directions respectively.

It is interesting to note that almost all fiducial markers move in a particular pattern that contain a relatively dominating Δz component due to the same direction of actuation force. However, depending on the geometric properties of the breast volume, Δx and Δy can occasionally become much larger than Δz. Large motions occurring in the X or Y direction, which are perpendicular to the actuation axis, are most likely induced by significant compression to the breast volume. Therefore, the characteristics can be

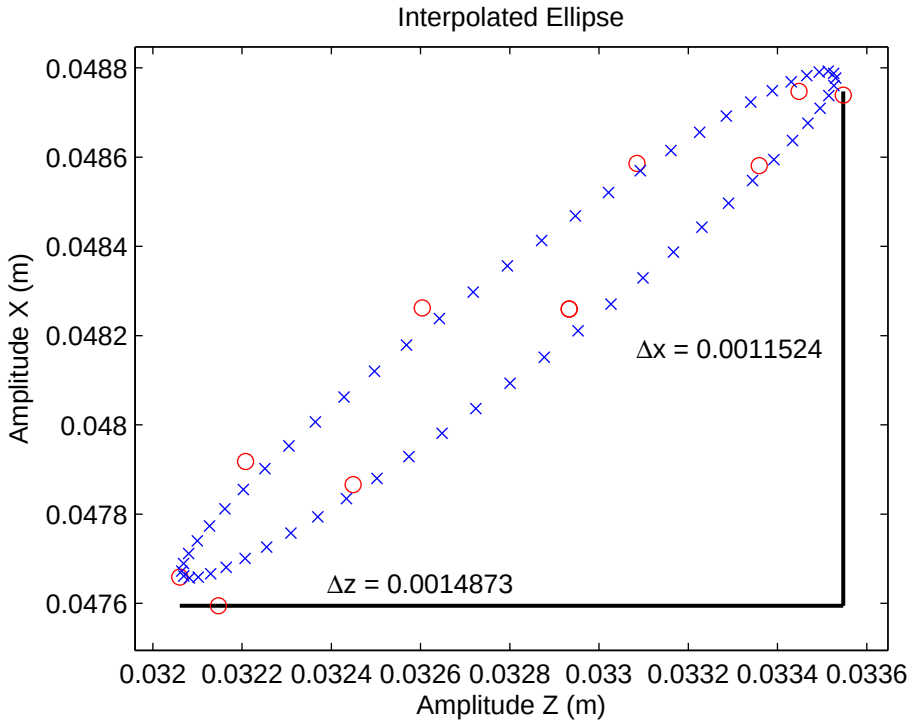

(a) A typical fiducial pattern observed in the XZ plane.

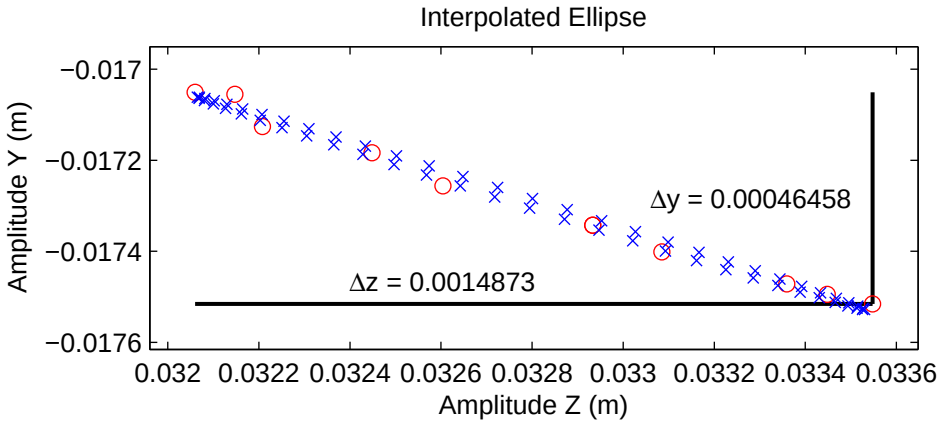

(b) A typical fiducial pattern observed in the YZ plane.

FIGURE 3.4: Typical fiducial pattern displacements along all three axes in the XZ and YZ planes with equal scale, where Δx, Δy and Δz are displacements along X, Y and Z axes, respectively.

identified in a much more accurate manner with displacements measured in 2 or more dimensions.

3.4.1 1D Displacement Analysis

In 1D displacement analysis, only one of the 3D components of a given fiducial marker motion path is registered. This method simulates responses that can be obtained by a data acquisition platform with 1D motion capturing capability, such as:

- 1 camera
- 1 accelerometer
- 1 LDV
- 1 fiber optic sensor
- 1 ultrasound sensor.

For example, studying the motion in the X axis only would require to use Equation 3.9. Δx is computed for all fiducial patterns found in a specified region and the largest is selected to represent the response at this actuation frequency.

$$\begin{aligned} \Delta(x) &= max(\Delta x) \\ \Delta(y) &= max(\Delta y) \\ \Delta(z) &= max(\Delta z) \end{aligned} \tag{3.9}$$

This is the simplest method, but is also the most limited. The major pitfall is that frequency responses can differ greatly depending on the coordinate direction being monitored. Selecting the correct axis to conduct motion sensing is not as trivial as it seems. In certain occasions, one component may play a more dominant role at certain frequencies while others dominate at other frequencies. This can be either due to equipment arrangement or simply variability in geometrical shapes of the breast volume.

3.4.2 2D Displacement Analysis

In 2D displacement analysis, any two out of the three coordinate directions are evaluated. This method is designed to simulate responses captured by 2D motion capable data acquisition platforms; such as:

- 1 camera
- 1 accelerometer (3-axis)
- 2 LDVs
- 2 optic sensors
- 2 ultrasound sensors.

For example, displacement Δx (horizontal) and Δz (vertical) can be used to investigate frequency responses. Results are calculated for every fiducial marker found in a specific region and the largest of the two is computed using Equation 3.10.

$$\begin{aligned} \Delta(xy) &= max(max(\Delta x), max(\Delta z)) \\ \Delta(xy) &= max(max(\Delta x), max(\Delta y)) \\ \Delta(yz) &= max(max(\Delta y), max(\Delta z)) \end{aligned} \tag{3.10}$$

3.4.3 3D Displacement Analysis

During 3D displacement analysis, Equation 3.11 is used to determine the maximum displacement. It evaluates full 3D motion of the fiducial movement, that is, motion occurring simultaneously in X Y Z axes. The following sensing setups are able to generate equivalent results.

$$\Delta(xyz) = max(max(\Delta x), max(\Delta y), max(\Delta z)) \tag{3.11}$$

- 2 cameras (Current DIET system employs 5 cameras to reconstruct the entire breast volume for full 3D analysis)
- 1 accelerometer (3-axis)
- 3 LDVs
- 3 optic sensors
- 3 ultrasound sensors.

As can be seen from these three cases, different levels of accuracy but also complexity are achievable with the level of accuracy required. Using a single camera of the existing setup enables 2D sensing without added complexity. If it turns out that an extra dimension is required, a second camera can always be added.

3.5 Simulation Study

The 1D, 2D and 3D methods outlined in the previous section are tested using images from a phantom imaging database which consists of images acquired from experiments carried out previously. The performance of using a single camera is assessed on a number of healthy as well as cancer simulating phantoms. A healthy 3kPa soft phantom is considered to have the best representation of human breast tissue, hence its results are presented in this section. Simulation results from other phantoms can be found in Appendix B.

The two system setups that need to be evaluated in this study are

- Number of cameras required for robust 2D sensing
- Number of image captures per oscillation cycle.

3.5.1 Number of Cameras

The number of cameras required to determine an accurate representation of the frequency response depends on whether 1D, 2D or 3D analysis is employed, and on the level of homogeneity of the observed breast. Images captured by a single camera contain displacements in 2 directions. This data can be used for 1D as well as 2D analysis. When carrying out a 2D analysis, depending on where the camera is positioned, motions occurring in the XZ plane, YZ plane, or XY plane are able to be captured. Unlike 1D or 2D analysis, 3D information can only be obtained if images are taken simultaneously from different angles; more specifically, imaging will be needed from two locations. Consequently, this has implications on the number of cameras required.

Since the least amount of imaging devices is desired, methods which use a single camera are to be considered first. Out of all methods, 2D analysis appears to be the most attractive candidate as it can be operated with just a single camera. However, if the area covered by a single camera is insufficient to determine the harmonics, additional cameras would have to be brought in.

With the existing 3D phantom data, a Region Of Interest (ROI) such as the one shown in Figure 3.5 is applied to mask out any fiducial markers that should be disregarded by the single camera. Such ROI only examines a portion of the breast and neglects fiducial movements in unwanted regions as defined in Section 3.2. These are the area near the top and bottom of the phantom. By altering the ROI confinement, different camera positions can be simulated. This provides accurate assessments of whether it

is possible to use a single camera with limited field of view for detection. The frequency response is obtained by computing relative maximum displacement values from all the fiducial movements found in such ROI over all actuation frequencies.

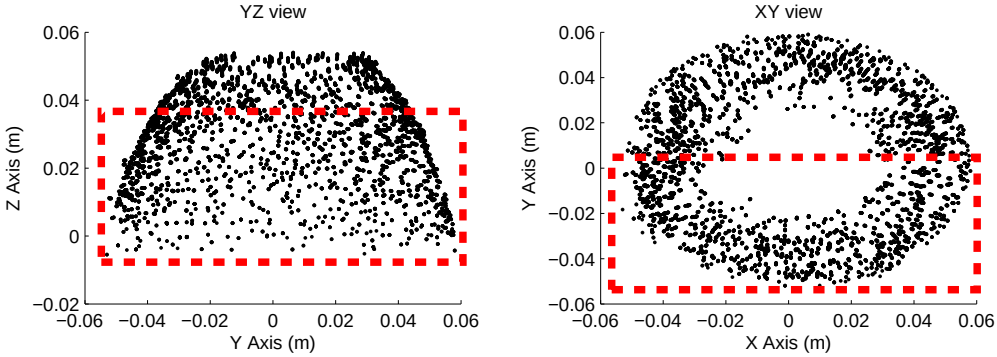

(a) Confinement observed in the YZ plane.

(b) Confinement observed in the XY plane.

FIGURE 3.5: Confinement to simulate the view of a single camera. Areas near the chest wall (bottom) and the actuator (top) are neglected.

3.5.2 Number of Images

The number of images required per oscillation cycle plays a very important role as it can affect the results of detection. Since the requirement is to use least amount of images, the system should capture at a minimum number of images that does not compromise the quality of results.

The maximum displacement for an ellipse is the maximum difference in amplitude between any two samples. Figure 3.6 shows obvious effects that different image captures per oscillation cycle may have on the maximum displacement. For example, due to the elliptical shape, displacement obtained by 2 images per cycle would be maximized if the first image is taken at $\phi = 0.25T$ or $\phi = 0.75T$. More specifically, displacement is at its minimum when $\phi = 0$. However, 3 captures or more are not so much affected by the value of starting phase ϕ. Therefore, a minimum of 3 image captures per oscillation cycle is desired.

Since the imaging does not necessarily start at $\phi = 0$ during the oscillation cycle, different possible starting points must be evaluated. For example, if there are 60 captures in one oscillation cycle, there are 60/k different starting points, where k is the number of images taken (due to cyclic behavior). By repeating the appropriate analysis for a range of different starting points, a distribution of maximum displacements at a particular actuation frequency is obtained. 90th percentile of the distribution represents the best case and 10th percentile the worst case.

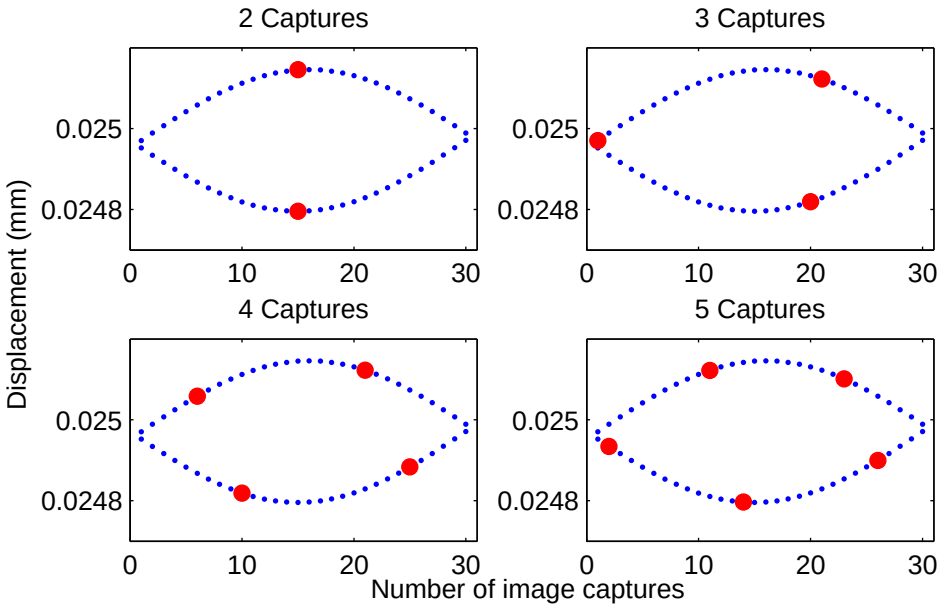

FIGURE 3.6: Impact of different numbers of image capture per oscillation cycle and its ability to reinterpret the ellipse. Motion path of the ellipse obtained by folding the sinusoid response at its half point. As shown in red dots, imaging may start at a random position; therefore there is absolutely no guarantee if the desired number of captures is sufficient to capture the shape of the ellipse.

The optimal number of captures should have a tight distribution between the worst and the best case. In the worst case scenario, the displacement measured at the modal frequency could be lower than at another frequency, only due to a lack of samples over one cycle. Therefore, in the worst case, one should still able to identify the fundamental frequency. To evaluate the minimal number of images required, 2, 3, 4 and 5 images are used to calculate displacements. The 90th, 50th and 10th percentile results at each frequency are calculated and compared.

3.5.3 Results

1D analysis results gathered from a soft 3kPa healthy phantom are shown in Figure 3.7. Evidently, it demonstrates the inadequacy of 1D analysis. Simply looking at the motion in a single direction will not be able to reveal the true response of the vibration. All 3 cases in the 1D analysis can successfully identify the location of first harmonic, but fails to agree on the presence of a second harmonic. Notably, 1D Δx and 1D Δz analysis have larger peak values compared to 1D Δy. 1D Δz analysis seemed to have completely missed the second harmonic. This behavior has also been seen on other phantoms.

On the contrary, as shown in Figure 3.8, 2D analysis is sufficient to reveal locations of both harmonics. The locations are also confirmed by a full 3D analysis. Therefore, 2D

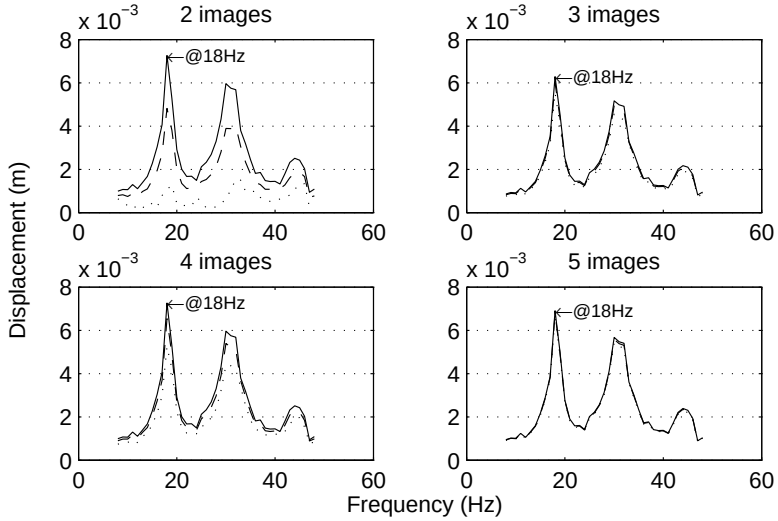

(a) 1D analysis with $Max(\Delta x)$.

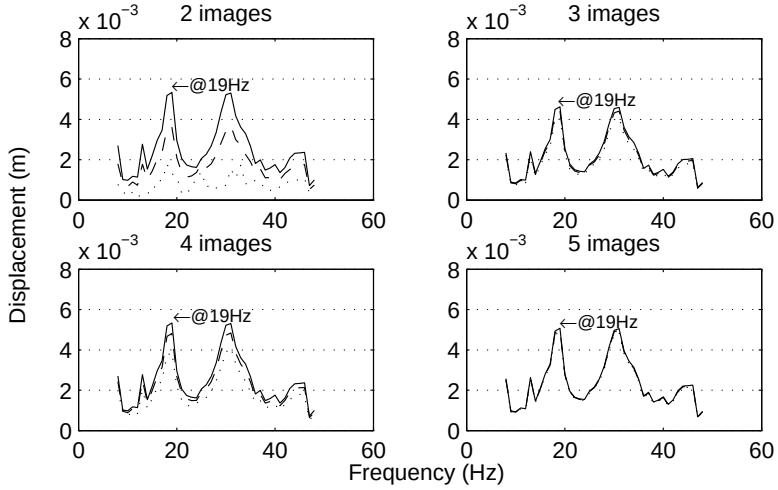

(b) 1D analysis with $Max(\Delta y)$.

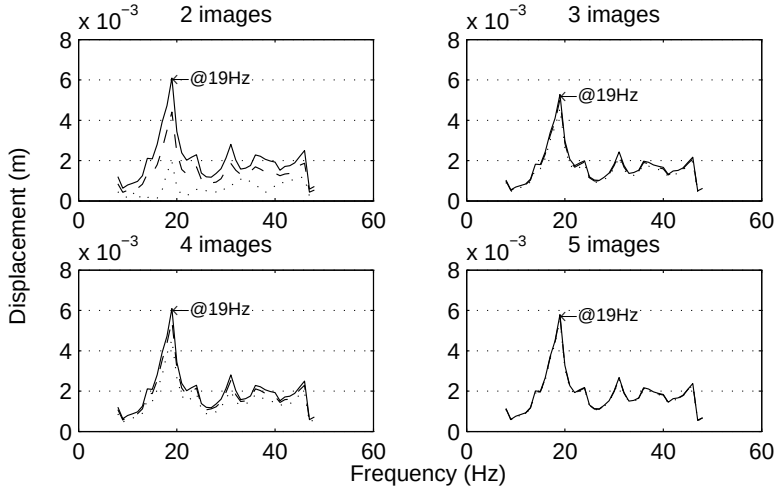

(c) 1D analysis with $Max(\Delta z)$.

FIGURE 3.7: 1D analysis for 2,3,4,5 captures on a healthy 3kPa soft phantom, where Δx, Δy and Δz are displacements along X, Y and Z axes, respectively. 90th percentile (solid) represents the best case and 10th percentile (dotted) indicates the worst case.

analysis is the most optimal selection for determining frequency response with a single camera.

With the number of image captures increasing, the distribution of 90th percentile best case and 10th percentile worst case can be seen to become tighter. Moreover, the 10th percentile worst case for 2 image captures fails to identify any harmonics at all. Therefore, an oscillation cycle with at least 3 image captures will be required in order to capture a full elliptical motion. Interestingly, four image captures perform worse than three, which is due to the even number that can lead to more cases of low displacements measured.

Figure 3.9 shows results obtained using 3D analysis, and this is considered to be the ground truth data for accuracy assessment. Notably, it has higher peak values at both modal frequencies. Figure 3.10 shows the best cases of 1D and 2D analysis compared with this ground truth data, whereas Figure 3.11 shows the comparison with the worst cases. This fluctuation in performance is expected as the imaging may not commence at $phi = 0$. Although 1D best case is able to perform reasonably well with its best case, there is no guarantee that imaging will start at the desired phase delay. On the other hand, 2D analysis has the best overall performance.

A single-point LDV is also used to validate the 3kPa soft phantom's frequency response and the result is shown in Figure 3.12. The measurement is taken from 5Hz to 88Hz and has a resolution of 1Hz. As shown in Figure 2.7, due to the experimental setup, the LDV's sensitive beam is unable to be in parallel with the 1D Z-axis. Displacements are determined based on integrating surface accelerations.

All harmonics are able to be identified and are within 2Hz of error compared to the 1D Δy analysis. Some portion of these uncertainties may be caused by the interpolation process as it could only generate data entries that are close to the real ones. In addition, the responses from LDV have significantly smaller amplitudes compared to image based analysis, which once again proves the inadequacy of using acceleration data for calculating displacements because the main source of uncertainly originates from the integration process.

3.6 Alternative Metrics

Alternative metrics for assessing vibrational behavior have also been introduced during the studies, such as standard deviation, averaging and root-mean-square (RMS) of all the fiducial displacements. Absolute displacement such as Δxz remain the best choice due to its simplicity and capability of capturing harmonic frequencies on phantom breasts.

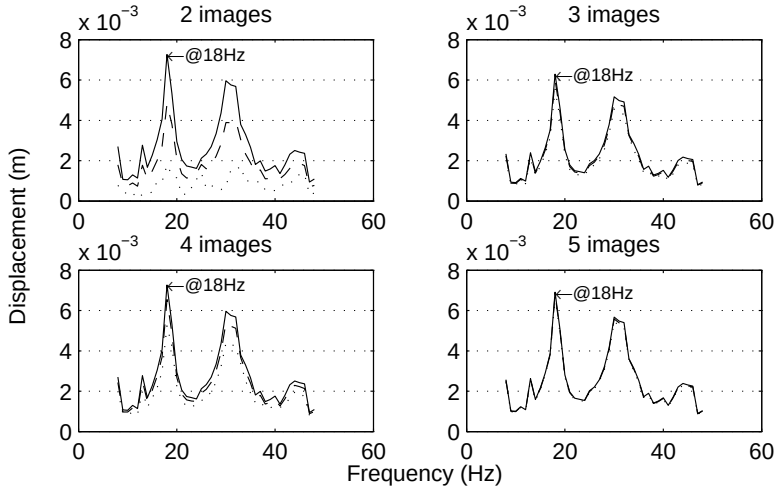

(a) 2D displacement analysis with $Max(\Delta x, \Delta y)$.

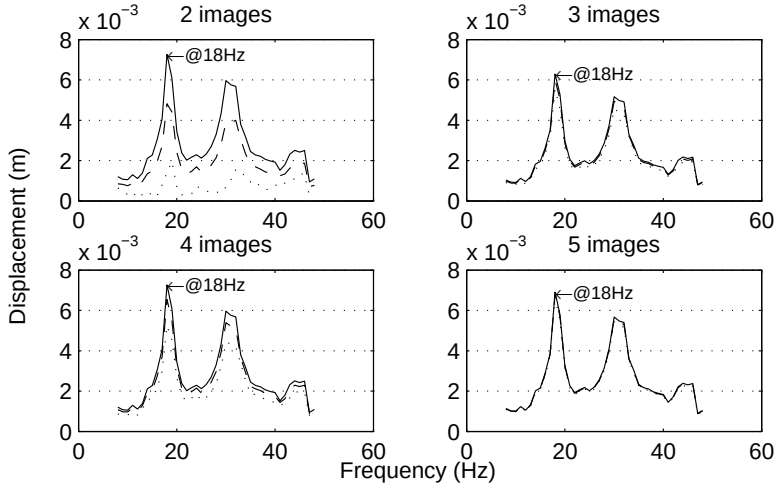

(b) 2D displacement analysis with $Max(\Delta x, \Delta z)$.

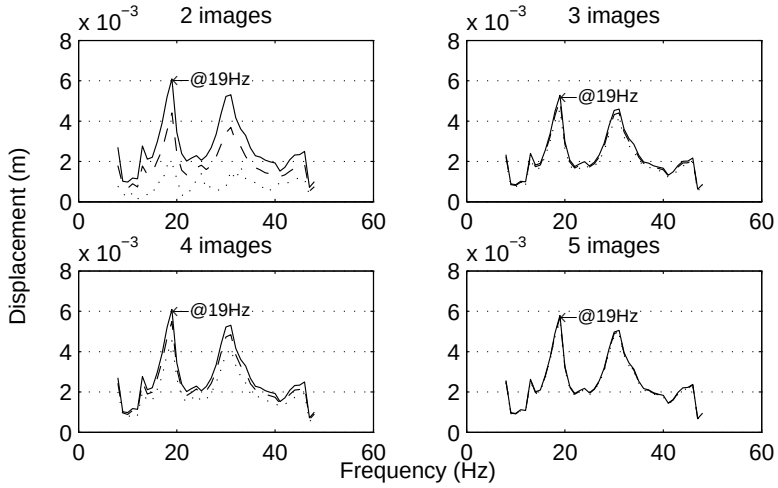

(c) 2D displacement analysis with $Max(\Delta y, \Delta z)$.

FIGURE 3.8: 2D analysis for 2,3,4,5 captures on a healthy 3kPa soft phantom, where Δx, Δy and Δz are displacements along X, Y and Z axes, respectively. 90th percentile (solid) represents the best case and 10th percentile (dotted) indicates the worst case.

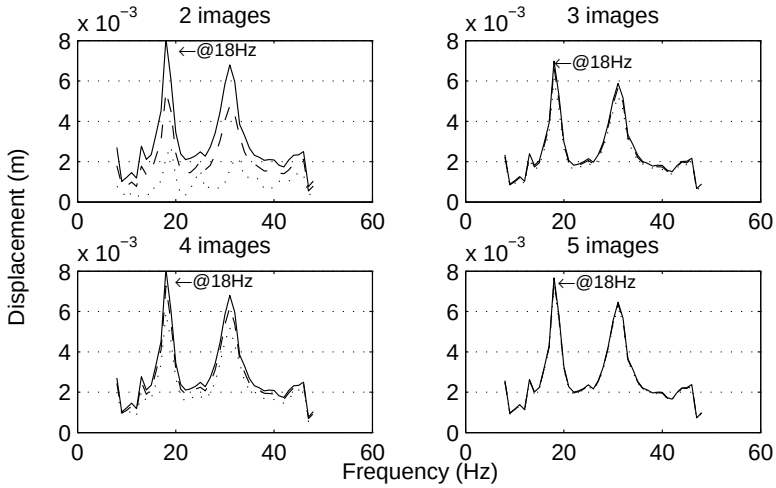

(a) 3D displacement analysis with $Max(\Delta x, \Delta y), \Delta z)$.

FIGURE 3.9: 3D analysis for 2,3,4,5 captures on a healthy 3kPa soft phantom, where Δx, Δy and Δz are displacements along X, Y and Z axes, respectively. 90 percentile (solid) represents the best case and 10 percentile (dotted) indicates the worst case.

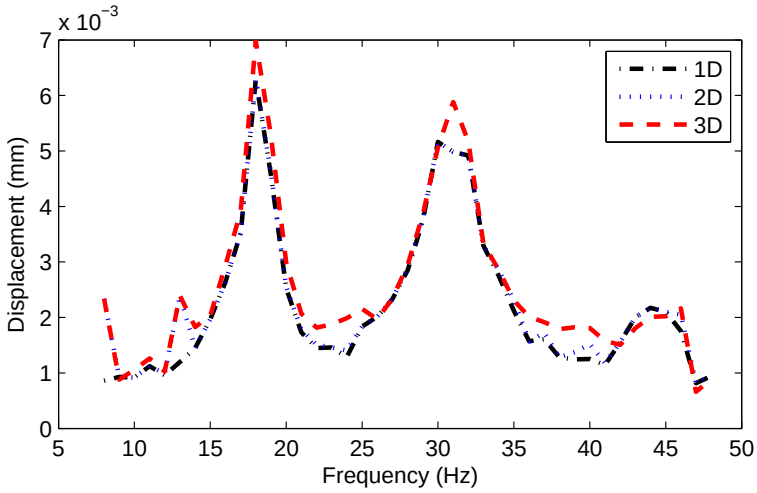

FIGURE 3.10: Comparison between 3D analysis ground truth data with best cases of 1D, and 2D analysis.

However, its exact performance on human breasts are yet to be confirmed as more trials are required to validate this.

Evaluation of standard deviation of all the fiducial displacements during one oscillation cycle can be potentially beneficial with a breast volume that has non-uniformly distributed density, because it measures the spread of the fiducial displacements in a given area. The feasibility analysis is carried out with the assumption that all healthy breasts should have homogeneous density distribution. In fact, the healthy silicon tissue found on all phantoms used in these studies is homogeneous.

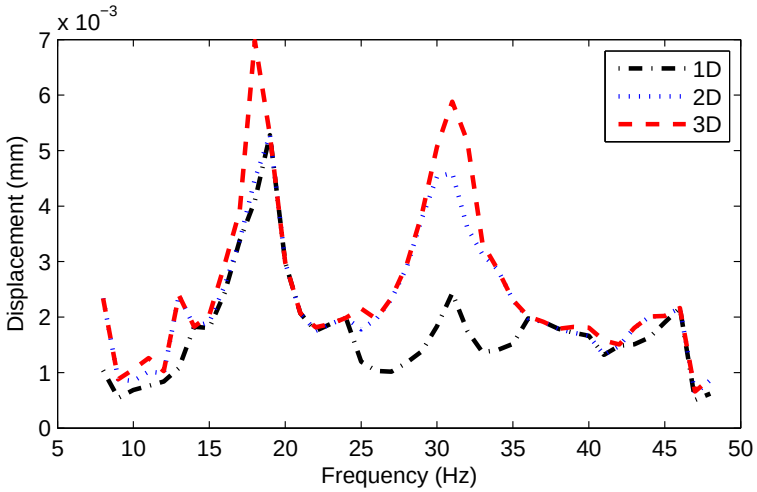

FIGURE 3.11: Comparison between 3D analysis ground truth data with worst cases of 1D, and 2D analysis.

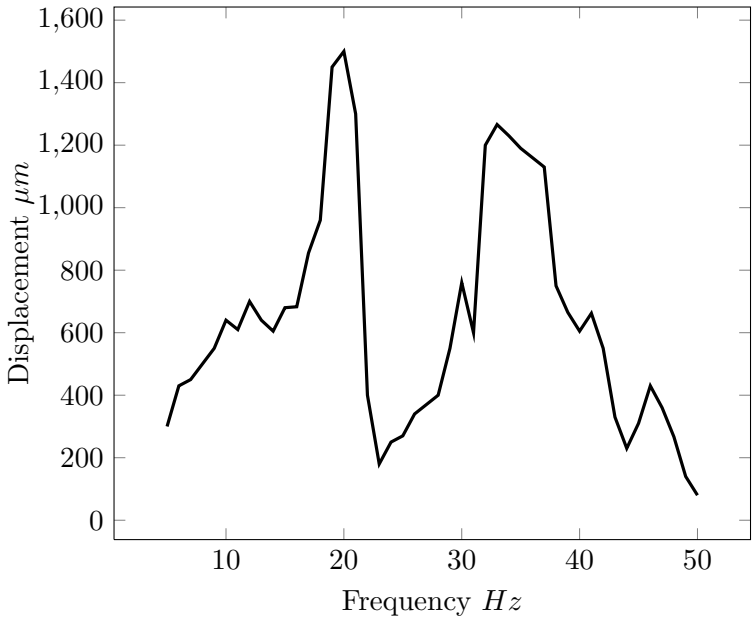

FIGURE 3.12: Single-point LDV validation of the frequency response from a healthy 3kPa soft phantom.

The metric for determining vibrational behavior will have to be revised if absolute displacement measurements Δ become inadequate.

3.7 Summary

Modal testing on the breast structure is required in order to determine its resonant frequencies. This aids the post processing software for successful identification and

location of cancerous tissues. The locations of fiducial markers during a single oscillation period are recorded and are used for subsequent displacement calculations.

Before carrying out any further studies on fiducial motion, more measurements of the fiducial positions in a single oscillation period must be acquired. However, this is relatively time-consuming. Therefore elliptical interpolation is used to generate additional data entries to simulate a variety number of image captures per oscillation cycle.

Retrospective feasibility studies based on a single image sensor have been carried out on a number of phantoms with different density and health status. Results suggest that absolute displacement measurements carried out in 2D with 3 image captures per oscillation cycle are sufficient to capture the frequency response of a breast volume, irrespective of the size and the shape of the breast. It is important to note that breast volumes with homogeneous density distributions are assumed. A single-point LDV is used to verify the frequency response of various phantoms using the setup illustrated in Figure 2.7. Validation once again proves 2D analysis is sufficient to identify all harmonic frequencies.

Chapter 4

Modal Analysis System

This chapter describes the structure and performance of the developed modal analysis system. Design considerations for each major component of the system are discussed in detail. It also describes communication protocols between components of the system. This is a key element in the system as it delivers the data that can be used for computing responses at various frequencies.

4.1 System Overview

The modal analysis system depicted in Figure 4.1 is implemented in such a manner that the frequency response of the breast can be obtained non-invasively and efficiently. In order to minimize resources and fully exploit the current imaging setup in the DIET system, the current modal testing system is designed to share imaging devices with the DIET system. Consequently, the imaging platform from the current DIET system is completely upgraded with newer cameras that increase the overall imaging speed. This setup allows five default imaging locations for carrying out the sweep. Additional imaging locations can be created by repositioning one of the cameras.

As shown in Figure 4.1, dSweep is the entry point for an imaging session. It carries out the imaging and data processing by coordinating communications between the three key components of the modal testing system, using physical wiring connections as well as TCP/IP communication sockets. A typical session is illustrated in Figure 4.2.

1) Appropriate initializations with user-specified capture settings on all hardware are performed. Once all initializations are completed and a list of frequencies is read from the configuration file, the program will try to establish communication channels with the camera, the actuator and the image tracking program. Once the system is up

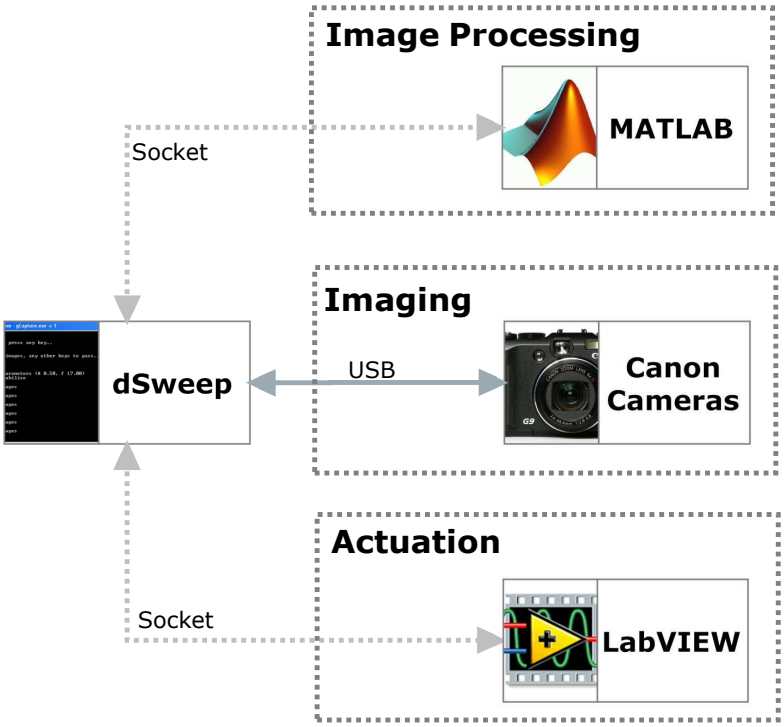

FIGURE 4.1: The system diagram of the modal testing system.

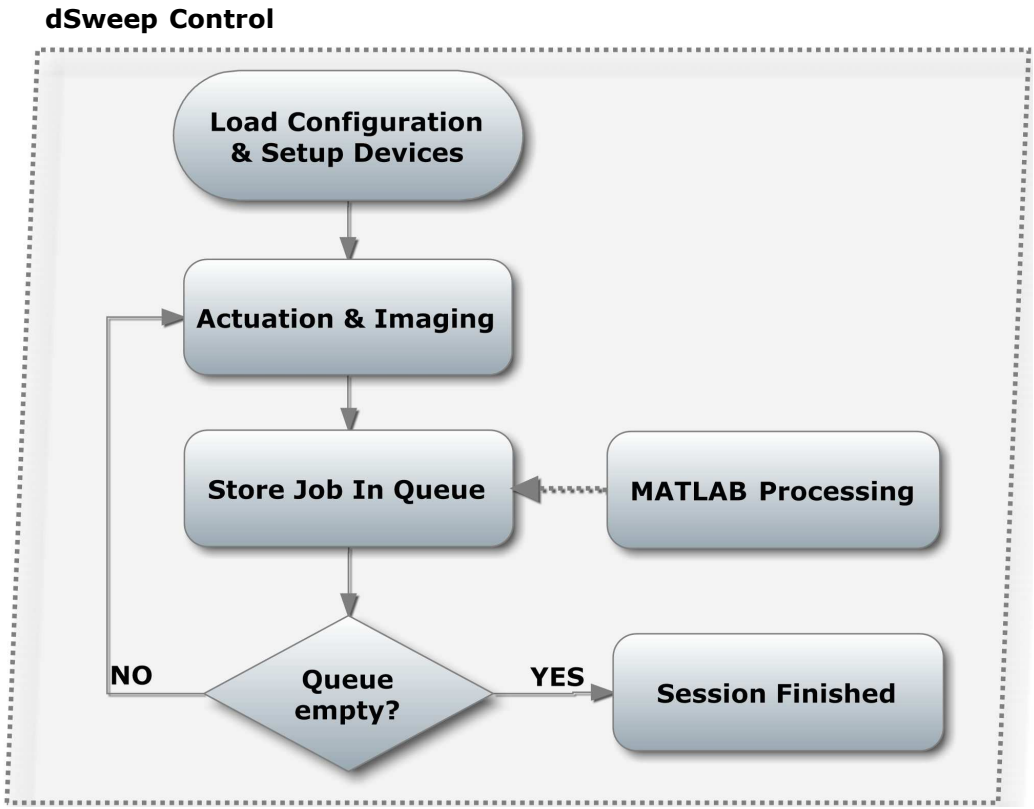

FIGURE 4.2: dSweep control during a typical imaging session. DSweep only takes care of imaging while tracking is carried out simultaneously by MATLAB

and running, dSweep will collect images at all frequencies found in the configuration file. This process is completely automated, as the program will step through the list sequentially.

2) Prior to commencing any imaging, dSweep instructs the actuator to operate at a particular frequency and amplitude. The program will then control the camera to capture a single oscillation cycle with a given number of captures. Once imaging at a particular frequency is completed and all the images are written to the local drive, the program will signal the dSweep server, that manages a queue of jobs that are ready to be tracked by the tracking application. Following this, the actuation and imaging step will move onto the next frequency and repeat this for all frequencies specified by the configuration file. The main purpose of the dSweep server is to facilitate the image tracking application with tracking new jobs as soon as they are imaged, simply by querying the dSweep server. Not only does this make full use of the computing resources, but also significantly increases the speed of the overall program. Once all the frequencies are captured, a special termination flag is raised.

3) Simultaneous to dSweep capturing, the image tracking program will constantly query the dSweep server running inside dSweep for new jobs to track. This is done via TCP/IP, so it is possible to use a separate computer on the network for processing those images. As shown in Figure 4.3, once a new job is detected, the image tracking program will store it into its own local queue for processing. This process repeats itself until there are no more jobs to process. Once the termination flag is received, it will generate a frequency response plot and let the server know it has finished.

4) Finally, dSweep server will terminate itself once tracking is finished. Following this, dSweep will then release all the hardware and all programs exit.

4.2 Main Application (dSweep)

This application is written entirely in C++ and is the entry point for an imaging session. It has two functionalities, namely to first carry out the imaging, and secondly to control the image tracking application via TCP/IP. The application exits when all frequencies are imaged and tracked.

4.2.1 Imaging

Most consumer cameras are capable of delivering images of sufficient quality. However, only a few brands allow its non-DSLR products to be controlled by third party software.

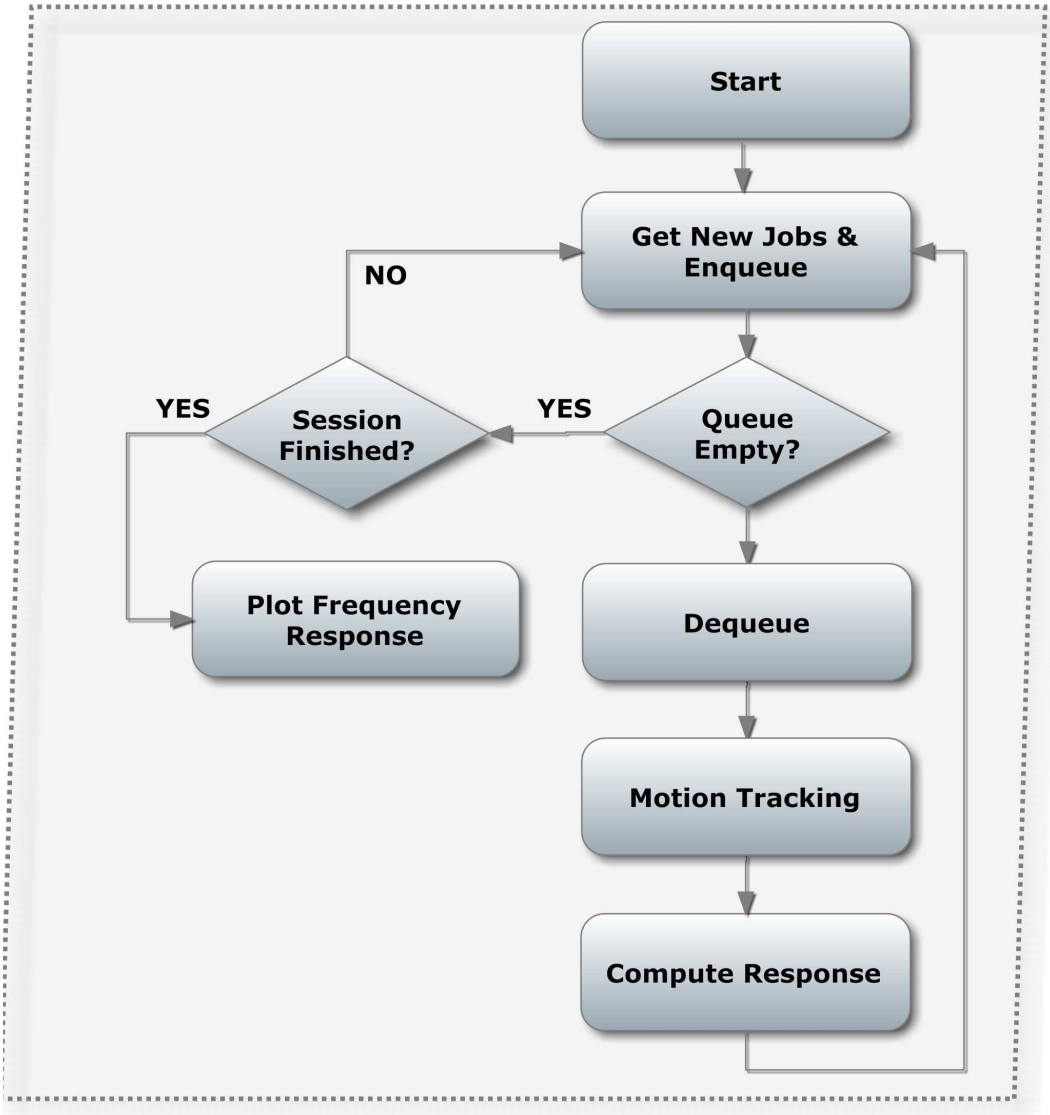

FIGURE 4.3: Matlab image processing.

Canon ™ maintained Software Development Kits (SDK) for some of its non-DSLR products, such as the G series. The aim of PowerShot G series of cameras is to give users some of the advanced features of its DSLR cameras while maintaining the cost and portability of its point-and-shoot models.

However, Canon has discontinued manufacturing G9 cameras and dropping SDK support for its newer non-DSLR products, replicability of the current imaging system is very much constrained. Moreover, there are difficulties associated with embedding these cameras into a portable commercial medical imaging unit. Therefore, alternative imaging devices will have to be introduced eventually, so the prototypes can be upgraded and replicated at ease. One obvious solution would be to employ DSLR cameras that are manufactured by both Nikon and Canon, which are extremely versatile and have relatively longer life cycles. However, these cameras are likely to be more expensive and

each model requires a different SDK. On the contrary, industrial cameras are becoming affordable, very compact and come with a universal SDK. Although these industrial cameras carry similar price tags compared to DSLR cameras, they are specifically designed to be embedded into other applications. This SDK is generally applicable to all cameras of a specific brand and the already written software can be recycled for upgraded camera systems

As aforementioned, in order to fully utilize the imaging setup in the DIET system, the modal testing system would have to share the imaging devices with the DIET system. This means a complete upgrade of the imaging system was required. A number of advantages were identified with using the PowerShot G9 cameras, and consequently they are chosen to replace the old G5 cameras in the DIET prototype.

- Superior processor, G9 employs DIGIC III for image processing while G5 uses DIGIC I. As a result, the imaging response time is significantly increased.
- Superior transferring speed, G9 uses USB 2 for data transfer while G5 uses USB 1. This was the main reason for the upgrade.
- A more sophisticated SDK, PowerShot RemoteCapture Software Development Kit (PRSDK^{TM}) is employed to control the G9. PRSDK uses fast and reliable Picture Transfer Protocol (PTP) while G5 can only be accessed with Canon Digital Camera SDK (CDSDK), which is outdated and less reliable.
- Controllability and versatility, PRSDK enables third party software to alter much more critical capture settings, such as Aperture, Shutter, ISO, Auto-focus mechanism, Auto-focus distance and Metering mode.

The G9 camera is attached to the PC via USB. A typical imaging session is illustrated in Figure 4.4. Default imaging settings, such as shown in Table 4.1, will be used if the user decides not to pass the program with a list of new parameters. With this list of special parameters, the program can apply system-wide changes in a way that is predictable and requires minimal effort. Refer to Appendix C for a full documentation on the list of parameters that the program supports.

Since all image captures are executed by threads, the main program will not lock up while the camera is taking a photo. This is beneficial as other routines can be carried out simultaneously and uninterruptedly. Using settings shown in Table 4.1, the performance of capturing and saving three images is recorded for a number of trials and results are shown in Table 4.2. Notably, compression to JPEG, transfer and write to hard disk altogether takes around $1 second$. Since each image itself requires $1 second$ exposure,

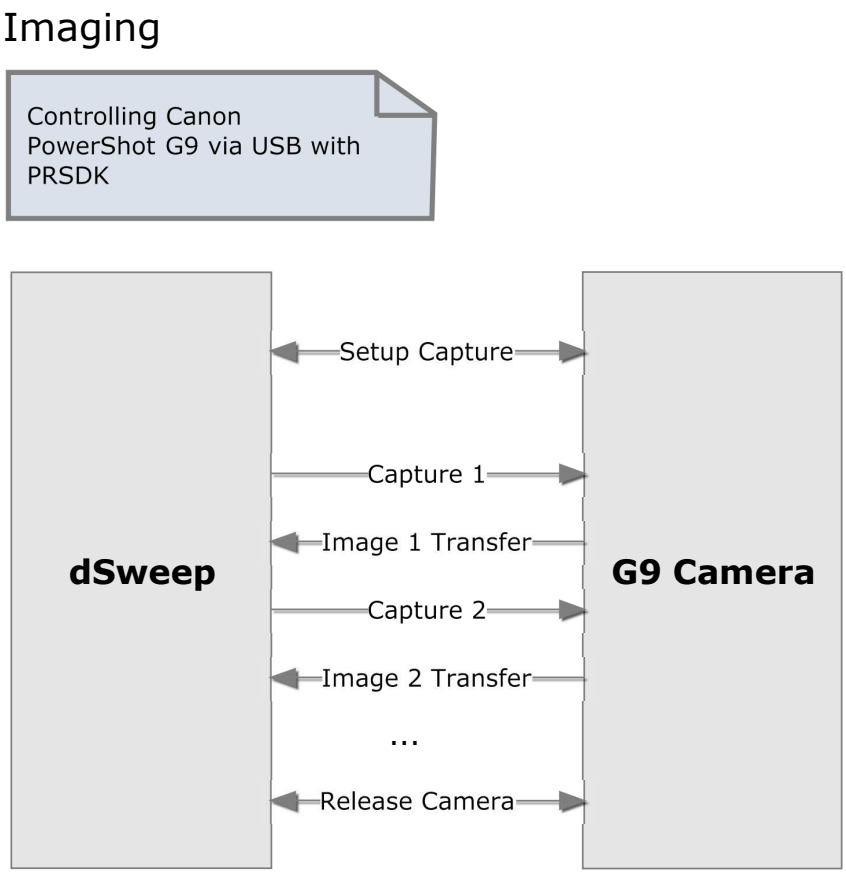

FIGURE 4.4: Communication channel between dSweep and the G9 camera during an imaging procedure.

imaging a set of three images would take less than 7*seconds* each to complete. This is far better compared to the performance from a G5 camera.

4.2.2 Tracking Control

dSweep server is embedded into the main program and runs on a separate thread. This particular server actively monitors a queue structure of untracked jobs. The imaging routine can add jobs to the queue while the tracking application can retrieve jobs from the queue. With the help from this server, image tracking is able to be performed in real time, parallel to imaging of the frequency sets.

4.3 Image Tracking Application

The image tracking application has the ability to work autonomously, and is also able to communicate and work efficiently with the dSweep server when required. The application

TABLE 4.1: Default imaging parameters.

Setting	Default value
Aperture	$f/8$
Shutter Speed	$1s$
ISO Sensitivity	100
Exposure Compensation	0
Exposure Mode	Manual
Auto-Focus Mode	Single Shot
Auto-Focus Distance	Close-up
Auto-Focus Assist	Disabled
Flash	Disabled
Metering	Evaluative
Image Quality	Fine
Image Size	1600x1200
Zoom	5
White Balance	Auto White Balance

TABLE 4.2: Time taken to capture and save three image captures. Each capture itself uses 1 second exposure. The test is repeated 8 times. Note that each set contains three images.

Set	1	2	3	4	5	6	7	8
Total (s)	6.00	6.62	6.30	6.57	6.23	6.87	6.96	6.99
JPEG + Tx + Write (s)	3.00	3.62	3.30	3.57	3.23	3.87	3.96	3.99
Per image (s)	1.00	1.21	1.10	1.19	1.08	1.29	1.32	1.33

is written in MATLAB^{TM} and the communication channel with dSweep is via sockets. A typical image processing session is shown in Figure 4.5, which consists of two main parts: first fiducial displacements are tracked at all the imaged frequencies, and second a frequency response is computed based on those displacements.

4.3.1 Tracking Fiducial Displacements

Feature tracking should take less time than image capturing so that both tasks can be carried out simultaneously and finish at approximately the same time. Therefore, a robust yet highly efficient feature tracking method is required for identifying fiducial motion on the images captured during a single oscillation period. Feature extraction based on thresholding and matching by nearest neighborhood is chosen for this application. A number of popular feature extraction methods are also presented.

4.3.1.1 Thresholding and Nearest Neighborhood

This is the method currently employed because of its reliability and accuracy. It is developed by Brown [31] and current implementation uses both C language as well as

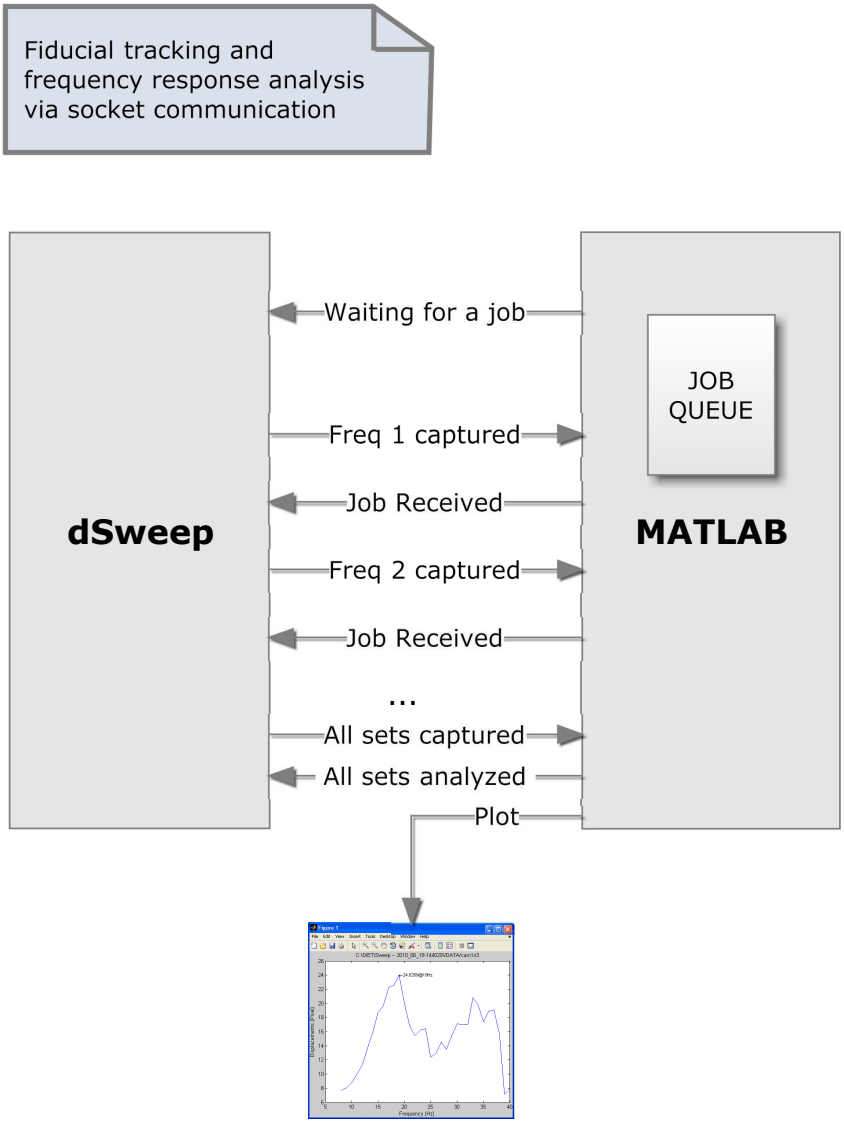

FIGURE 4.5: Communication channel between dSweep and MATLAB during an imaging procedure.

MATLAB™.

In this particular approach, positions of the fiducial markers are obtained by simple thresholding technique. Since there are only three colors of fiducial markers and all three colors are fairly well-defined, their approximate positions and color can be determined. Let $r(x, y)$, $g(x, y)$ and $b(x, y)$ be red, green and blue color values of a pixel (x, y) in 2D space. The resulting $\mathcal{R}$, $\mathcal{G}$ and blue $\mathcal{B}$ feature pixels sets are defined by Equation 4.1.

$$\begin{aligned}\mathcal{R} &= \{(x,y)|r(x,y) > 80, r(x,y) > 1.2 * g(x,y), r(x,y) > 1.2 * b(x,y)\} \\ \mathcal{G} &= \{(x,y)|g(x,y) > 80, g(x,y) > 1.2 * r(x,y), g(x,y) > 1.2 * b(x,y)\} \\ \mathcal{B} &= \{(x,y)|b(x,y) > 80, b(x,y) > 1.2 * r(x,y), b(x,y) > 1.2 * g(x,y)\}\end{aligned} \tag{4.1}$$

Following this, a continuous block of pixels that have the same color are recognized to be an individual fiducial marker and its position is approximated by computing the centroid of the block of pixels. Once feature extraction on all frames is finished, feature matching of all frames is achieved by comparing the euclidean distance of the closest neighbor to the second closest neighbor in the same color set. Location of the feature in the adjacent frames should be nearest neighbors.

It is important to note that prior to extracting features, a bounding box is calculated to isolate the breast from the background and minimize the number of pixels examined. Table 4.3 shows the performance of feature extraction and matching on three different sets of images, where each set contains three images describing the oscillation cycle. Notably, $\sim 3seconds$ is required to extract features from three images and no more than $2seconds$ to match those features. Consequently, tracking a set of three images should finish well within $5seconds$. Since most of the image tracking code is running in MATLAB^{TM}, the speed of execution is constrained.

TABLE 4.3: Performance of thresholding-based tracking and nearest neighborhood matching on three images. The quantity of feature points detected and time of execution are recorded. Note that each set contains three images. Individual performance is recorded on the number of feature points (pts) detected and the time taken in seconds (s).

	Image 1	Image 2	Image 3	Matched(s)	Total(s)
Set 1	554pts/0.95s	579pts/1.00s	591pts/1.05s	527/1.57s	4.57s
Set 2	573pts/0.98s	560pts/0.94s	601pts/1.03s	495/1.34s	4.29s
Set 3	564pts/1.00s	539pts/0.93s	527pts/0.90s	511/1.49s	4.32s

4.3.1.2 SIFT and SURF

Scale-invariant feature transform (SIFT) described by Lowe *et al.* [56, 57] is a feature identification algorithm designed for extracting and recognizing salient regions or feature points in images. SIFT detector uses the difference of successive Gaussian-blurred images to identify potential points of interest. This is achieved by removing low contrast points and rejecting edge responses. An orientation histogram based on local image gradient directions is formed to achieve invariance in scale, rotation and location.

Speeded Up Robust Features (SURF) proposed by Bay *et al.* [58] is another scale and rotation-invariant interest point detector and it employs a slightly different way to detect features [59]. It is based on the sums of approximated 2D Haar wavelet responses and uses integral images to compute responses of rectangular box filters in an efficient manner.

The studies performed by Bauer *et al.* [60] and Juan *et al.* [61] indicate SURF outperforms SIFT during the feature point identification process due to its superior processing speed and higher accuracy. However, SURF detects slightly less feature points than SIFT.

SIFT and SURF both have their own advantages; SURF is known for its speed of processing while SIFT is good at detecting rotating objects. Several implementations of both algorithms exist in the open-source community. OpenSURF (written in C++) is tested with existing phantom images. Figure 4.6 depicts a tracked frame from a series of images that describes a single oscillation cycle. Notably, the tracking speed is faster than the thresholding method, partially because it detects less points. For example, experimental results shown in Table 4.4 suggest that $\sim 2seconds$ are required to extract features on three images compared to the $\sim 3seconds$ required by thresholding. In addition, there have been several implementations that are specifically designed to increase the performance. Those designs use Graphics Processing Unit (GPU) to carry out calculations and the speed is even faster [62, 63]. In both algorithms, feature matching can be achieved by nearest neighborhood method.

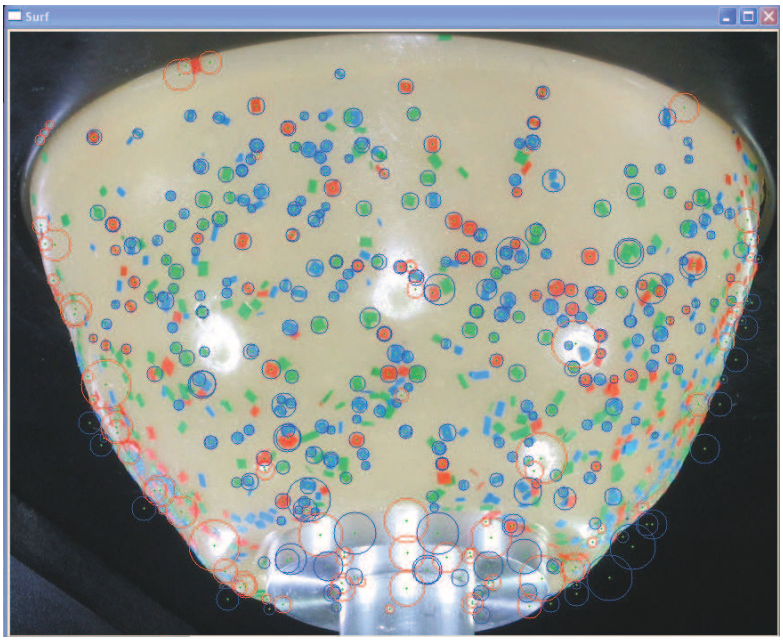

FIGURE 4.6: OpenSURF tracking features in a single image, 434 interest points are detected in 0.61 seconds. Note that unwanted features can be filtered in order to enhance the accuracy.

TABLE 4.4: Performance of feature extraction using OpenSURF on sets of three images. The quantity of feature points detected and the program execution time are recorded for each image. Individual performance is recorded on the number of feature points (pts) detected and the time taken in seconds (s).

	Image 1	Image 2	Image 3
Set 1	434pts/0.61s	512pts/0.82s	414pts/0.54s
Set 2	462pts/0.77s	497pts/0.80s	459pts/0.67s
Set 3	471pts/0.72s	450pts/0.69s	421pts/0.59s

The main advantage of using SIFT/SURF is that many well-maintained implementations are available in the open-source community. Furthermore, no additional software package is required to analyze fiducial movements. It is thus possible to incorporate the motion tracking algorithm into the imaging program, creating a standalone control application.

4.3.1.3 FastNCC

The Fast Normalized Cross Correlation (FastNCC) described by Hii *et al.* is an accurate method for motion tracking [64]. For a given window of pixels, Fast NCC will search for the most similar landmark in the upcoming frame through template matching. Landmarks such as fiducial markers are approximated with rectangular functions, so the speed of matching in dramatically enhanced. Its performance is much improved compared to traditional FFT Normalized Cross Correlation algorithm, but still slower than desired. Current computationally expensive implementation requires MATLAB runtime and is unable to track all images within a sensible time frame. This algorithm can become quite accurate when smaller sized windows are used, but this may have some detrimental effects on the overall processing time. Faster processing time may be achieved if the algorithm is reimplemented in low level languages.

4.3.1.4 Skin Tracking

Results from preliminary research show that a sequence of ordered images allow the estimation of motion of the skin as either instantaneous image velocities or discrete image displacements [65]. Optical flow, or apparent motion between two images can be estimated by a differential method such Equation 4.2, assuming movement is small.

$$\frac{\partial I}{\partial x}\delta x + \frac{\partial I}{\partial y}\delta y + \frac{\partial I}{\partial t}\delta t = 0 \tag{4.2}$$

$I(x, y, t)$ defines the intensity of a pixel at location (x, y, t). u and v represents image velocities in the directions of x and y respectively. Unfortunately, optical flow can not be directly estimated due to the presence of two unknowns in one equation. Additional constraints must be introduced in order to solve for motions. Adding epipolar constraints such that requires two corresponding points to be epipolar compatible in a single frame and multiple frames would solve the equation. The biggest advantage of using this method is that no fiducial markers are require. More research into this is required.

4.3.2 Frequency Response Reconstruction

A number of reconstruction methods have been introduced in the previous chapter, which are all based on absolute displacements of the fiducial markers. Image tracking software described in this chapter computes frequency responses using Δxz 2D analysis. All displacements are calculated in pixels and the harmonic with largest displacement is highlighted. An example response is shown in Figure 4.7, where a sweep between 10Hz to 40Hz is studied using default capturing parameters. Two harmonics are detected; the natural frequency at 18Hz and a second harmonic at 30Hz.

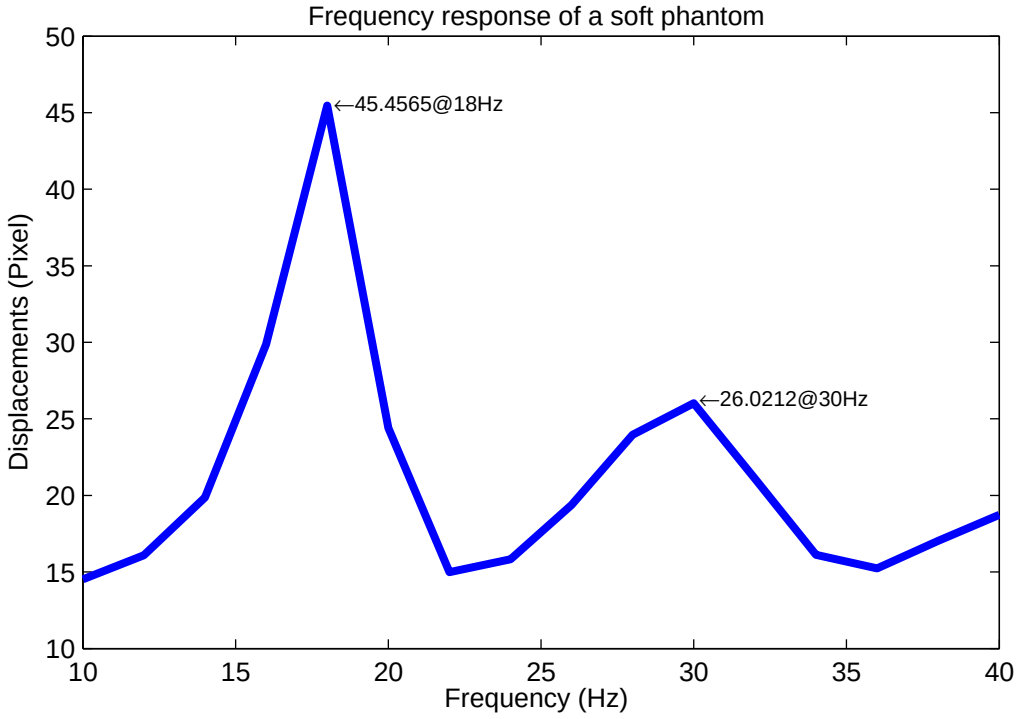

FIGURE 4.7: Frequency response is reconstructed from a sweep of 16 different frequencies that are spaced equally apart between 8Hz to 40Hz. The sweep is performed on a soft 3kPa phantom with three image captures per oscillation, and uses default imaging parameters. Evidently, the first two harmonics can be identified well

4.4 Communication Protocol Between Applications

A dSweep server is running on a dedicated non-blocking thread, as part of the dSweep program. Capturing and tracking are able to reach such server on port 6789. It is important to note that direct communications between capturing and tracking is prohibited. A simple protocol is developed to synchronize all components of the system. See Appendix D for a summary on all available packet structures. These packets can be classified into three categories, depending on their origins.

4.4.1 Imaging

Once a particular frequency is imaged, the file path of the folder containing those images is transmitted to dSweep server using the following packet.

```
DSWEEP&=PATH_TO_JOB
```

Imaging routine is only able to "enqueue" new jobs and will not be allowed to modify the content of the job queue.

4.4.2 Tracking

Tracking on the other hand, has full rights to modify and retrieve contents of the job queue located on the server. A simple job query can be carried out by the following packet.

```
DTRACK&=
```

Job queries are made on a consistent basis, the server replies with either job entries or operation flags. Once all jobs are tracked and frequency response is generated, the termination flag is passed back to the server.

```
DTRACK&=JOBRXD
```

4.4.3 dSweep Server

The server looks after both imaging and tracking and runs on its own thread. This thread is embedded into the capture application and it manages a job list of unfinished jobs. Its main job is to acknowledge any query packets that are sent from the two clients.

```
ACKDSWEEP&=
```

The server acknowledges any new jobs that have been submitted by the imaging routine with the above packet. On the other hand, three different types of acknowledgment packets can be issued to the tracking application.

```
ACKDTRACK&=PATH_TO_JOB
ACKDTRACK&=QEMPTY
ACKDTRACK&=JOBFIN
```

The first acknowledgment packet is transmitted whenever there is a job available on the queue for tracking. When there are jobs ready to be processed, queue empty flag is issued with the second acknowledgment packet. Termination flag is issued whenever imaging is completed on all frequencies.

4.5 Performance Analysis

If imaging and tracking take approximately the same time to complete, interleaving these two tasks would maximize the performance, saving as much as half of the time originally required. As mentioned earlier, imaging and tracking of three images would take no more than $7 seconds$ each. Execution time of dSweep for the current setup with three image captures per oscillation using one camera is shown in Table 4.5. Standard sweeps of 33 frequencies, from 8Hz to 40Hz with a resolution of 1Hz are carried out. On average, each set of three images take about $10 seconds$ to complete. However, due to additional time overheads, those numbers do not truly reflect the actual time that is spent on imaging and tracking. Overheads include

- Time taken to initialize the imaging device ($\sim 5 seconds$)
- Since the current actuation system requires some time to stabilize its motion, an extra $2 seconds$ delay is added into the imaging routine. Therefore it must be taken out from the $10 seconds$ total time spent
- The image tracking software checks jobs from the server once every $5 seconds$, so there may be a slight delay
- Since tracking of the last set can only start when all n sets are imaged, time taken for imaging and tracking should be approximately $(n + 1) * t$.

TABLE 4.5: Overall performance of the current setup.

Session name	Number of sets	Images per set	Total images created	Total time (s)	Avg. time per set (s)
MK3 10mm	33	3	99	330	10.00
MK3 20mm	33	3	99	332	10.06
MK3 Clean	33	3	99	350	10.61
Stiff 10mm	33	3	99	320	9.70
Stiff 22mm	33	3	99	330	10.00
Stiff Clean	33	3	99	310	9.39

Sometimes, it is possible for the tracking program to detect a number of new jobs on the dSweep server, which generally creates a backlog that could have a detrimental impact on the performance of the overall system. This is because the frequency response can only be reconstructed if responses at all frequencies are calculated. An increase in size of the backlog indicates that tracking takes longer than imaging. Theoretically, the efficiency of the overall system reaches its highest when there is zero backlog. Consequently, it would be a good idea to run the tracking application on a faster computer somewhere else on the network if there the backlog starts to build up.

4.6 Summary

The setup of the developed modal analysis platform has been presented in this chapter. The system setup uses Canon G9 for imaging, thresholding to extract the positions of fiducial markers and nearest neighborhood for matching those features. Performance-wise, the time it takes to image three captures is approximately the same as tracking (less than 7 seconds), so it is possible to maximize the overall performance by running the two processes concurrently. As seen in test-runs, 10 seconds is sufficient for completing imaging and tracking for a three image capture set. As a result, the system is able to produce a full frequency response consisting of results at 33 different frequencies within 6 minutes. Alternative imaging and image processing solutions are presented, so clearly improvements can be made to the existing system. Appendix C describe a full documentation and user guide of the programs described in this chapter.

Chapter 5

Experimental Results

Using the experimental setup described in the previous chapter, studies have been carried out on silicone phantoms and some results are obtained from human breasts. This chapter presents those frequency responses and attempts to examine the implications the tumor properties and system settings may have with its frequency responses. More specifically, the impact on modal frequencies due to different imaging locations, dimension of tumor, tumor location and phantom stiffness are presented.

5.1 Phantoms Trials

All silicone phantoms used in this study are homogeneous, apart from their inclusions. As shown in Figure 5.1, the precise location of an inclusion can be described by its horizontal distance h and vertical distance v from the center.

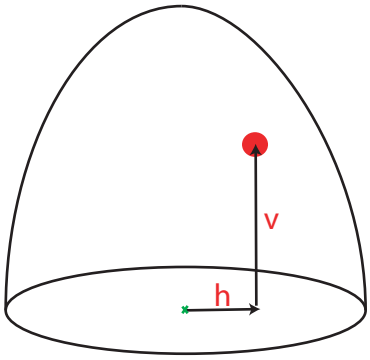

FIGURE 5.1: Graphical representation of the tumor position, where h is the horizontal distance and v is the vertical distance measured from the center.

Unless otherwise stated, an experiment is conducted with default capturing parameters: three image captures per oscillation with a single camera and default camera settings shown in Table 4.1.

5.1.1 Imaging locations

Results are obtained from six different imaging locations: the 5 default imaging locations shown in Figure 1.2 and an additional location shown in Figure 5.2. The additional camera position is created by clamping the camera onto the side-rail. This position is parallel to the top surface.

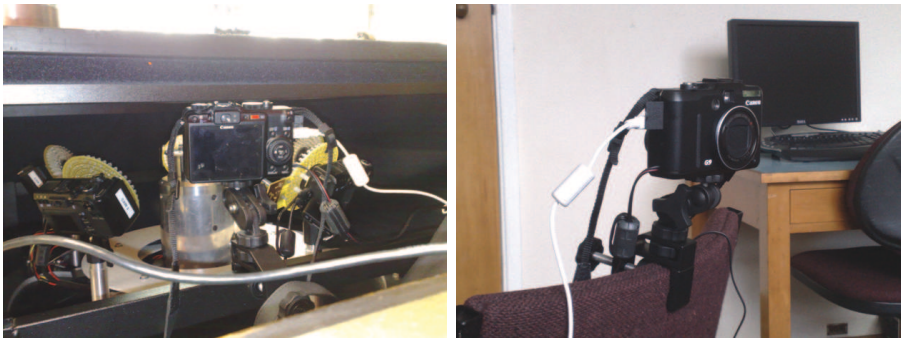

(a) Additional imaging location (b) The clamp

FIGURE 5.2: Additional imaging location created by clamping the camera onto the side-rail.

As shown in Figure 5.3, camera location has very little impact on the frequency responses of all phantoms. Although the magnitude of response varies depending on the imaging locations, frequencies of the harmonics remain unaffected. It is somewhat interesting to note that Camera 6, which is positioned on the side-rail, has much weaker responses compared to the other cameras. A possible explanation for this might be that this camera uses a different zoom setting since it is positioned further than the others. Consequently, the motion may appear differently at this available zoom setting than the others. Another possible explanation for this is that Camera 6 has a completely different view of fiducial movement compared to the others, so a smaller motion is detected. Despite of this downscaling behavior, the fundamental frequency still appears to be very distinctive and consistent with predictions from the rest of the cameras.

5.1.2 Phantom Stiffness

The results shown in Figure 5.4 suggest that stiffer phantoms have higher resonances. This finding is in agreement with the simulation results shown in Chapter 3. On the question of surface displacement measured, responses from the stiffer phantom are significantly smaller compared to surface displacements on the soft phantom. This weakened behavior is much expected since the stiff material that the phantom is molded from requires a much stronger actuation force to cause any deformation.

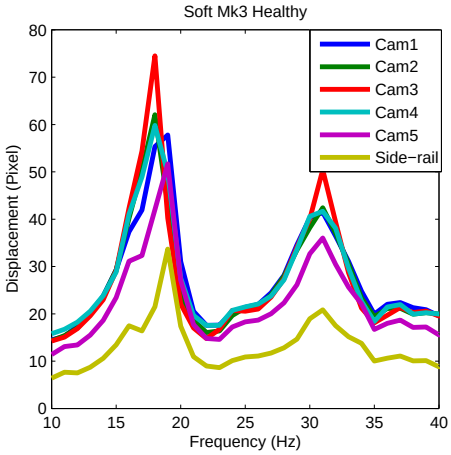

(a) Healthy

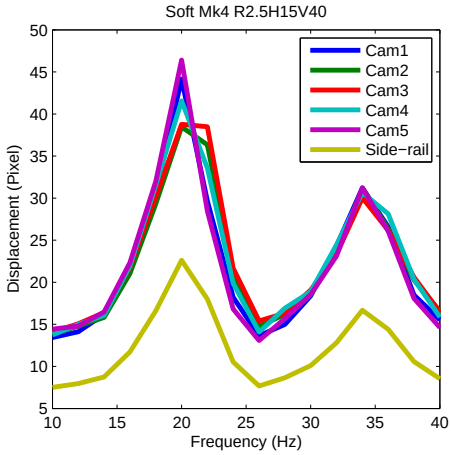

(b) 2.5mm inclusion at $h = 15mm$,$v = 40mm$

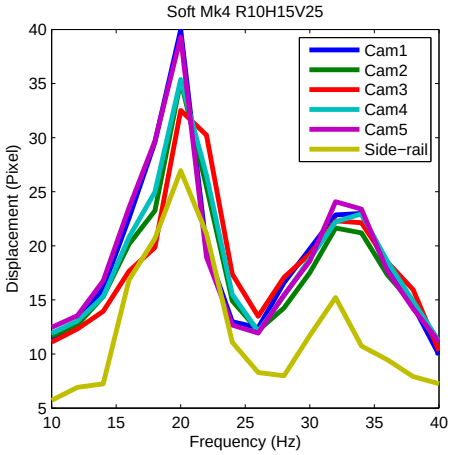

(c) 5mm inclusion at $h = 12mm$,$v = 40mm$

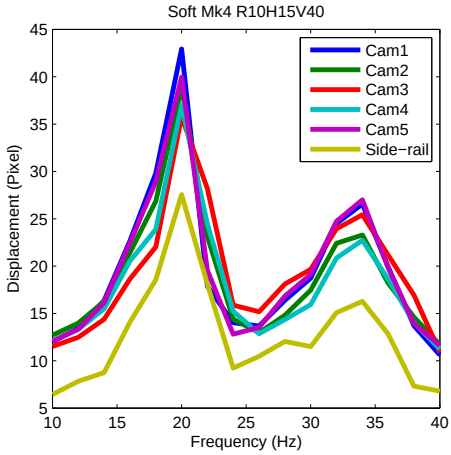

(d) 10mm inclusion at $h = 15mm$,$v = 40mm$

FIGURE 5.3: Frequency responses of 4 different phantoms imaged at 6 locations.

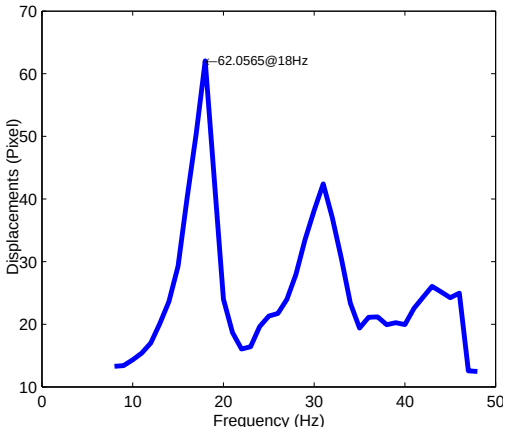

(a) Healthy soft 3kPa phantom

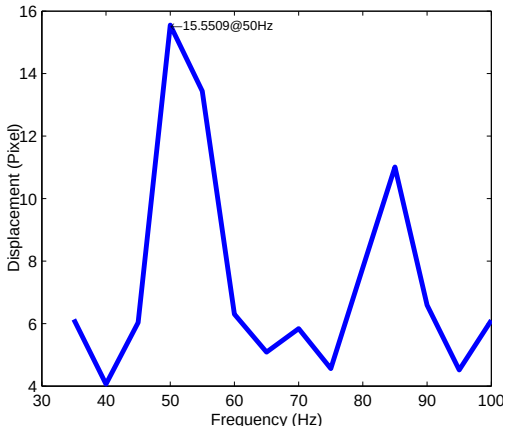

(b) Healthy stiff 30kPa phantom

FIGURE 5.4: Effect of phantom stiffness on modal frequencies.

5.1.3 Dimension and Location of Inclusion

Three different dimensions of inclusions are tested using the soft phantom and their responses are shown previously in Figure 5.3. Modal frequencies detected from those responses are tabulated in Table 5.1. Notably, the observed difference between locations of fundamental frequencies is not significant. However, the displacement amplitudes suggest that a link may exist between the size of the inclusion and the damping coefficient of the breast volume.

TABLE 5.1: Modal frequencies for a soft 3kPa phantom with inclusion.

Radius (mm)	Location (mm)	Fundamental (Hz)	Second Harmonic (Hz)
2.5	$h = 15, v = 40$	18	34
5	$h = 15, v = 25$	20	34
5	$h = 15, v = 40$	20	34
5	$h = 25, v = 40$	20	34
5	$h = 35, v = 25$	20	32
10	$h = 15, v = 25$	20	30
10	$h = 15, v = 40$	20	34
10	$h = 25, v = 40$	20	32
10	$h = 35, v = 25$	20	32

Table 5.1 did not show any significant changes in modal frequencies with different locations of inclusions. Figure 5.5 illustrates responses for two different sizes of inclusions: $5mm$ and $10mm$. It has been observed that inclusions with larger horizontal distances to the center weaken the overall responses; that is, motions appear to be constrained by inclusions that are placed further away from the actuation axis and closer to the surface.

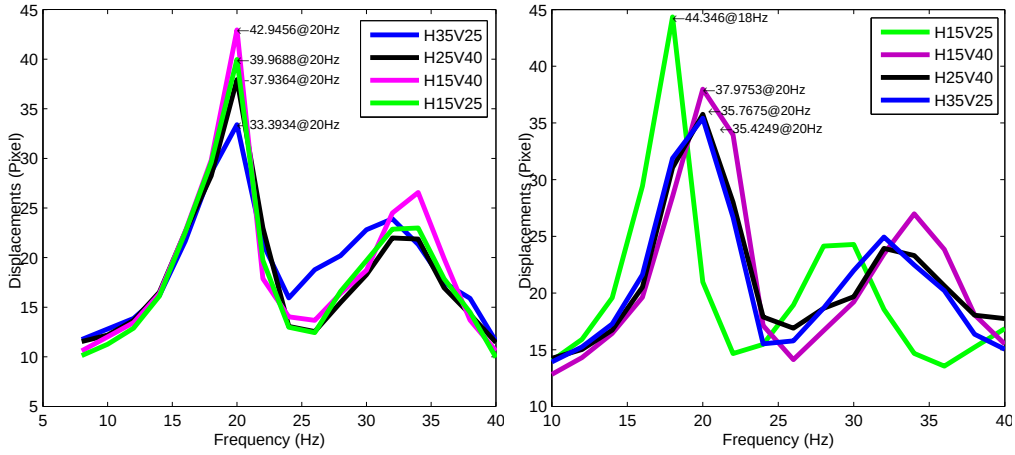

(a) $10mm$ inclusion (b) $5mm$ inclusion

FIGURE 5.5: Responses with different tumor positions, where HxVy indicates the exact location of the inclusion in mm.

5.2 Human Trials

As shown in Figure 5.6, preliminary results from trials carried out on several healthy human breasts indicate that typical human breasts share similar fundamental frequencies compared to the 3kPa soft phantom, between $15Hz$ and $20Hz$. Moreover, the imaging location does have some slight impact on the magnitudes of responses obtained. This finding is in agreement with the finding in phantom studies.

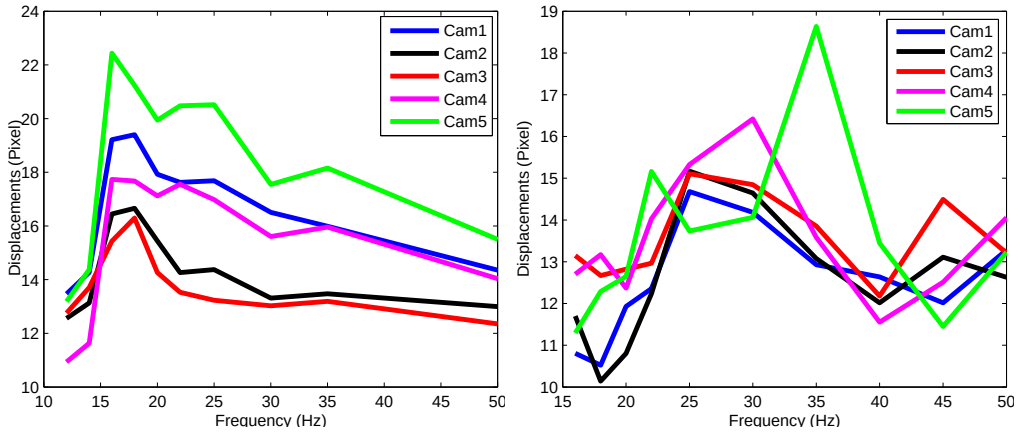

(a) HS009 (b) JC008

(c) JW007 (d) OR006

FIGURE 5.6: Frequency responses from several healthy human breasts.

In contrast to earlier findings in phantom studies, responses from Camera 4 and 5 shown in Figure 5.6(b) show completely different modal frequencies compared to all other cameras. A possible explanation for this might be that the breast was moving during the imaging procedure. It is probable therefore that human-induced breast movement during the imaging has strong influences on the quality of results. Another possible explanation for this is that human breasts are not homogeneous and hence density of the tissue is likely to be variable at different locations. Consequently, the resonant frequencies are expected to be affected by different imaging locations.

One unanticipated finding is that all healthy cases shown in Figure 5.6 do not seem to have distinctive second harmonics. This finding has important implications for developing phantoms in the future. However, more human trials will have to be conducted in the future in order to validate such behavior. This finding is in agreement with previous findings documented by Peters [32] which showed that typical healthy breast volumes have similar stiffness.

5.3 Summary

The results shown in this chapter provide an insight into the performance of the modal analysis platform on both silicone phantoms and human breasts. The potential impact of phantom properties and imaging settings on responses are investigated.

Silicone phantoms of two types of stiffnesses were tested: 3 kPa and 33 kPa. As expected, an increase in tissue stiffness results in much higher resonances. As seen in phantom studies, resonant frequencies are not so much affected by the imaging location, dimension or location of its inclusion. However, these parameters have influences on the magnitude of responses. The fundamental frequency for the silicone phantoms were centered around $20Hz$.

In human trials, several healthy breasts were examined. This finding, while preliminary, suggests that different imaging location can sometimes lead to different responses because human breasts are not homogeneous. Further testing on unhealthy breasts should be undertaken to reveal the modal analysis platform's true performance. The fundamental frequency for the healthy human breasts tested were between $15Hz$ to $25Hz$.

It is apparent that the soft silicone phantoms are well-suited for modeling the breast tissues given their frequency responses are relatively similar. A sweep between $8Hz$ and $40Hz$ is sufficient for detecting the fundamental frequencies in all cases.

Chapter 6

Conclusions and Future Work

6.1 Conclusions

This project was undertaken to design a cost effective, yet accurate modal analysis platform for the Digital Image-based Elasto-Tomography (DIET) breast cancer screening system, so natural frequencies of the breast can be obtained prior to imaging.

The requirements for the system were low cost and non-invasive sensing. Various sensing methods were evaluated and an image-based motion tracking approach was chosen for this application

The designed 2D sensing method was evaluated on retrospective motion data to determine optimal settings and limitations. Before implementation in hardware and software with default parameters, the designed system is able to produce a full frequency response in a short time frame. A full response that consists of 33 different frequencies can be reconstructed within 6 minutes. This is possible because image processing and capturing are carried out simultaneously in an automated fashion.

Validation of the developed system was undertaken on silicone phantoms and human breasts to assess the impact of camera numbers and positioning.

The phantom studies have found that imaging location had very little impact on the resonant frequencies, mainly because the silicone phantoms have equal density for all healthy tissue. However, results from human trials suggest the opposite, due to the fact that human breast tissues are likely to be inhomogeneous.

These phantom studies also showed that generally the dimension and location of inclusion will not affect the location of harmonics. But the behavior of responses from human breast with presence of inclusions are yet to be determined. The main limitation

of this study is that the number of human trials was relatively small, and future human trials are required so a relationship can be established between the phantom studies and human trials.

Overall, the modal analysis system developed in this thesis proved to be functional in assessing modal behavior of soft tissue. The system was designed on prior imaging data, implemented in hardware and software and validated on silicone and human breasts. The imaging performance improvements introduced by this system will help contribute to an improved overall DIET system.

6.2 Future Work

The hardware choice of G9 PowerShot cameras has proven to work well as it is able to deliver satisfactory images in a timely manner. However, Canon^{TM} is phasing out PRSDK supports for its non-DSLR products and alternative imaging solutions are required for building future prototypes. Industrial cameras in particular are attractive due to their compact size and light weight, and programming support. More generally, research is also needed to determine the best way for sensing vibrations non-invasively.

The image tracking application has proven to be fast enough to allow the processing to run in real time. However, the current implementation is fully written in MATLAB, and the processing speed is severely constrained by the MATLAB runtime environment. The speed can be dramatically increased if the software could be rewritten in lower level languages. While simply thresholding and nearest neighbor matching appears to be sufficient to track fiducial displacements, it may be worthwhile to evaluate alternative image tracking techniques such as optical flow and feature descriptor tracking because these methods can reveal more interesting characteristics of the fiducial movement. Considerably more work will need to be done to determine the most robust tracking solution.

Absolute displacements in 2D is the metric currently employed for computing responses at different frequencies. The algorithm can be easily adapted to use other metrics, such as standard deviation and RMS of displacements. Future work should look at how the performance varies with different metrics.

Preliminary results from human trials suggest that human breasts share similar frequency responses with the 3kPa soft silicone phantom; hence, extensive phantom studies using the soft silicon material were conducted. It has been revealed that the fundamental frequencies of those phantoms are centered around $20Hz$, whereas the human breast is seen to have its fundamental frequency somewhere between $15Hz$ to $25Hz$. A typical sweep from $8Hz$ to $40Hz$ is sufficient to reveal both harmonics of the silicone phantom.

In human trials, the second harmonic is either negligibly small or not picked up. Further experiments are essential, so more realistic phantoms can be constructed.

Appendix A

Least Common Multiple

A.1 Data Interpolation

It is ideal to conduct a separate experiment with the required image per cycle settings. However, this is relatively time-consuming as there is a large number of phantoms and different images per cycle settings that needs to be evaluated.

One way of shortening this cumbersome process would be: image a particular phantom with N images per cycle, where N is the least common multiple (LCM) of all the images per cycle that one wants to study; for example $(n_1, n_2, ..., n_k)$. These number of images per cycle $(n_1, n_2, ..., n_k)$ can then be precisely obtained from this N images per cycle measurement through decimation. This eliminates the need to perform $(n_1, n_2, ..., n_k)$ images per cycle on the same phantom numerous times. However, the major drawback of this method is that a large amount of images are required to be captured to study a large group of images per cycles. The LCM of a series $(n_1, n_2, ..., n_k) = (2, 3, 4, 5, 6, 7, 8)$ is calculated to be 840; that is, 840 images per oscillation cycle. This will be the amount of data generated at one particular actuation frequency. It will need to be multiplied by the number of actuation frequencies one wants to investigate to get an idea of the data storage required. This becomes highly impractical and even more computational expensive to process. Therefore, other solutions for generating additional measurements are sought after.

A.2 Finding LCM by prime factorization

The LCM of any two numbers a and b, denoted by $lcm(a, b)$ can be calculated using the smallest positive number m for which there exist positive integers n_a and n_b, such that

$$m = an_a = bn_b \tag{A.1}$$

The LCM for more than two numbers is similarly defined.

$$m = a_1 n_{a_1} = a_2 n_{a_2} = a_3 n_{a_3} = a_4 n_{a_4} = a_5 n_{a_5} = ... = a_k n_{a_k} \tag{A.2}$$

The LCM of any two numbers a and b can be obtained by their prime factorizations, such that

$$a = p_1^{a_1} ... p_k^{a_k} \tag{A.3}$$

$$b = p_1^{b_1} ... p_k^{b_k} \tag{A.4}$$

where the p elements represents all the prime factors of a, b. If a particular p does not occur in one factorization, the corresponding exponent is assigned to 0. The LCM is then given by the following equation.

$$lcm(a, b) = \prod_{k=1}^{n} p_k^{max(a_k b_k)} \tag{A.5}$$

For example, LCM(3,4,5,6) would result in the following:

$$\begin{aligned} 3 &= 2^0 3^1 5^0 \\ 4 &= 2^2 3^0 5^0 \\ 5 &= 2^0 3^0 5^1 \\ 6 &= 2^2 3^1 5^0 \end{aligned} \tag{A.6}$$

$\therefore lcm(3, 4, 5, 6) = 2^2 3^1 5^1 = 60$

A.3 Finding LCM by Greatest Common Divisor

LCM of two numbers can also be defined by Equation A.7, where GCD is the great common divisor of the two.

$$lcm(a,b) = \frac{ab}{GCD(a,b)} \tag{A.7}$$

Since LCM is associative, LCM of more than two numbers can be computed by Equation A.8.

$$lcm(a_1, a_2, a_3, ..., a_k) = lcm(a_1, lcm(a_2, lcm(a_3, lcm(..., lcm(a_{k-1}, a_k))))) \tag{A.8}$$

Appendix B

Retrospective Feasibility Studies On Various Phantoms

B.1 Unhealthy 3kPa soft phantom with 20mm tumor

Figure B.1, Figure B.2 and Figure B.3.

B.2 Healthy 30kPa stiff phantom

Figure B.4, Figure B.5 and Figure B.6.

B.3 Unhealthy 30kPa stiff phantom with 22mm tumor

Figure B.7, Figure B.8 and Figure B.9.

B.4 Unhealthy 30kPa stiff phantom with 10mm tumor

Figure B.10, Figure B.11 and Figure B.12.

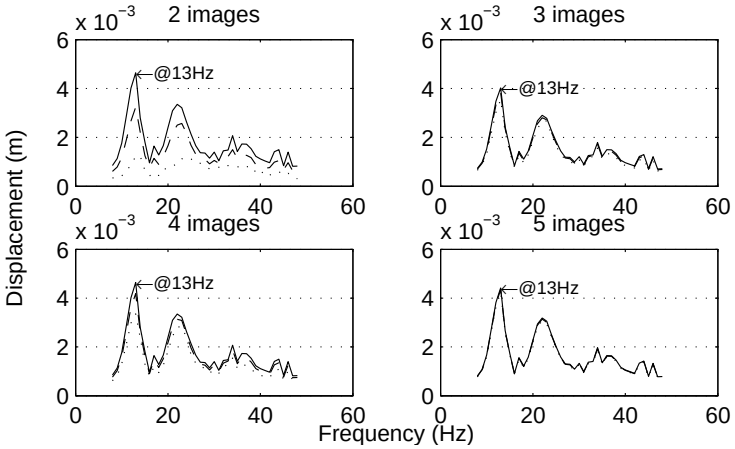

(a) 1D analysis with $Max(\Delta x)$.

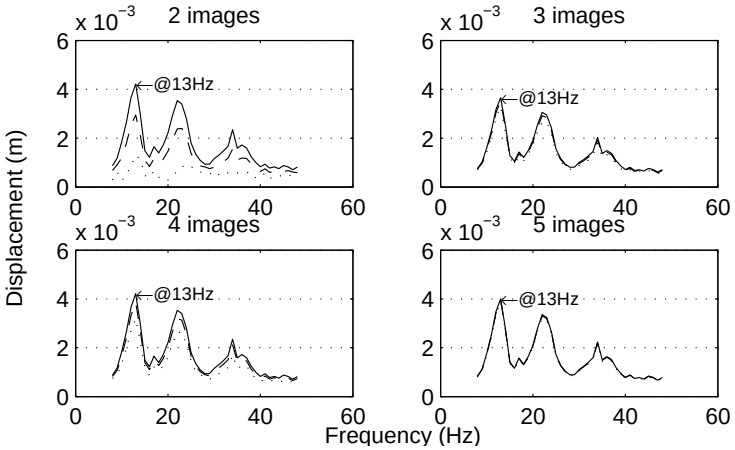

(b) 1D analysis with $Max(\Delta y)$.

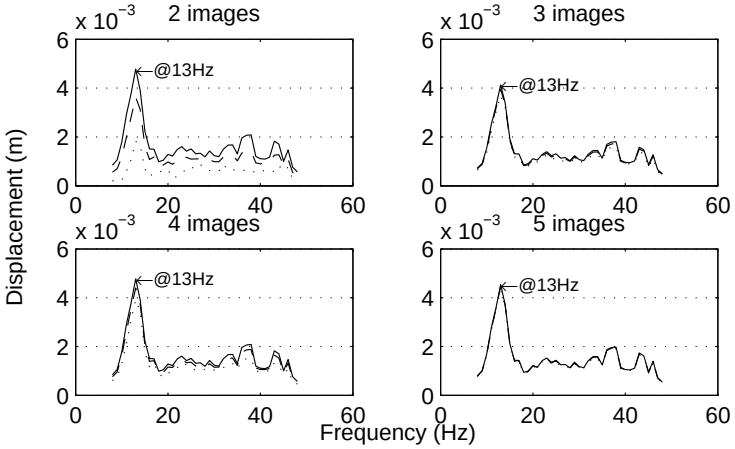

(c) 1D analysis with $Max(\Delta z)$.

FIGURE B.1: 1D analysis for 2,3,4,5 captures on an unhealthy 3kPa soft phantom with 20mm tumor, where Δx, Δy and Δz are displacements along X, Y and Z axes, respectively. 90th percentile (solid) represents the best case and 10th percentile (dotted) indicates the worst.

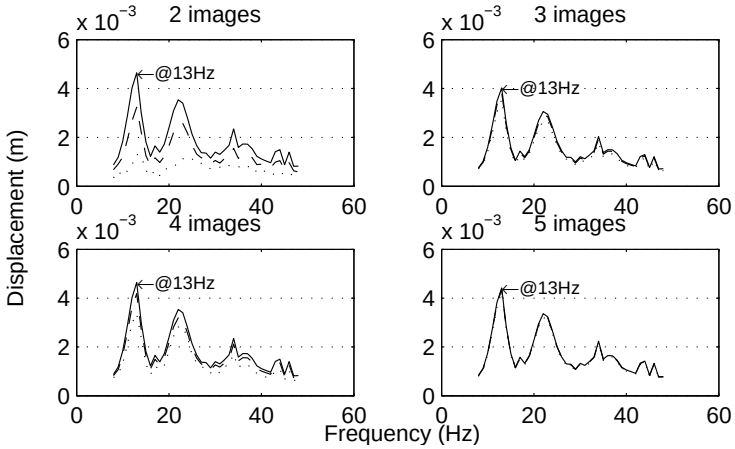

(a) 2D displacement analysis with $Max(\Delta x, \Delta y)$.

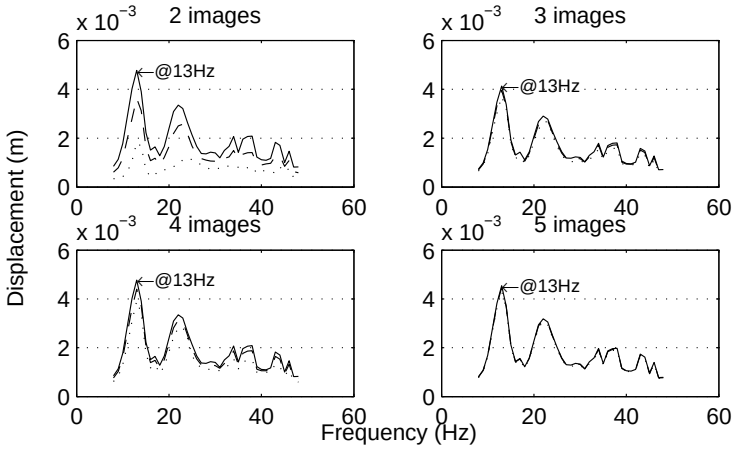

(b) 2D displacement analysis with $Max(\Delta x, \Delta z)$.

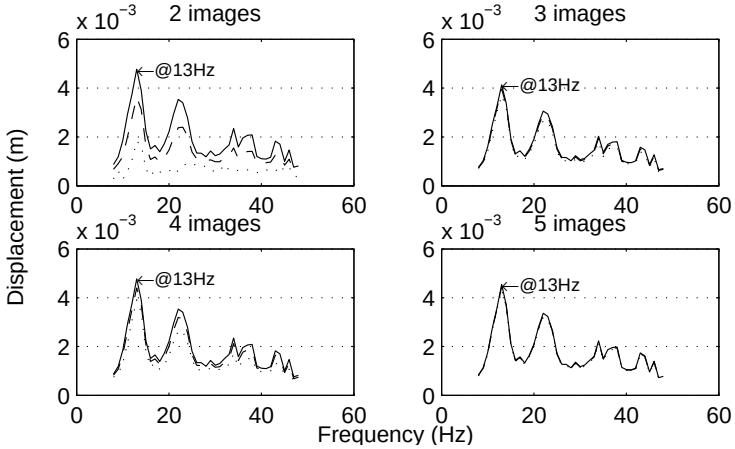

(c) 2D displacement analysis with $Max(\Delta y, \Delta z)$.

FIGURE B.2: 2D analysis for 2,3,4,5 captures on an unhealthy 3kPa soft phantom with 20mm tumor, where Δx, Δy and Δz are displacements along X, Y and Z axes, respectively. 90th percentile (solid) represents the best case and 10th percentile (dotted) indicates the worst.

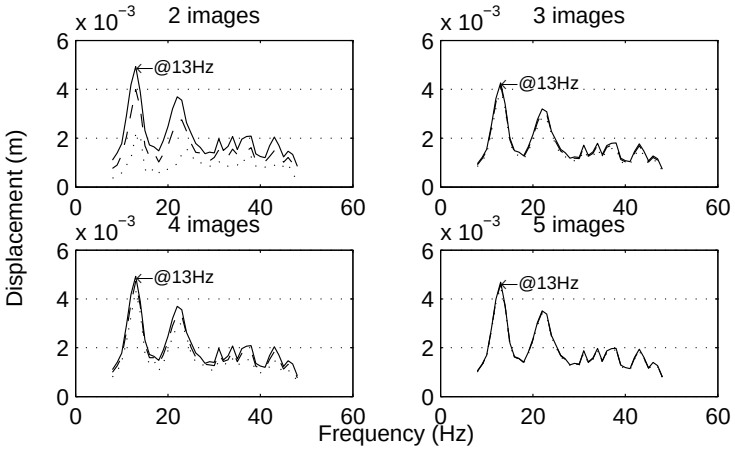

(a) 3D displacement analysis with $Max(\Delta x, \Delta y, \Delta z)$.

FIGURE B.3: 3D analysis for 2,3,4,5 captures on an unhealthy 3kPa soft phantom with 20mm tumor, where Δx, Δy and Δz are displacements along X, Y and Z axes, respectively. 90th percentile (solid) represents the best case and 10th percentile (dotted) indicates the worst.

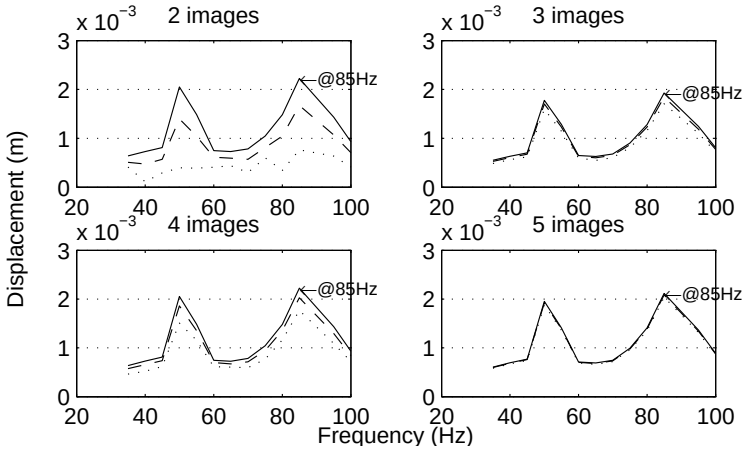

(a) 1D analysis with $Max(\Delta x)$.

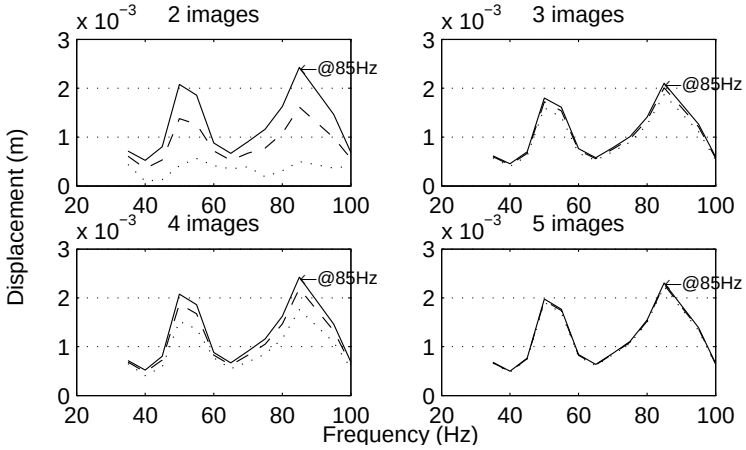

(b) 1D analysis with $Max(\Delta y)$.

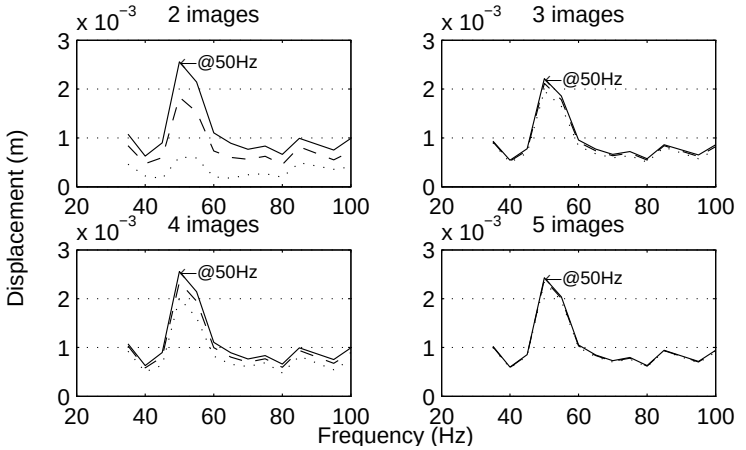

(c) 1D analysis with $Max(\Delta z)$.

FIGURE B.4: 1D analysis for 2,3,4,5 captures on a healthy 30kPa stiff phantom, where Δx, Δy and Δz are displacements along X, Y and Z axes, respectively. 90th percentile (solid) represents the best case and 10th percentile (dotted) indicates the worst.

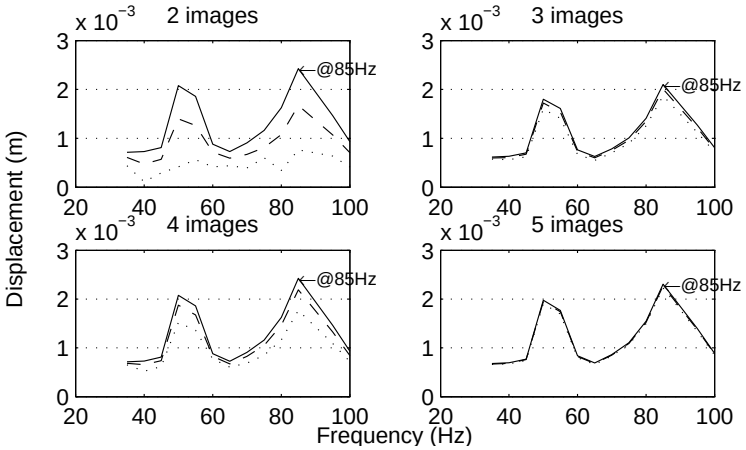

(a) 2D displacement analysis with $Max(\Delta x, \Delta y)$.

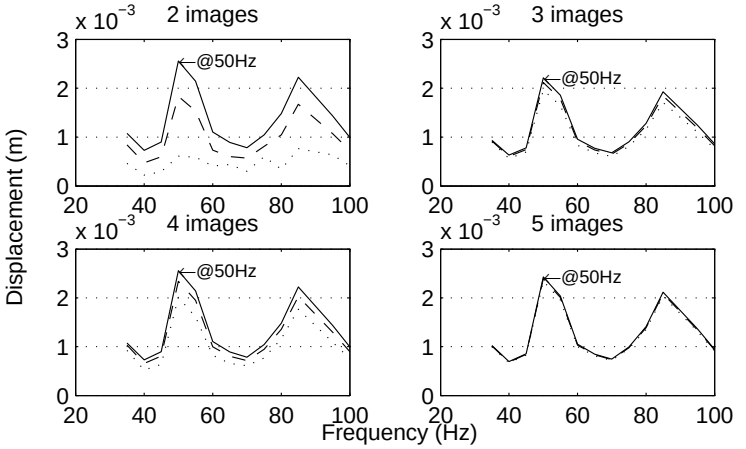

(b) 2D displacement analysis with $Max(\Delta x, \Delta z)$.

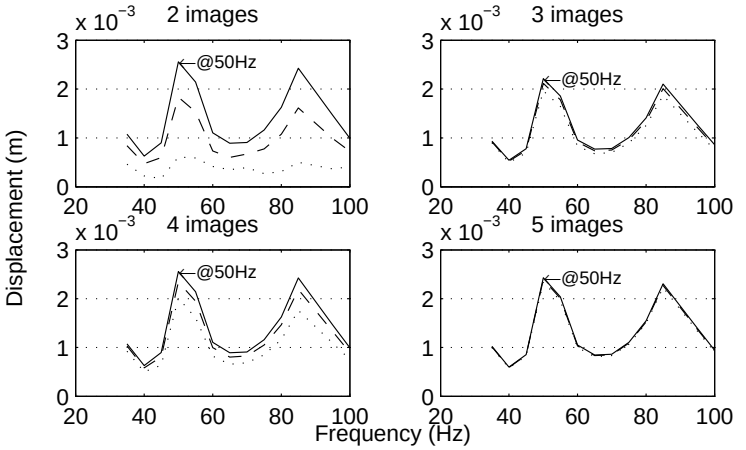

(c) 2D displacement analysis with $Max(\Delta y, \Delta z)$.

FIGURE B.5: 2D analysis for 2,3,4,5 captures on a healthy 30kPa stiff phantom, where Δx, Δy and Δz are displacements along X, Y and Z axes, respectively. 90th percentile (solid) represents the best case and 10th percentile (dotted) indicates the worst.

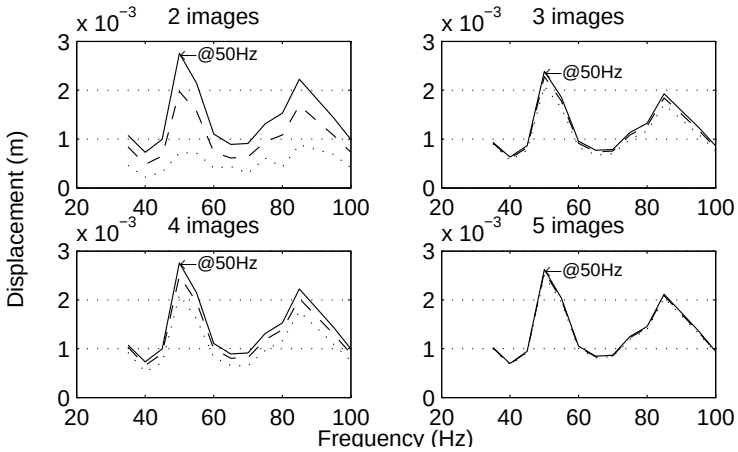

(a) 3D displacement analysis with $Max(\Delta x, \Delta y, \Delta z)$.

FIGURE B.6: 3D analysis for 2,3,4,5 captures on a healthy 30kPa stiff phantom, where Δx, Δy and Δz are displacements along X, Y and Z axes, respectively. 90th percentile (solid) represents the best case and 10th percentile (dotted) indicates the worst.

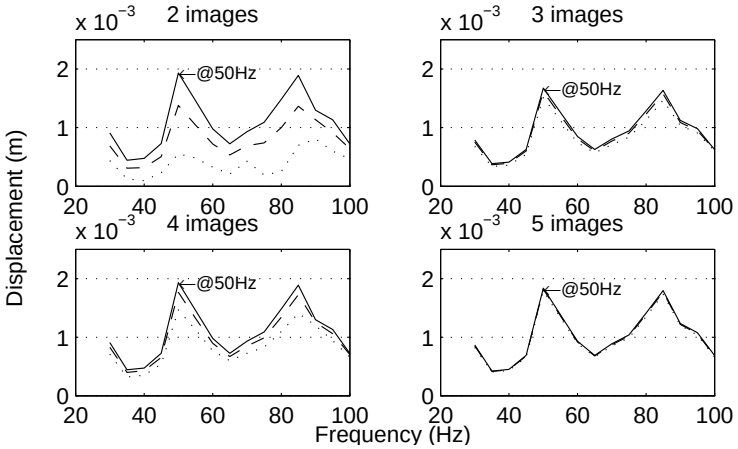

(a) 1D analysis with $Max(\Delta x)$.

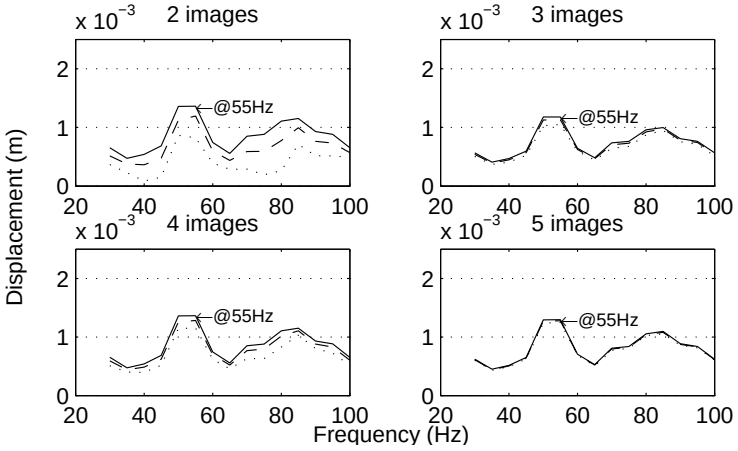

(b) 1D analysis with $Max(\Delta y)$.

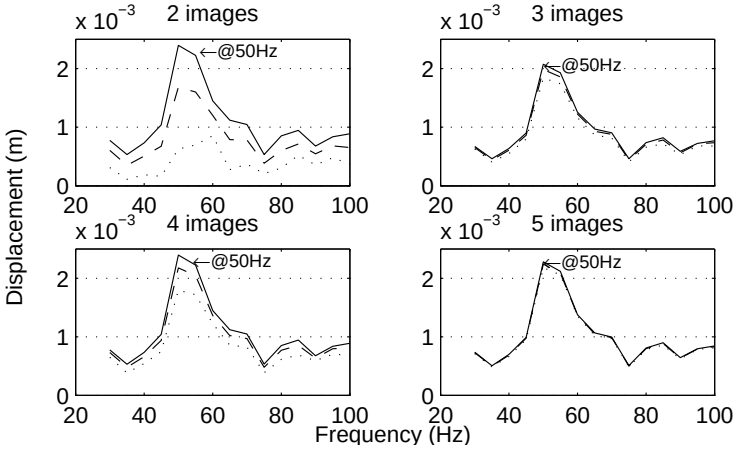

(c) 1D analysis with $Max(\Delta z)$.

FIGURE B.7: 1D analysis for 2,3,4,5 captures on an unhealthy 30kPa stiff phantom with 22mm tumor, where Δx, Δy and Δz are displacements along X, Y and Z axes, respectively. 90th percentile (solid) represents the best case and 10th percentile (dotted) indicates the worst.

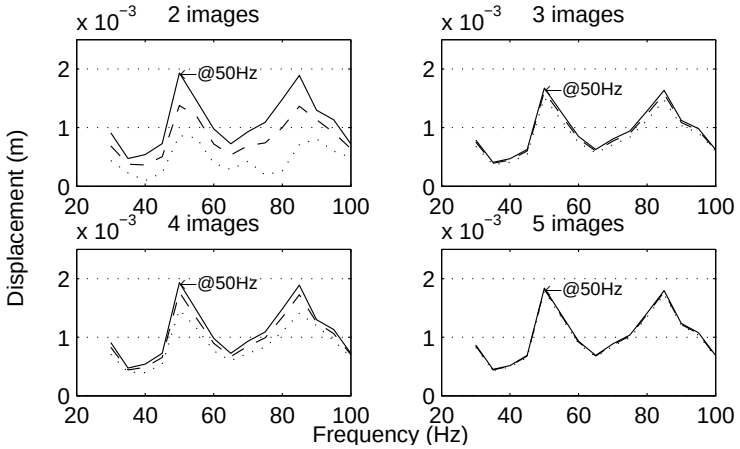

(a) 2D displacement analysis with $Max(\Delta x, \Delta y)$.

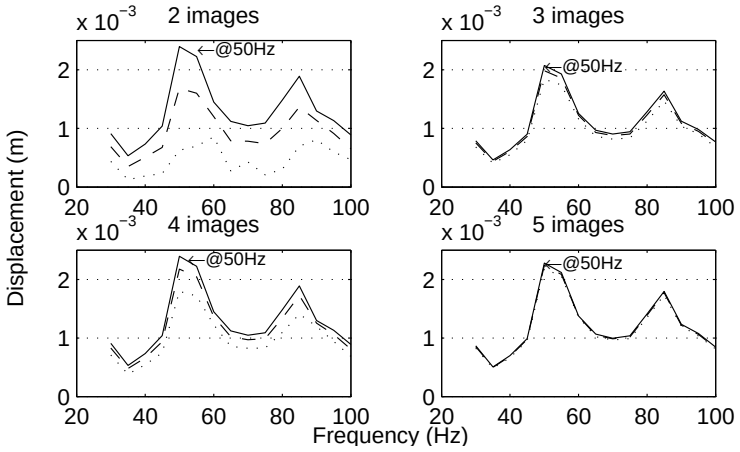

(b) 2D displacement analysis with $Max(\Delta x, \Delta z)$.

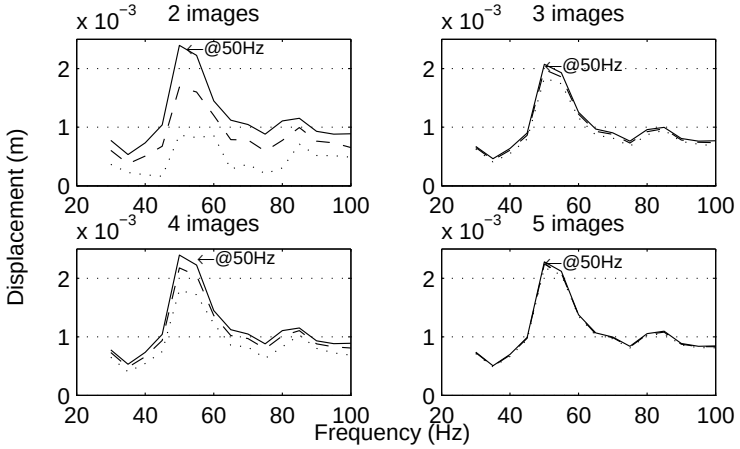

(c) 2D displacement analysis with $Max(\Delta y, \Delta z)$.

FIGURE B.8: 2D analysis for 2,3,4,5 captures on an unhealthy 30kPa stiff phantom with 22mm tumor, where Δx, Δy and Δz are displacements along X, Y and Z axes, respectively. 90th percentile (solid) represents the best case and 10th percentile (dotted) indicates the worst.

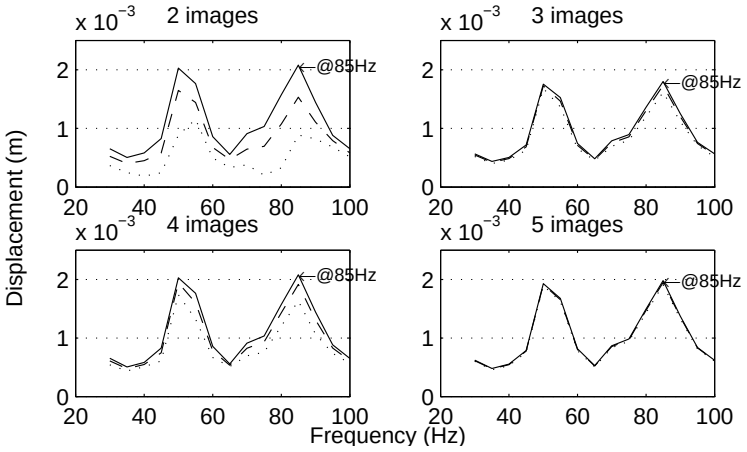

(a) 3D displacement analysis with $Max(\Delta x, \Delta y, \Delta z)$.

FIGURE B.9: 3D analysis for 2,3,4,5 captures on an unhealthy 30kPa stiff phantom with 22mm tumor, where Δx, Δy and Δz are displacements along X, Y and Z axes, respectively. 90th percentile (solid) represents the best case and 10th percentile (dotted) indicates the worst.

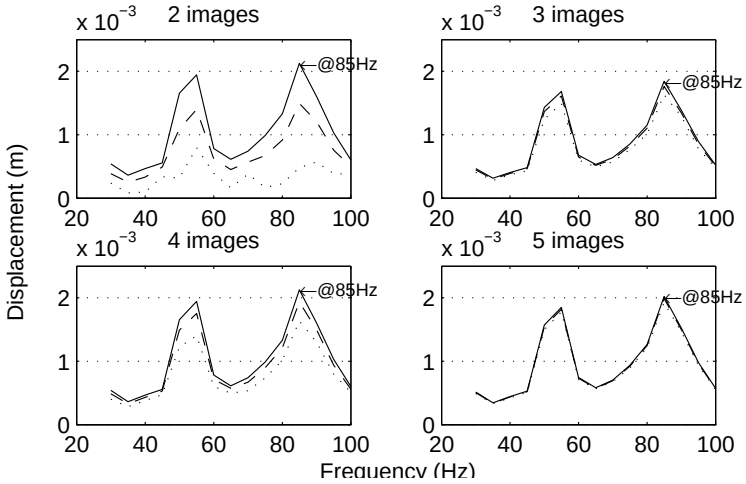

(a) 1D analysis with $Max(\Delta x)$.

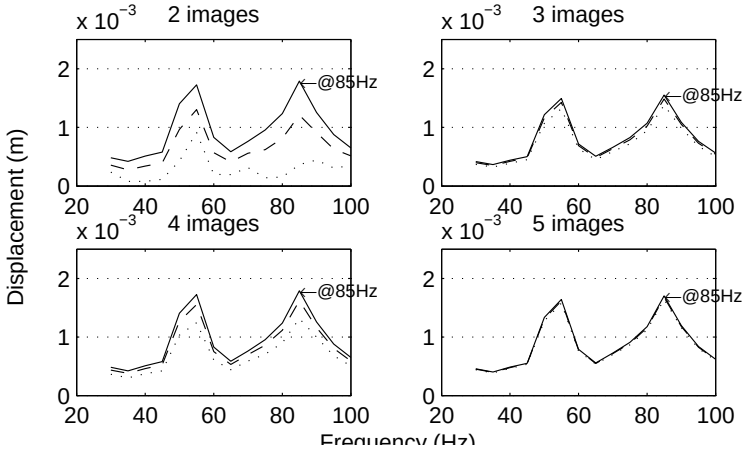

(b) 1D analysis with $Max(\Delta y)$.

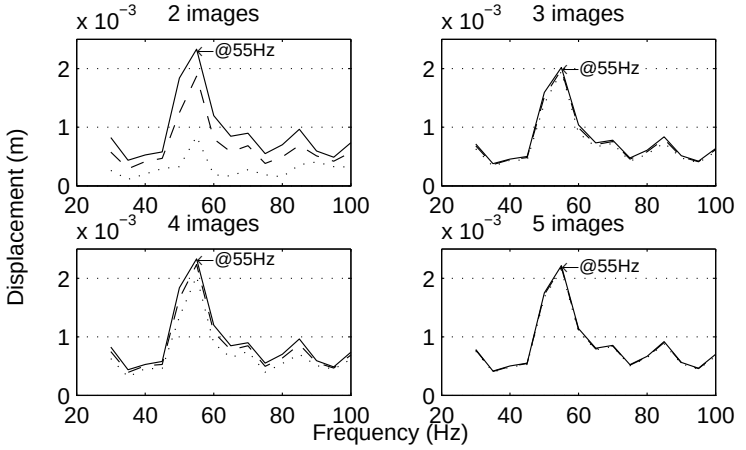

(c) 1D analysis with $Max(\Delta z)$.

FIGURE B.10: 1D analysis for 2,3,4,5 captures on an unhealthy 30kPa stiff phantom with 10mm tumor, where Δx, Δy and Δz are displacements along X, Y and Z axes, respectively. 90th percentile (solid) represents the best case and 10th percentile (dotted) indicates the worst.

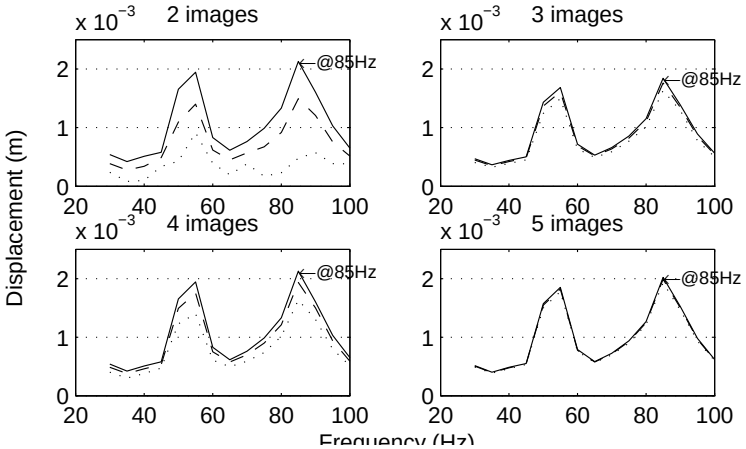

(a) 2D displacement analysis with $Max(\Delta x, \Delta y)$.

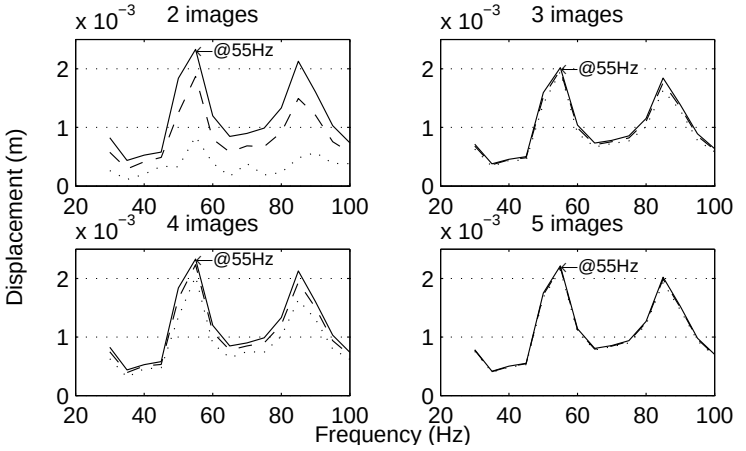

(b) 2D displacement analysis with $Max(\Delta x, \Delta z)$.

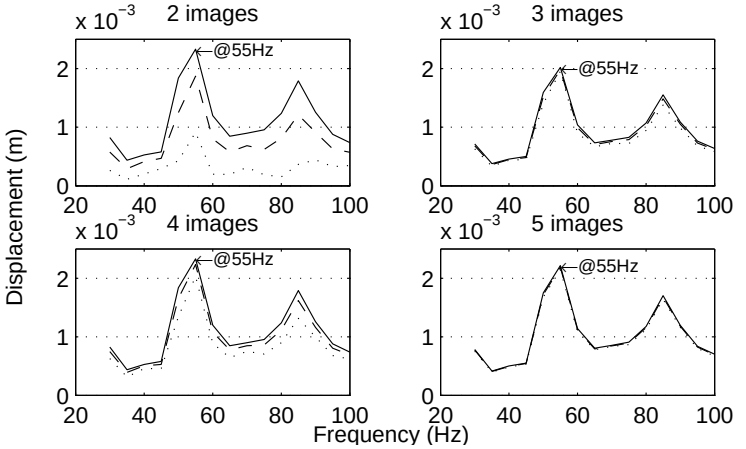

(c) 2D displacement analysis with $Max(\Delta y, \Delta z)$.

FIGURE B.11: 2D analysis for 2,3,4,5 captures on an unhealthy 30kPa stiff phantom with 10mm tumor, where Δx, Δy and Δz are displacements along X, Y and Z axes, respectively. 90th percentile (solid) represents the best case and 10th percentile (dotted) indicates the worst.

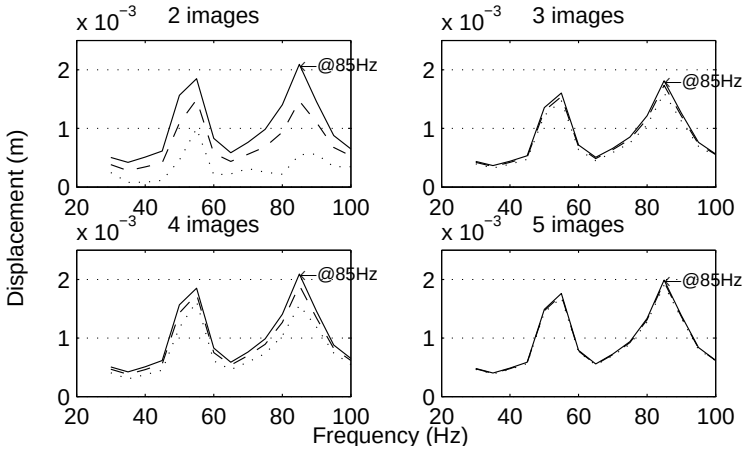

(a) 3D displacement analysis with $Max(\Delta x, \Delta y, \Delta z)$.

FIGURE B.12: 3D analysis for 2,3,4,5 captures on an unhealthy 30kPa stiff phantom with 10mm tumor, where Δx, Δy and Δz are displacements along X, Y and Z axes, respectively. 90th percentile (solid) represents the best case and 10th percentile (dotted) indicates the worst.

Appendix C

Program User Guide

This program user guide covers the key software introduced in this thesis.

C.1 Modal Testing System

Make sure all hardware are operational, LabVIEW is running and camera at the selected imaging location is turned on. Note there are five different cameras available in the current DIET system, so make sure the other four unused cameras are switched off. Otherwise, dSweep will initialize on the first camera connected. Additional imaging locations can be created simply by repositioning the camera from the DIET setup to a desired location. When imaging at positions other than the default positions, zoom value must be determined by visual inspection using RelCtrl.

Two pieces of software are involved and required to be started. In general, the order of startup does not matter, but it is good to start the main application (dSweep) first as it will take a few seconds to setup the actuator and imaging device. Their usages are described in the following sections.

C.1.1 dSweep

dSweep takes a number of parameters. To get a list of supported parameters, invoke the program with "-h". For example,

```
C:\Work\software\dTrackingSoftware\bin\Release>dSweep.exe -h
dTracking.dSweep Build Sep 27 2010 @ 20:24:55
```

```
Usage dSweep <options> [default values]

-i ip           RIO <i>p [10.0.0.2]
-p port         RIO <p>ort [2345]
-n x            <n>umber of photos [3]
-d dir          <d>irectory to store photos [C:\DIET]
-a amp          Actuator <a>mplitude [0.500000]
-u f/x          Camera apert<u>re [56]
                       32 = AV_2f8
                       35 = AV_3f2
                       37 = AV_3f5_3rd
                       40 = AV_4f
                       43 = AV_4f5_3rd
                       45 = AV_5f6_3rd
                       48 = AV_5f6
                       51 = AV_6f3
                       53 = AV_7f1
                       56 = AV_8f
-t spd          Camera shu<t>ter speed [56]
                       For a complete list of values, see SDK/datasheet.
                       37 = TV_5s
                       40 = TV_4s
                       44 = TV_3s
                       48 = TV_2s
                       56 = TV_1s
-o ISO          Camera IS<o> value[69]
                       69 = ISO_80
                       72 = ISO_100
                       80 = ISO_200
                       88 = ISO_400
                       96 = ISO_800
                       104 = ISO_1600
-z zoom         Camera <z>oom[5]
                        0 <= zoom <= 19
-q qual         Image <q>uality[5]
                       1 = IQ_ECONOMY
                       2 = IQ_NORMAL
                       3 = IQ_FINE
                       4 = IQ_LOSSLESS
```

```
                        5 = IQ_SUPERFINE
-s size          Image <s>ize[7]
                        0 = IS_LARGE   4000x3000
                        1 = IS_MEDIUM1 3264x2448
                        2 = IS_SMALL   640x480
                        3 = IS_MEDIUM2 2592x1944
                        7 = IS_MEDIUM3 1600x1200

BUILD Sep 27 2010 20:24:55
```

Default values are shown in square brackets ([]) and all available settings are shown.

The following command starts a session with zoom value of 8 and three image capture per oscillation cycle (refer to Table 4.1 for default settings).

```
dSweep -z 8 -n 3
```

This example starts a custom session with $f4$, $2second$ exposure, ISO 200 and actuation amplitude of $1mm$.

```
dSweep -z 8 -n 3 -u 40 -t 48 -o 80
```

dSweep communicates with LabVIEW actuation control program using port 2345 and the its internal job queue can be accessed on port 5678 using packets shown in Appendix D.

C.1.2 Image Tracking Software

Tracking software will communicate with the dSweep job queue on port 6789. Tracking will retrieve jobs from the queue and default setting assumes dSweep is running on the same computer. Start the program in by typing the following in MATLAB.

```
>>dclient
```

If dSweep is running on a different computer on the network, use the following.

```
>>dclient(ip,6789) % ip that dSweep is running on
```

The program will add all subdirectories found in program folder to MATLAB's path. This is done by the following piece of code. If, for some reason, the program does no start from the program's directory, problems are likely to occur. It is important to make sure MATLAB includes those paths.

```
currentExpDIR = pwd; % current directory
addpath(currentExpDIR)
addpath([currentExpDIR '/matlab_bgl'])
addpath([currentExpDIR '/cubedata'])
addpath([currentExpDIR '/substitution_toolbox'])
```

C.2 DIET Imaging (gCapture)

The imaging system previously used G5 cameras for imaging, and are all upgraded to G9 cameras. Since G9 uses a newer SDK (PRSDK), imaging software has to be reimplemented. This is done with a server/client setup.

C.2.1 Server

The imaging server supports a list of options that can be changed during startup, default values are shown in square brackets.

```
C:\Work\software\gCapture\bin\Release>gCapture.exe -h

##################################################

gCapture(PRSDK) Build Oct  7 2010 @ 11:42:19


##################################################
Usage dSweep <options> [default values]

-f filepath     <f>ile containing list of frequencies to capture
[./sweep.cfg]
-i ip           RIO <i>p [10.0.0.2]
-p port         RIO <p>ort [2345]
-n x            <n>umber of photos [10]
```

```
-d dir          <d>irectory to store photos [C:\DIET]
-a amp          Actuator <a>mplitude [0.500000]
-u f/x          Camera apert<u>re [56]
                       32 = AV_2f8
                       35 = AV_3f2
                       37 = AV_3f5_3rd
                       40 = AV_4f
                       43 = AV_4f5_3rd
                       45 = AV_5f6_3rd
                       48 = AV_5f6
                       51 = AV_6f3
                       53 = AV_7f1
                       56 = AV_8f
-t spd          Camera shu<t>ter speed [56]
                       For a complete list of values, see SDK/datasheet.
                       37 = TV_5s
                       40 = TV_4s
                       44 = TV_3s
                       48 = TV_2s
                       56 = TV_1s
-o ISO          Camera IS<o> value[69]
                       69 = ISO_80
                       72 = ISO_100
                       80 = ISO_200
                       88 = ISO_400
                       96 = ISO_800
                       104 = ISO_1600
-z zoom         Camera <z>oom[5]
                        0 <= zoom <= 19
-q qual         Image <q>uality[5]
                       1 = IQ_ECONOMY
                       2 = IQ_NORMAL
                       3 = IQ_FINE
                       4 = IQ_LOSSLESS
                       5 = IQ_SUPERFINE
-s size         Image <s>ize[7]
                       0 = IS_LARGE   4000x3000
                       1 = IS_MEDIUM1 3264x2448
                       2 = IS_SMALL   640x480
```

```
                        3 = IS_MEDIUM2 2592x1944
                        7 = IS_MEDIUM3 1600x1200
-v              verbose

BUILD Oct  7 2010 11:42:19
```

Depending on the number of cameras chosen by user, gCapture will try to initialize on all those devices. For example, following command starts a imaging sever with five cameras, ten images per oscillation capture, and at a zoom value of 5.

```
gCapture -c 5 -n 10 -z 5
```

However, since above command uses all default values for those options, user may omit these options. The following command will be equivalent.

```
gCapture
```

Different settings of ISO, Aperture and Shutter Value can be specified during the startup. These values will not be allowed to be changed once the server is started. To use different capture settings, the program must be terminated by the client before being restarted.

Calibration is compulsory as each startup will result in a different focus. Once calibration is finished and server is started, the client can be run.

C.2.2 Client

A remote control application is developed, so multiple patients can be imaged without recalibrating the cameras with every different patient. Simply have the server running and run client to enqueue different imaging jobs.

```
C:\Work\software\gCaptureRC\bin\Release>gCaptureRC.exe -h
Usage dietclient.exe <opt>

-k:      to kill the server
-i <dSpace ip> :        Specify the dSpace Ip adress [127.0.0.1]
-p <dSpace port> :      Specify the dSpace port [3456]
-f <cfgfile> :  Specify the actuator frequency [50]
```

```
BUILD Oct  5 2010 13:10:00
```

The following command enqueues a new configuration file "file.cfg" into the job pool. User may queue up new jobs at anytime, even during imaging. Server will immediately recognize and acknowledge the job request and will read out the frequencies from the supplied configuration file once it finishes imaging the current frequency. It's a good idea to store the configuration files in the same directory or lower than the program.

```
gCaptureRC -f file.cfg
```

To terminate the server at anytime, use the following command. Server will acknowledge the kill signal and terminate itself once it has finished imaging the current frequency. This is possible because server is running on a dedicated thread.

```
gCaptureRC -k
```

C.3 RelCtrl

Note that this program is only intended to be a tool for determining appropriate zoom values.

RelCtrl is a piece of software that comes with almost all PRSDK distributions. It is a demo application that can be used for live viewing. Additional functionalities are brought in so live visual feedbacks on zoom adjustments can be seen. The main window is shown in Figure C.1. Execute the following procedure to obtain an appropriate zoom value.

First have the strobe system on full brightness.

Second connect to camera and start view finder.

Third adjust the zoom setting to obtain a good visual of the targeted object and remember the zoom value.

Finally refocus the lens. Having full brightness helps the lens with focusing.

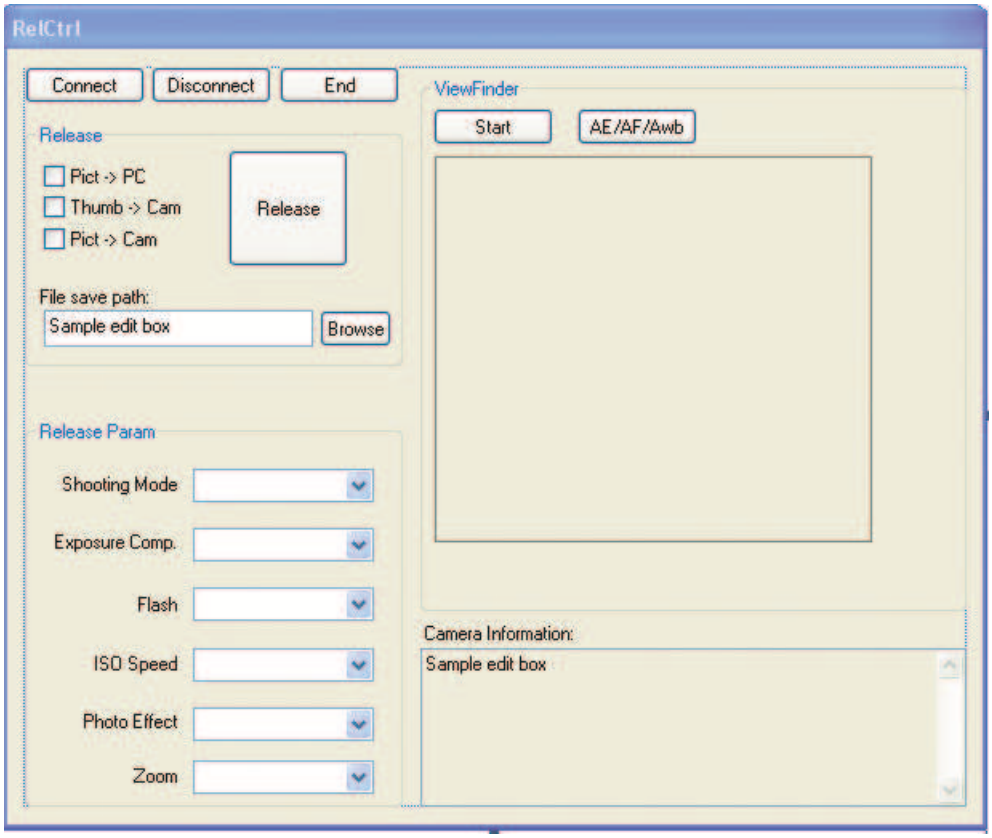

FIGURE C.1: RelCtrl program provides visual feedback that aids zoom selection.

Appendix D

Communication Protocol

D.1 Imaging and Tracking

The protocol shown in Table D.1 is employed to keep imaging and tracking synchronized. The dSweep server keeps things in the correct order. Since all communications are bi-directional, additional features can be included quite easily.

Table D.1: Communication protocol.

Content	Origin	Destination	Functionality
DSWEEP&=C:/DIET/Sweep - DATE/Motion.16Hz/	Imaging	Server	Imaging at 16Hz is finished Payload contains path to the folder
DTRACK&=	Tracking	Server	Requesting for a new job to track
DTRACK&=JOBRXD	Tracking	Server	Acknowledging packets from the tracking program to server, new job received
ACKDSWEEP&=	Server	Imaging	Acknowledging packets from Imaging routine
ACKDTRACK&=C:/DIET/Sweep - DATE/Motion.16Hz/	Server	Tracking	Acknowledging packets from server for the image tracking program. Payload is the path that leads to those images
ACKDTRACK&=JOBFIN	Server	Tracking	Acknowledging packets from server to image tracking program. Imaging is finished
ACKDTRACK&=QEMPTY	Server	Tracking	Acknowledging packets from server to image tracking program. Queue is empty

Bibliography

[1] World Health Organisation. The global burden of disease: 2004 update, 2008.

[2] Michel P. Coleman et al. Cancer survival in five continents: a worldwide population-based study (concord). *The lancet oncology*, 9(8):730–756, August 2008. ISSN 1474-5488. doi: 10.1016/S1470-2045(08)70179-7.

[3] New Zealand Ministry of Health. Cancer: New registrations and deaths 2007, July 2010.

[4] New Zealand Ministry of Health. Cancer patient survival covering the period 1994 to 2003, 2006.

[5] J. P. Pierce, L. Natarajan, J. Marshall, and K. Messer. Re: Dietary fat reduction and breast cancer outcome: interim efficacy results from the Women's Intervention Nutrition Study. *J. Natl. Cancer Inst.*, 99:900–901, Jun 2007.

[6] L. H. Breimer and H. Theobald. RE: Moderate alcohol intake and cancer incidence in women. *J. Natl. Cancer Inst.*, 101:1093, Aug 2009.

[7] P. Boffetta, M. Hashibe, C. La Vecchia, W. Zatonski, and J. Rehm. The burden of cancer attributable to alcohol drinking. *Int. J. Cancer*, 119:884–887, Aug 2006.

[8] L. S. Mørch et al. Alcohol drinking, consumption patterns and breast cancer among Danish nurses: a cohort study. *Eur J Public Health*, 17:624–629, Dec 2007.

[9] N. Hamajima et al. Alcohol, tobacco and breast cancer–collaborative reanalysis of individual data from 53 epidemiological studies, including 58,515 women with breast cancer and 95,067 women without the disease. *Br. J. Cancer*, 87:1234–1245, Nov 2002.

[10] P. A. van den Brandt et al. Pooled analysis of prospective cohort studies on height, weight, and breast cancer risk. *Am. J. Epidemiol.*, 152:514–527, Sep 2000.

[11] S R Wolman et al. Genetic markers as prognostic indicators in breast cancer. *Cancer*, 70:1765–1774, 1992.

[12] J. G. Brody. Everyday exposures and breast cancer. *Rev Environ Health*, 25:1–7, 2010.

[13] Cathrin Brisken. Endocrine Disruptors and Breast Cancer. ., 2008.

[14] M. Kriege et al. Efficacy of MRI and mammography for breast-cancer screening in women with a familial or genetic predisposition. *N. Engl. J. Med.*, 351:427–437, Jul 2004.

[15] P. C. Gøtzsche, O. J. Hartling, M. Nielsen, J. Brodersen, and K. J. Jørgensen. Breast screening: the facts–or maybe not. *BMJ*, 338:b86, 2009.

[16] A. Asghari and M. K. Nicholas. Pain during mammography: the role of coping strategies. *Pain*, 108:170–179, Mar 2004.

[17] J. Law and K. Faulkner. Cancers detected and induced, and associated risk and benefit, in a breast screening programme. *Br J Radiol*, 74:1121–1127, Dec 2001.

[18] K. Faulkner. Mammography screening and genetic disposition to radiation risk. *Br J Radiol*, 80:591–592, Aug 2007.

[19] J. Law. Risk and benefit associated with radiation dose in breast screening programmes–an update. *Br J Radiol*, 68:870–876, Aug 1995.

[20] J. Law. Variations in individual radiation dose in a breast screening programme and consequences for the balance between associated risk and benefit. *Br J Radiol*, 66:691–698, Aug 1993.

[21] J. Ophir, I. Cespedes, H. Ponnekanti, Y. Yazdi, and X. Li. Elastography: a quantitative method for imaging the elasticity of biological tissues. *Ultrason Imaging*, 13: 111–134, Apr 1991.

[22] B. S. Garra et al. Elastography of breast lesions: initial clinical results. *Radiology*, 202:79–86, Jan 1997.

[23] K.D. Paulsen, E.E.W. Van Houten, M.M. Doyley, and J.B. Weaver. Magnetic resonance elastography in the breast: initial reconstructions of damping coefficient. In *Biomedical Imaging, 2002. Proceedings. 2002 IEEE International Symposium on*, pages 157 – 160, 2002. doi: 10.1109/ISBI.2002.1029217.

[24] A. Samani, C. Luginbuhl, and D.B. Plewes. Magnetic resonance elastography technique for breast tissue in-vitro elasticity measurement. In *Biomedical Imaging, 2002. Proceedings. 2002 IEEE International Symposium on*, pages 931 – 934, 2002. doi: 10.1109/ISBI.2002.1029414.

[25] M. Muller et al. 8c-5 full 3d inversion of the viscoelasticity wave propagation problem for 3d ultrasound elastography in breast cancer diagnosis. In *Ultrasonics Symposium, 2007. IEEE*, pages 672 –675, 28-31 2007. doi: 10.1109/ULTSYM.2007.174.

[26] Y. Yamakoshi, J. Sato, and T. Sato. Ultrasonic imaging of internal vibration of soft tissue under forced vibration. *Ultrasonics, Ferroelectrics and Frequency Control, IEEE Transactions on*, 37(2):45 –53, mar 1990. ISSN 0885-3010. doi: 10.1109/58.46969.

[27] T. Matsumura et al. Measurement of elastic property of breast tissue for elasticity imaging. In *Ultrasonics Symposium (IUS), 2009 IEEE International*, pages 1451 –1454, 20-23 2009. doi: 10.1109/ULTSYM.2009.5442044.

[28] R. Sinkus et al. Nonlinear viscoelastic properties of tissue assessed by ultrasound. *Ultrasonics, Ferroelectrics and Frequency Control, IEEE Transactions on*, 53(11):2009 –2018, november 2006. ISSN 0885-3010. doi: 10.1109/TUFFC.2006.141.

[29] C.E. Hann et al. Strobe imaging system for digital image-based elasto-tomography breast cancer screening. *Industrial Electronics, IEEE Transactions on*, 56(8):3195 –3202, aug. 2009. ISSN 0278-0046. doi: 10.1109/TIE.2009.2023643.

[30] A. Peters, J. G. Chase, and E. E. Van Houten. Estimating elasticity in heterogeneous phantoms using Digital Image Elasto-Tomography. *Med Biol Eng Comput*, 47:67–76, Jan 2009.

[31] R. Brown. *Three-dimensional motion capture for the DIET breast cancer imaging system.* PhD thesis, Department of Mechanical Engineering, University of Canterbury, Christchurch, New Zealand, 2008.

[32] A. Peters. *Digital Image Elasto-Tomography Mechanical Propeties reconstruction from Surface Measured Displacement Data.* PhD thesis, Department of Mechanical Engineering, University of Canterbury, Christchurch, New Zealand, 2007.

[33] Lotz T., Simpson P. D., Stocker D., Hann C.E., and Chase J.G. In vitro evaluation of surface based non-invasive breast cancer screening with digital image based elasto tomography (diet). In *Proc IEEE Eng Med and Biol Soc 2010*, 2010.

[34] T Lotz, N. Muller, C.E. Hann, and J.G. Chase. Minimal elastographic modeling of breast cancer for model based tumour detection in a digital image elasto tomography (diet) system. In *Proc SPIE Medical Imaging 2011*, Orlando, Florida, USA, 2011.

[35] C. W. De Silva. *Vibration: Fundamentals and Practice, Second Edition.* CRC/-Taylor & Franci, 2007.

[36] M. Sridhar and M. F. Insana. Ultrasonic measurements of breast viscoelasticity. *Med Phys*, 34:4757–4767, Dec 2007.

[37] M. Sridhar, J. Liu, and M. F. Insana. Viscoelasticity imaging using ultrasound: parameters and error analysis. *Phys Med Biol*, 52:2425–2443, May 2007.

[38] D. J. Ewins. *Modal Testing: Theory, Practice and Application (Mechanical Engineering Research Studies Engineering Design Series)*. Taylor & Francis Group, February 2003. ISBN 0863802184.

[39] D.B. Rendon, J.L.R. Ojeda, L.F.C. Foix, D.S. Morillo, and M.A. Fernandez. Mapping the human body for vibrations using an accelerometer. In *Engineering in Medicine and Biology Society, 2007. EMBS 2007. 29th Annual International Conference of the IEEE*, pages 1671 –1674, 22-26 2007. doi: 10.1109/IEMBS.2007.4352629.

[40] T. Cano, F. Chapelle, J.-M. Lavest, and P. Ray. High frequency displacement measurement based on video and accelerometer for mechanical purpose. In *Intelligent Signal Processing, 2007. WISP 2007. IEEE International Symposium on*, pages 1 –6, 3-5 2007. doi: 10.1109/WISP.2007.4447613.

[41] Shukui Zhao, Yi Zheng, Shigao Chen, and J.F. Greenleaf. High sensitivity vibration estimation using pulse echo doppler ultrasound. In *Ultrasonics, 2003 IEEE Symposium on*, volume 2, pages 1923 – 1926 Vol.2, 5-8 2003. doi: 10.1109/ULTSYM.2003.1293292.

[42] O. Bou Matar, J.P. Remenieras, L. Pizarro, A. Roncin, and F. Patat. Performances of the parametric acoustic vibrometer for vibration sensing. In *Ultrasonics Symposium, 1997. Proceedings., 1997 IEEE*, volume 1, pages 605 –608 vol.1, 5-8 1997. doi: 10.1109/ULTSYM.1997.663094.

[43] URL http://www.migatron.com/products/rps-412a-v-1/index.htm.

[44] H. A. Jenkins, N. Pergola, and J. Kasic. Anatomical vibrations that implantable microphones must overcome. *Otol. Neurotol.*, 28:579–588, Aug 2007.

[45] Chen-Chia Wang et al. Human life signs detection using high-sensitivity pulsed laser vibrometer. *Sensors Journal, IEEE*, 7(9):1370 –1376, sept. 2007. ISSN 1530-437X. doi: 10.1109/JSEN.2007.905041.

[46] A.O. Kucherik, M.V. Donetc, V.G. Prokoshev, and S.M. Arakelian. Laser doppler diagnostics of the human capillary blood stream system near skin surface. In *Lasers and Electro-Optics Europe, 2005. CLEO/Europe. 2005 Conference on*, pages 647 – 647, 17-17 2005. doi: 10.1109/CLEOE.2005.1568423.

[47] PW Smutz, RG Dong, and Schopper Aaron. A study of tissue vibration transmissibility using scanning laser vibrometer. In *25th annual meeting of the american society of biomechanics*, pages 8–11, San Diego, 2001.

[48] Lorenzo Scalise, Francesco Rossetti, and Nicola Paone. Hand vibration: non-contact measurement of local transmissibility. *International Archives of Occupational and Environmental Health*, 81:31–40, 2007. ISSN 0340-0131. URL http://dx.doi.org/10.1007/s00420-007-0190-3. 10.1007/s00420-007-0190-3.

[49] V.T. Chitnis, S. Kumar, and D. Sen. Optical fiber sensor for vibration amplitude measurement. *Lightwave Technology, Journal of*, 7(4):687 –691, apr 1989. ISSN 0733-8724. doi: 10.1109/50.19096.

[50] R. Dib, Y. Alayli, and P. Wagstaff. A broadband amplitude-modulated fibre optic vibrometer with nanometric accuracy. *Measurement*, 35(2):211 – 219, 2004. ISSN 0263-2241. doi: DOI:10.1016/S0263-2241(03)00041-1. 2 special issues: Vibration measurement by Laser techniques Advances and Applications and 7th workshop on ADC modelling and testing.

[51] A. Vallan, M.L. Casalicchio, and G. Perrone. Displacement and acceleration measurements in vibration tests using a fiber optic sensor. *Instrumentation and Measurement, IEEE Transactions on*, 59(5):1389 –1396, may 2010. ISSN 0018-9456. doi: 10.1109/TIM.2010.2040934.

[52] G. Perrone and A. Vallan. A low-cost optical sensor for noncontact vibration measurements. *Instrumentation and Measurement, IEEE Transactions on*, 58(5):1650 –1656, may 2009. ISSN 0018-9456. doi: 10.1109/TIM.2008.2009144.

[53] A. Buffa, G. Perrone, and A. Vallan. A plastic optical fiber sensor for vibration measurements. In *Instrumentation and Measurement Technology Conference Proceedings, 2008. IMTC 2008. IEEE*, pages 1387 –1391, 12-15 2008. doi: 10.1109/IMTC.2008.4547259.

[54] S. Feng, T. Lotz, J.G. Chase, and C.E. Hann. An image based vibration sensor for soft tissue modal analysis in a digital image elasto tomography (diet) system. In *Proc IEEE Eng Med and Biol Soc (EMBS2010)*, 2010.

[55] Christopher E. Hann et al. Integral-based parameter identification for long-term dynamic verification of a glucose-insulin system model. *Comput. Methods Prog. Biomed.*, 77(3):259–270, 2005. ISSN 0169-2607. doi: http://dx.doi.org/10.1016/j.cmpb.2004.10.006.

[56] D.G. Lowe. Object recognition from local scale-invariant features. volume 2, pages 1150 –1157 vol.2, 1999. doi: 10.1109/ICCV.1999.790410.

[57] Zhu Daixian. Sift algorithm analysis and optimization. pages 415 –419, apr. 2010. doi: 10.1109/IASP.2010.5476084.

[58] Herbert Bay, Tinne Tuytelaars, and Luc Van Gool. Surf: Speeded up robust features. In *In ECCV*, pages 404–417, 2006.

[59] Zhan-Long Yang and Bao-Long Guo. Image mosaic based on sift. *Intelligent Information Hiding and Multimedia Signal Processing, International Conference on*, 0: 1422–1425, 2008. doi: http://doi.ieeecomputersociety.org/10.1109/IIH-MSP.2008.335.

[60] Johannes Bauer, Niko Sunderhauf, and Peter Protzel. Comparing several implementations of two recently published feature detectors. 2007.

[61] Luo Juan and Oubong Gwun. A comparison of sift, pca-sift and surf. 3(4):143–152, 2009.

[62] *Real-time eye blink detection with GPU-based SIFT tracking*, 2007. doi: 10.1109/CRV.2007.54. URL http://dx.doi.org/10.1109/CRV.2007.54.

[63] T. Terriberry, L. French, and J. Helmsen. Gpu accelerating speeded-up robust features. 2008.

[64] A.J.H. Hii, C.E. Hann, J.G. Chase, and E.E.W. Van Houten. Fast normalized cross correlation for motion tracking using basis functions. *Computer Methods and Programs in Biomedicine*, 82(2):144 – 156, 2006. ISSN 0169-2607. doi: DOI: 10.1016/j.cmpb.2006.02.007.

[65] S. S. Beauchemin and J. L. Barron. The computation of optical flow. *ACM Comput. Surv.*, 27(3):433–466, 1995. ISSN 0360-0300. doi: http://doi.acm.org/10.1145/212094.212141.